EFFECT OF HYBRIDIZATION ON THE EXCHANGE COUPLING IN MAGNETIC MULTILAYERS

by

John Maurice Mander B.Sc

A thesis submitted for the Degree of Doctor of Philosophy

Department of Mathematics

City Univeristy

September 1995

Contents

ACKNOWLEDGEMENTS

A big thank you must go to my supervisor Professor J Mathon for first of all believing in me before starting this thesis. But especially for all the help, advice and time taken to explain topics to me whilst conducting my research. It would be remiss of me not to also thank Dr M Villeret, Dr J Castro and Dr A Umerski for their help as well.

Financial support was provided by the Science and Engineering Research Council and is gratefully acknowledged.

Computers funded by SERC/EPSRC grant GRJ29923

Abstract

A layer within a magnetic multilayer may exhibit properties radically different from its bulk properties, when the thickness of the layers is very small. It has been found experimentally that the magnetic moments of magnetic layers separated by a thin non-magnetic spacer spontaneously align either ferromagnetically or antiferromagnetically, depending on the thickness of the spacer layer. This type of magnetic interaction is called exchange coupling J(N) and is observed to oscillate as a function of the spacer thickness N. The purpose of this thesis is to give details of one theoretical approach which can be used to model exchange coupling in magnetic multilayers. Currently three different models have been employed and we start by giving a brief details of these three methods. In the remaining Chapters we develop our preferred model, the Quantum well theory. A theory for the one band model at zero temperature is developed by expressing J(N) in terms of the local Green's functions of the trilayer. The local Green's functions are obtained using a very versatile method which can be applied to obtain the local Green's function of any atomic plane in any type of multilayer. The band structure used to describe the trilayer is the tight-binding model. A numerical approach is developed to compute the exchange coupling. This requires a considerable amount of time to compute rendering it impractical to use. Therefore we develop an asymptotic expansion of J(N) which relates the exchange coupling to the spacer layer and enables us to compute J(N) in a reasonable amount of time. We consider a single example of exchange coupling for a one band trilayer to ensure the two methods are in agreement with each other. The one band model is useful to help understand the physical mechanisms in exchange coupling but its applications are limited. We therefore generalize all the models and methods of computation so that we can compute the exchange coupling for a two band trilayer. Here we can fully take into account the hybridization between the bands. An investigation into what effect the hybridization in the ferromagnetic and spacer layers has on the exchange coupling is given. Due to the possibility the exchange coupling may oscillate with two periods for the two band trilayer we finally consider a single example of double-period exchange coupling.

Chapter 1

General background

1.1 Introduction

An area that has attracted a considerable amount of theoretical and experimental work recently is magnetic multilayers. Magnetic multilayers are structures which consist of very thin alternating layers of materials with differing magnetic properties. What has stimulated the interest is the possibility a layer in the structure may have very different properties from its bulk properties. This occurs when the layers are very thin ie of the order of several atomic planes.

Magnetic multilayers are usually constructed using the technique called molecular beam epitaxy (MBE), for further details on MBE see Ref [1]. MBE works by depositing an evaporated metal onto a substrate at a controlled rate thereby forming thin films or layers. Advances in this state of the art technique has enabled scientists to grow very good magnetic multilayers. Under certain conditions crystals can

be grown at the rate of one atomic plane which can result in structures containing sharp interfaces between layers. Also the crystals contain very few impurities.

Of all the possible magnetic multilayers one of the more interesting and more commonly studied structures at the moment is the trilayer. This is a thin non-magnetic metal (spacer layer) sandwiched between two magnetic layers, for example Co/Cu. It has been found experimentally, Refs [2] - [6] that the magnetic moments of the magnetic layers spontaneously align either ferromagnetically or antiferromagnetically depending on the thickness of the spacer layer. This type of interaction between the layers oscillates as a function of the spacer layer thickness and is called exchange coupling.

It has also been observed experimentally Refs [3] and [7] that the resistance of the multilayer, when a current is passed in the direction parallel to the layers, is much higher when the magnetic moments are aligned antiferromagnetically (antiparallel) compared to the ferromagnetic (parallel) configuration. Applying a magnetic field can change the configuration from antiferromagnetic to ferromagnetic and therefore also the resistance of the multilayer. This effect is called "giant magnetoresistance". In this way one can see a direct relationship between the giant magnetoresistance and exchange coupling of a magnetic multilayer. One reason giant magnetoresistance in magnetic multilayers has attracted so much attention is it can be exploited to read information from a magnetic computer disc and increase its storage capacity.

Information on a magnetic computer disc is stored in the form of small magnetised regions arranged in concentric circles. The conventional reading head reads

information from the disc by sensing the rate of change of the magnetic field as the disc rotates. The speed of a track decreases towards the centre of the disc so to compensate for this effect and maintain the same rate of change throughout the disc, storage density on the inner tracks must be decreased. On the other hand magnetoresistive sensors sense the strength of the magnetic field rather than its rate of change. Data can therefore be stored at the same high density throughout the disc without the need to compensate for the slower moving centre tracks and the total storage capacity of the disc is increased.

The aim of this Chapter is to explain the underlying physical mechanisms that cause exchange coupling in magnetic multilayers. We start this process in Section 1.2 by explaining what makes transition metals such as Fe ferromagnetic. Currently three different theoretical methods have been employed to describe oscillatory exchange coupling in magnetic multilayers and these are outlined in Section 1.3. Finally in Section 1.4 we give a general definition of the Green's function of an operator. Here we pay particular attention to the derivation of the density of states using the Green's function method as it is one of the main quantities used in the quantum well theory of exchange coupling. We use the quantum well theory to model exchange coupling in magnetic multilayers in this thesis.

In Chapter 2 we explain how to compute the exchange coupling for a single orbital trilayer using the quantum well theory. Here the exchange coupling is defined in terms of the local density of states of the trilayer, which is obtained using the Green's function method. Using the local Green's functions a numerical and analytic

approach are developed to compute the exchange coupling. As this situation has already been documented its inclusion in this thesis is to help understand all the techniques employed when computing the exchange coupling. We also give the first explicit proof that Fourier analysis can be employed in the analytic approach by obtaining an analytic expression for the local Green's functions of the trilayer.

In Chapter 3 we generalize the single orbital model of exchange coupling and for the first time we compute the exchange coupling for a two band trilayer. We start by obtaining a new expression for the local Green's function of the two band trilayer, as the exchange coupling is defined in terms of these Green's functions. The analytic and numerical approaches, as used in the one band model, are then generalized so that we can compute the exchange coupling. Finally for the first time the situation of double period exchange coupling is considered.

1.2 Ferromagnetism in transition metals

To understand magnetism in magnetic multilayers we first need to understand what makes bulk transition metals such as Fe, Ni and Co ferromagnetic. Ferromagnetism in transition metals can be described using the classical Stoner-Wohlfarth model Ref [8] the three main ingredients of which are:-

- The main carriers of magnetism in ferromagnetic transition metals are electrons in the 3d bands.

- The distribution of these electrons, called itinerant electrons, is determined by the band structure. $D(E_f)$ the density of states at the Fermi energy E_f being the key quantity.

- The interaction between the itinerant electrons may be described by a molecular field which is proportional to the magnetisation. The associated energy per atom is

$$E_M = -\frac{Un^2M^2}{4},$$

where n is the number of electrons per atom, U the interaction parameter and M is the relative magnetisation.

When $D(E_f)$ is high enough and U is strong the Stoner criterion of $UD(E_f) > 1$ is satisfied. The energy bands for the up and down spin carriers become split resulting in an imbalance in the number of up and down spin electrons and spontaneous magnetisation M.

A microscopic basis of the Stoner model of ferromagnetism was provided by Hubbard Ref [9] and [10] and the Hubbard model remains the best theoretical framework for discussing excited states in a ferromagnet. We now outline the Hubbard model.

1.2.1 Hubbard model

The more mobile s-band electrons in transition metals are free electron like and can be adequately modelled using the free electron gas model. These electrons are more responsible for the transport properties and contribute little to magnetism. The carriers of magnetism are "holes" in the d-band which contains five sub-bands. Unfortunately the free-electron gas does not provide a good model for these bands. Rather one requires a theory of correlations which adequately takes into account the atomistic nature of the solid and in particular the d-band electrons. In this thesis we adopt the itinerant electron model also referred to as the band model to describe the d-band.

The electron charge density in a d-band is concentrated near the nuclei of the solid and sparse between the atoms, making it possible to speak with some meaning of an electron being "on" a particular atom. This gives rise to the possibility of using the localized spin model also referred to as the atomic model to describe the d-band electrons. It is in fact found experimentally that d-band electrons of transition metals exhibit behaviour of both the band model and the atomic model. Treating the electrons using the band model where they move rapidly one may correlate their motion in such a manner as to give properties of the atomic and band theory. In

this way one may now understand how electrons can exhibit both types of behaviour simultaneously.

The band model used is the tight-binding approximation which is widely accepted to be useful for describing the energy band of the partially filled d-shells of transition metals. The electron-electron interactions are treated in the Hartree-Fock approximation. To be able to model the d-band electrons we first need the Hamiltonian. The complete Hamiltonian is very complicated and too difficult to handle so a simple model Hamiltonian therefore has to be built. We use the Hubbard Hamiltonian as in Ref [10] and it is

$$H = \sum_{ij\mu\nu\sigma} T_{ij}^{\mu\nu} C_{i\mu\sigma}^{\dagger} C_{j\nu\sigma} + \frac{1}{2} \sum_{ijkl\mu\nu\eta\zeta} \sum_{\sigma\sigma'} \left(i\mu\sigma j\nu\sigma' \left| \frac{1}{r} \right| k\eta\sigma l\zeta\sigma' \right) C_{i\mu\sigma}^{\dagger} C_{j\nu\sigma'}^{\dagger} C_{l\zeta\sigma'} C_{k\eta\sigma}, \tag{1.1}$$

where $C_{i\mu\sigma}^{\dagger}$ and $C_{i\mu\sigma}$ are the creation and annihilation operators for an electron at site R_i with spin σ in an orbital μ. The band structure enters through

$$T_{ij}^{\mu\nu} = \int \phi_{\mu\sigma}^{*}(r - R_i) \left[-\frac{\hbar^2}{2m} \nabla^2 + V(r) \right] \phi_{\nu\sigma}(r - R_i) dr^3, \tag{1.2}$$

which determines the band structure in the tight-binding approximation. V(r) is the nuclear periodic potential and

$$\begin{aligned} \left(i\mu\sigma j\nu\sigma' \left| \frac{1}{r} \right| k\eta\sigma l\zeta\sigma' \right) &= e^2 \int \phi_{\mu\sigma}^{*}(r - R_i) \phi_{\nu\sigma'}^{*}(r' - R_j) \frac{1}{r - r'} \times \\ &\quad \phi_{k\sigma}(r - R_k) \phi_{l\sigma}(r' - R_l) dr^3 dr'^3. \end{aligned} \tag{1.3}$$

Here $\phi_{\mu\sigma}(r - R_i)$ is the Wannier wave function of the electron on site R_i in an orbital μ with spin σ.

The first term in the Hamiltonian given in Equation 1.1 represents the ordinary band energies of the electrons and the second term their interaction energy. It is

now possible to begin the simplifying approximations. On the assumption that the bandwidth is going to be small the Wannier wave function will form an atomic shell which is small in radius when compared with the inter-atomic spacing. In this circumstance it may be seen that the integral $\left(ii\left|\frac{1}{r}\right|ii\right) = U$ in Equation 1.3 is much greater in magnitude than any of the other interaction terms and suggests we can neglect all other terms as they do not contribute significantly to the interaction. Also we neglect degeneracy ie we can drop the band indices and the model reduces to a simple single orbital model. Making these approximations leads to the Hamiltonian of Equation 1.1 being reduced to

$$H = \sum_{ij\sigma} T_{ij} C^{\dagger}_{i\sigma} C_{j\sigma} + \frac{U}{2} \sum_{i\sigma} n_{i\sigma} n_{i-\sigma}, \tag{1.4}$$

where $n_{i\sigma} = C^{\dagger}_{i\sigma} C_{i\sigma}$ is the occupation number , T_{ij} the hopping integral and the Wannier function is related to the Bloch operator $C^{\dagger}_{k\sigma}$ by

$$C^{\dagger}_{i\sigma} = \frac{1}{\sqrt{N}} \sum_{k} C^{\dagger}_{k\sigma} \exp\left(-ikR_i\right). \tag{1.5}$$

1.2.2 Hartree-Fock approximation

All the main features of the Stoner model can be obtained by treating the Hubbard-Hamiltonian given by Equation 1.4 in the Hartree-Fock approximation. The Hartree-Fock approximation may be applied provided the bare interaction U is replaced by a weaker effective interaction parameter U^{eff}. An exhaustive study of all possible Hartree-Fock solutions is not investigated, attention is simply restricted to the class of solutions which may represent non-magnetic or ferromag-

netic states. This is achieved by "linearizing" the interaction terms in the Hubbard Hamiltonian of Equation 1.4 and amounts to replacing the term $n_{i\sigma}n_{i-\sigma}$ with $n_{i\sigma} < n_{i-\sigma} > + n_{i-\sigma} < n_{i\sigma} >$ where $< n_{i\sigma} >$ is the average expectation of $n_{i\sigma}$. The Hamiltonian can therefore be written as

$$H_{HF} = \sum_{ij\sigma} T_{ij} C^{\dagger}_{i\sigma} C_{j\sigma} + U^{eff} n_{\uparrow} n_{\downarrow}, \tag{1.6}$$

where $\frac{1}{2}\sum_{i\sigma} n_{i\sigma}n_{i-\sigma} \rightarrow n_{\uparrow}n_{\downarrow}$ using $n_{\uparrow} =< n_{i\uparrow} >$ and $n_{\sigma} = \sum_{\sigma} n_{k\sigma}$. The total energy in the Hartree-Fock approximation is given by

$$E_{HF} = \sum_{k\sigma} E_k n_{k\sigma} + U^{eff} n_{\uparrow} n_{\downarrow}. \tag{1.7}$$

Rewriting $U^{eff} n_{\uparrow} n_{\downarrow}$ as

$$U^{eff} n_{\uparrow} n_{\downarrow} = \frac{U^{eff}}{4} \left[(n_{\uparrow} + n_{\downarrow})^2 - (n_{\uparrow} - n_{\downarrow})^2 \right]$$

and then using Ref [11] we find that

$$\begin{aligned} U^{eff} n_{\uparrow} n_{\downarrow} &= \text{Const} - \frac{U^{eff}}{4}(n_{\uparrow} - n_{\downarrow})^2 \\ &= \text{Const} - \frac{U^{eff} M^2 n^2}{4}. \end{aligned} \tag{1.8}$$

Here

$$M = \frac{n_{\uparrow} - n_{\downarrow}}{n} \quad \text{is the relative magnetisation}$$

and

$$n = n_{\uparrow} + n_{\downarrow} \quad \text{is the total number of particles in the system.}$$

Equation 1.8 is in fact the expression for the additional energy of the system in the Stoner model. It follows using Ref [12] that

$$n_\sigma = \begin{cases} \dfrac{n(1+M)}{2} & if \quad \sigma = \uparrow \\ \dfrac{n(1-M)}{2} & if \quad \sigma = \downarrow \end{cases}$$

or

$$n_\sigma = \int_0^\infty D(E) f^\sigma(E) dE,$$

where

$$f^\sigma(E) = \frac{1}{1 + \exp\left(\frac{E-\mu^\sigma}{k_B T}\right)}$$

and D(E) is the density of states, μ^σ the chemical potential, k_B the Boltzmann constant and finally T is the temperature. The total energy in the "Stoner model" is given by

$$E^{Stoner} = \sum_{k\sigma} E_{k\sigma} n_{k\sigma} - \frac{U^{eff} M^2 n^2}{4}. \tag{1.9}$$

At T=0 this equation is equivalent to

$$E^{Stoner} = \int_0^{E_{f\uparrow}} E D(E) dE + \int_0^{E_{f\downarrow}} E D(E) dE - \frac{U^{eff} M^2 n^2}{4}, \tag{1.10}$$

where E_f is the Fermi energy for the σ spin band and

$$n_{\uparrow\downarrow} = \int_0^{E_{f\uparrow\downarrow}} D(E) dE. \tag{1.11}$$

The criterion for ferromagnetism is obtained by comparing the energy E^{Stoner} for small M at $T = 0$ with the paramagnetic energy E_0. It is found using Ref [12] that

$$E_M = E_0 + \frac{n^2 M^2 \left[1 - U^{eff} D(E_f)\right]}{4 D(E_f)}. \tag{1.12}$$

From this equation it can be seen that the system becomes ferromagnetic when

$$U^{eff} D(E_f) > 1, \tag{1.13}$$

which is known as the Stoner criterion.

For a strong ferromagnet ("strong" has nothing to do with the strength of the resultant magnetic moment) the Hartree-Fock ground state is an exact eigenstate since particles of the same spin do not interact in this model in accordance with the Pauli exclusion principle. The Pauli exclusion principle states that two electrons with the same spin cannot occupy the same orbital and therefore an electron with spin up say avoids an atom which is already occupied with another up spin electron. This can be visualised as the up spin band being completely full as in the case of Ni see Figure 1.1. If the Fermi level lies in both spin-bands then we have a weak ferromagnet as in the case of Fe see Figure 1.2.

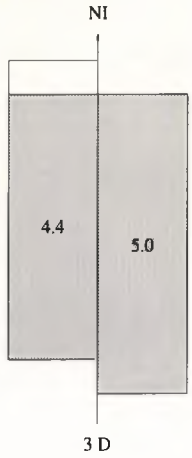

Figure 1.1: Schematic representation of the density of states of the d-band of the strong ferromagnet nickel. The total number of electrons in the down spin (left) and up spin (right) bands are also shown. The bands are filled up to the common Fermi level E_f.

Figure 1.2: Schematic representation of the density of states of the d-band of the weak ferromagnet iron. The total number of electrons in the down spin (left) and up spin (right) bands are also shown. The bands are filled up to the common Fermi level E_f.

1.3 Various theoretical models

Fabrication of good quality magnetic multilayers and the interesting magnetic properties they can possess has also stimulated a great deal of theoretical work. The theoretical work has sought to realistically model exchange coupling in magnetic multilayers thereby equipping us with the necessary tool to make predictions about aspects of exchange coupling such as the period of oscillations for example. It has also helped us to understand the physical mechanisms involved in exchange coupling in magnetic multilayers.

Currently three alternative approaches have been developed to model exchange coupling in magnetic multilayers. The first one, which we outline in Section 1.3.1, is based on local spin density functional theory. This method computes the exchange coupling whilst fully taking into account the local band structure and electron interactions in the magnetic multilayer. The second approach is the perturbation theory which treats the magnetic layers in a trilayer as magnetic monolayers weakly perturbing a non-magnetic host, this is described in Section 1.3.2. Finally in Section 1.3.3 we briefly outline the quantum well theory where we give details of how all the required formulae are derived. This is the model we adopt in this thesis to model exchange coupling in magnetic multilayers and full details of the how the exchange coupling is actually computed are given in the remaining Chapters of this thesis.

1.3.1 Local spin density functional theory

In this Section we briefly outline one approach for computing the exchange coupling in magnetic multilayers based on first principles for determining the total energy combined with a suitable scheme for calculating the local band structure within the magnetic mulitlayer.

Electrons in a real solid cannot be described by a wave function computed from a single particle Schrödinger equation

$$\left(-\frac{\hbar^2}{2m}\nabla^2 + U(r)\right)\psi_k(r) = E_k\psi_k(r), \tag{1.14}$$

independent of all other electrons because of the many-body interactions between the electrons.

Density functional theory Refs [13] and [14] provides an elegant framework in which the total energy can be obtained inclusive of all the electron-electron interactions. The total energy of an interacting electron gas is a unique functional of its charge density $n(r)$ and it is

$$E[n(r)] = T[n(r)] + U[n(r)] + E_{xc}[n(r)], \tag{1.15}$$

where $T[n(r)]$ is the kinetic energy of a non-interacting electron gas, $U[n(r)]$ is the potential energy and $E_{xc}[n(r)]$ is the exchange and correlation term. If $E_{xc}[n(r)]$ were known one could obtain the solution of the many-electron system. Since in practice these functionals are not known an approximation has to be made. The most common one used is the Local Spin Density Approximation (LSDA) of Ref [14] which uses E_{xc} for the homogeneous electron gas as an approximation to E_{xc}. The

great advantage of the density functional method lies in the fact that by using Ref [14] the system reduces to a single particle problem and the density n(r) can be written as

$$n(r) = \sum_i \psi_i^*(r)\psi_i(r), \tag{1.16}$$

where the wave function ψ_i are solutions of one particle equations

$$\left[-\frac{1}{2}\bigtriangledown^2 + V_{cr}(r) + \mu_{xc}(r)\right]\psi_i(r) = E_i\psi_i(r). \tag{1.17}$$

Here $V_{cr}(r)$ is the total Coulomb potential which is related to the charge density by Poisson's equation

$$-\bigtriangledown^2 U(r) = 4\pi\rho(r) \tag{1.18}$$

and $\mu_{xc}(r)$ is the local exchange correlation potential term which can be obtained from many-body theory. The local spin density functional method is then combined with a suitable scheme for calculating the local band structure within the magnetic multilayer and there are a variety of methods. One of these is the Green's function method of Korringa, Kohn and Rostoker (KKR) for planar defects, Refs [15] and [16]. Here the magnetic layer and neighbouring host planes are considered to be perturbations in an otherwise unperturbed non-magnetic host. A second method uses the atomic spheres approximation to perform self-consistent calculations on the band structure Refs [17] and [18]. A third method uses the Linearized Augmented Plane Wave (LAPW) technique Refs [19], [20] and [21]. Also tight-binding models can be used to provide a stationary approximation for self-consistent density functional theory Ref [22]. In all these models a starting density is constructed which

for example could take the bulk form for the magnetic and spacer layers. Using this density one can calculate the potential using Equation 1.17 and once the potential is known the wave functions can then be calculated. This in turn yields a new charge density

$$\rho(r) = e^2 \sum_i |\psi_i|^2 , \tag{1.19}$$

where the summation is over all occupied one-electrons in the metal. The new density is then fed back until self-consistency is achieved. For a layered system, as in the multilayer, the self-consistency has to be achieved for each atomic plane. For a magnetic multilayer with a large number of atomic planes this makes the problem computationally very difficult.

Using this method, the exchange coupling is calculated from the total energy difference between the antiferromagnetic and ferromagnetic configurations of the magnetic multilayer. Since the energy difference is several orders of magnitude smaller than the total energy itself, any inaccuracies or approximations will have a disproportionately large effect on the coupling. We can immediately see one problem of this theory is the accuracy of the results. Another is the prohibitive amount of time it takes to perform the self-consistent calculations has meant the calculations have been restricted to relatively small spacer thicknesses. Also because of the need to perform the calculations self-consistently it makes the model less transparent. This is in turn makes it more difficult to make predictions or gain insight into the mechanisms involved in exchange coupling. For all these reasons, fully self-consistent calculations for the whole magnetic multilayer have now been abandoned in favour

of "frozen potential" approximations Refs [15] and [17]. Here full bulk self-consistent calculations are performed for each layer in their bulk form and then "cut and paste" into the multilayer environment. In other words the effect of the local band structure deviating from its bulk behaviour around an interface is neglected.

1.3.2 Perturbation theory - RKKY

The next theoretical appproach we are going to outline which has been used to describe exchange coupling in magnetic multilayers is the Ruderman-Kittel-Kasuya-Yosida (RKKY) model. It began with much earlier theoretical and experimental work when dilute alloys consisting of a host metal combined with magnetic impurities were being considered. In practice it is very difficult to investigate experimentally the effects of a single magnetic impurity, rather one needs a sufficient number of impurities to be able to detect the effects they have on the host metal. The magnetic impurities should be far enough apart so that the magnetic structure no longer resembles a pure metal but close enough so that their exchange energies dominate other energies. A theory for the long range interaction between two magnetic impurities in a non-magnetic host metal is provided by the RKKY mechanism. The RKKY model predicts that there is an oscillatory long range interaction yielding ferromagnetic or antiferromagnetic coupled spins depending on their mutual distance apart L. It is the well known expression Ref [23]

$$J(L) = \frac{4A^2 m k_f^4}{8\pi^3 \hbar^2} \left[\frac{2k_f L \cos(2k_f L) - \sin(2k_f L)}{(2k_f L)^4} \right], \tag{1.20}$$

where k_f is the Fermi wave vector of the host metal and A is an adjustable parameter that describes the strength of the coupling.

This type of oscillatory behaviour bears close resemblance to the oscillatory exchange coupling between ferromagnetic layers separated by a non-magnetic metal spacer layer. The resemblance has inevitably lead to the application of the RKKY

theory so that it can describe the exchange coupling in magnetic multilayers as in Refs [24], [25] and [26] for example. The first step in the application of the RKKY model was to replace the single atomic magnetic impurities by magnetic atomic planes as described by Yafet in Ref [27]. The system now under consideration is the one shown in Figure 1.3.

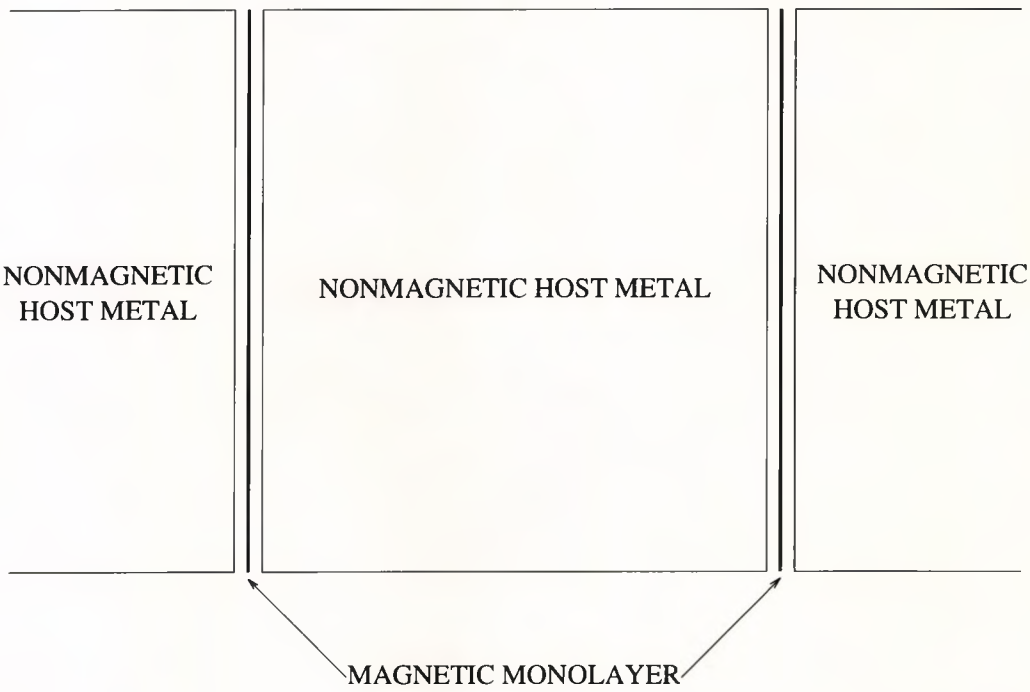

Figure 1.3: Diagram showing two ferromagnetic monolayers deposited in a non-magnetic host metal. Their mutual distance apart is z.

Exchange interaction energies of the magnetic monolayers are now calculated. The three dimensional free-electron system may be regarded as a pseudo one dimensional (1D) system because of the translational invariance in the plane parallel to the layers (xy - plane). Choosing the z-axis so that it goes through the observable

point r then the exchange function $J_s(z)$ is given by

$$J_s(z) \sim \int_z^\infty \frac{rdr}{r^4} \left[\sin(2k_f r) - 2k_f r \cos(2k_f r)\right], \tag{1.21}$$

where $rdr = \rho d\rho$ is the element of area in the xy plane at a constant z. Integrating Equation 1.21 by parts gives

$$J_s(z) \sim \frac{1}{2}\left[\left(\frac{\pi}{2} - Si(2k_f r)\right) - \frac{\cos(2k_f r)}{2k_f r} + \frac{\sin(2k_f r)}{(2k_f r)^2}\right]. \tag{1.22}$$

Here Si is the sine integral formula. At large z $\left[\frac{\pi}{2} - Si(2k_f r)\right]$ behaves asymptotically like $\frac{\cos(2k_f r)}{2k_f r} + \frac{\sin(2k_f r)}{(2k_f r)^2}$ and $J_s(L)$ becomes

$$J_s(L) \propto \frac{\sin(2k_f L)}{L^2}, \tag{1.23}$$

where L is the mutual distance apart of the two magnetic monolayers.

Examination of Equation 1.23 shows that by treating the model of magnetic impurities in the pseudo 1D limit leads to oscillatory exchange coupling between ferromagnetic layers separated by a non-magnetic metal spacer. Thus the RKKY theory appears to be a good candidate for describing the oscillatory interlayer coupling. Indeed it has given some insight into the origin of the observed oscillation periods and their relationship to the spacer layer. This is achieved even within the free-electron approximation.

Following Ref [25] the model consists of two ferromagnetic monolayers embedded in a non-magnetic metal as shown in Figure 1.3. The distance between the ferromagnetic monolayers is $z = (N + 1)a$, where a is the spacing between atomic planes and N is the number of atomic planes in the spacer. Experimentally the

magnetic layers are usually thicker than just the single atomic plane as used in the RKKY model. The justification for this approximation is the claim that exchange coupling is roughly independent of the thickness of the magnetic layers. We show in Section 3.1.2 that the exchange coupling can be influenced by the thickness of the magnetic layers, which is also demonstrated in Refs [28] and [29]. It transpires that the period of the oscillations is dependent on the spacer layer only, however the strength of the exchange coupling can be affected by the thickness of the magnetic layers. From this we can see one of the drawbacks of the RKKY model of exchange coupling in magnetic multilayers as it cannot take into consideration the thickness of the magnetic layers.

The magnetic layers are assumed to consist of spins S_i located on atomic position R_i of the host metal. One of the magnetic layers interacts with electrons of the host metal and induces a spin polarisation around it. This polarisation is propagated across the spacer and eventually interacts with the other magnetic monolayer. This results in an effective exchange interaction between the two magnetic monolayers. The exchange coupling can be split into two main aspects. One is the interaction between a ferromagnetic layer and the host's electrons and the other is the way the spin polarisation is propagated across the host. The RKKY model concentrates on the second paying particular attention to the oscillation periods. The exchange integral is defined by

$$I(R_{ij}) = -\frac{1}{2}\left(\frac{A}{V_0}\right)^2 \frac{V_0}{(2\pi)^3}\int d^3q\chi(q)\exp(iqR_{ij}), \tag{1.24}$$

where V_0 is the atomic volume and as before A is an adjustable parameter that

describes the strength of the coupling. The nonuniform susceptibility (in units of $2\mu_B^2$/atom) of the host metal is given by

$$\chi(q) = \frac{V_0}{(2\pi)^3} \sum_{n,n'} \int d^3k \frac{f(\epsilon_{n,k}) - f(\epsilon_{n',k+q+G})}{\epsilon_{n',k+q+G} - \epsilon_{n,k}}, \tag{1.25}$$

where $f(\epsilon)$ is the Fermi-Dirac function, the indices n and n' refer to the energy bands, G is a vector of the reciprocal lattice chosen so that $k+q+G$ belongs to the first Brillouin Zone (FBZ). The exchange coupling is

$$J = \frac{a}{V_0} S^2 \sum_{j \epsilon F_2} I(R_{0j}), \tag{1.26}$$

where 0 labels one site of the left magnetic monolayer which is taken to be the origin and F_2 denotes the right monolayer.

The integrals over q and k in Equations 1.24 and 1.25 are performed over the FBZ, which is not well adapted to the symmetry of the problem. Thus all functions of q and k are defined outside the FBZ by simply repeating them periodically. The integration can therefore now be performed on any unit cell of the reciprocal space. The advantage of using the prismatic auxillary zone is that the integration over the z axis and in plane components of the wave vector can be separated. The expression for the coupling becomes

$$J = -\frac{1}{2}\left(\frac{A}{V_0}\right)^2 S^2 \frac{a}{(2\pi)^3} \int_{-\pi/a}^{\pi/a} dq_z e^{iq_z z} \int_{2DBZ} d^2q_{||} \chi(q_{||}, q_z) \sum_{R_{||} \epsilon F_2} \exp(iq_{||} R_{||}). \tag{1.27}$$

The summation over $R_{||}$ in Equation 1.27 is zero unless $q_{||} = 0$. Thus the coupling can be expressed in the terms of the Fourier transform of the susceptibility $\chi(q_z) = \chi(q_{||} = 0, q_z)$ which can written as

$$J = -\left(\frac{A}{V_0}\right) S^2 \frac{a^2}{32\pi^4} \int_{2DBZ} B(k_{||}) d^2k_{||}, \tag{1.28}$$

where

$$B(k_{\|}) = \int_{-\pi/a}^{\pi/a} dk_z \int_{-\pi/a}^{\pi/a} dk_z' \frac{f(\epsilon_{k_{\|},k_z}) - f(\epsilon_{k_{\|},k_{z'}})}{\epsilon_{k_{\|},k_z} - \epsilon_{k_{\|},k_{z'}}} \exp^{i(k_z'-k_z)z}.$$

Using Ref [30] it is noted that the main contribution to the integrals in $B(k_{||})$ come from states close to the Fermi surface. $\epsilon_{k_{\|},k_z}$ and $\epsilon_{k_{\|},k_{z'}}$ are expanded up to first order about the Fermi energy level and the integrals are then performed using complex contour techniques. The integral over $k_{||}$ is then performed using the stationary phase approximation (SPA). The SPA states that the main contributions to the integrals comes from around the stationary points. Employing the SPA to calculate the integral yields

$$J(z) = -\left(\frac{A}{V_0}\right)^2 S^2 \frac{a^2}{16\pi^2\hbar^2 z^2} \sum_{\alpha} m_{\alpha}^* \sin(q_z^{\alpha} z + \psi_0) \bar{F}_{\alpha}(z,T), \tag{1.29}$$

where q_z^{α} is the spacer Fermi surface spanning vector in the direction perpendicular to the layer. The index 0 denotes the stationary points, ψ_0 the phase is equal to 0, $\frac{\pi}{2}$ or π when q_z^0 is a maximum, minimum or a saddle point respectively. m_{α}^* is the effective mass and it is

$$m_{\alpha}^* = \frac{2\hbar\sqrt{|\kappa_x^0 \kappa_y^0|}}{|v_z^{\mu}| + |v_z^{v}|},$$

where κ_x^0 and κ_y^0 are the combined principal curvature radii of the Fermi surface at the stationary point q_z^0. v_z^{μ} and v_z^{v} are the effective velocity.

The initial prediction of a period using the RKKY theory is much shorter than experimentally observed which would appear to invalidate the RKKY mechanism. However this apparent discrepancy can be removed using a simple argument. The spacer thickness $z = (N+1)a$ is not a continous variable and an effective much larger

period may be predicted from the discrete sampling. This effect is demonstrated in Refs [31] and [32] and is known as aliasing. In our work we have also noted that there appears to be both a short and long period in the oscillations of exchange coupling. The correct period being the one that takes into account the discrete nature of the spacer thickness.

In general the RKKY model gives an asymptotic analysis of the interlayer exchange coupling in magnetic multilayers which is only valid for larger spacer thicknesses. This is achieved by showing that oscillations are related to the geometry of the spacer Fermi surface. In this way it explains variations in the oscillations by the thickness and orientation of the spacer layer. However the amplitude of the oscillations enters through the unknown parameter A. So whilst the RKKY model can give some insight into oscillatory exchange coupling it does not provide a complete picture as the amplitude cannot be quantified. In the model we adopt, the quantum well theory, any factors that may affect any aspect of the exchange coupling are implicitly built into the model through its parameters thus providing a more complete picture than the RKKY model can. Also the RKKY model fails when there are bound states in a potential well formed in the trilayer which happens for Co/Cu for example.

1.3.3 Quantum well theory

In this Section we outline the quantum well theory of oscillatory exchange coupling in magnetic multilayers. This is the model we have adopted so for the sake of brevity only the main formulae are derived here. Full details of the methods of computation are given in the remaining Chapters of this thesis. This approach was developed by Edwards et al and further details can be found in Ref [33] and [34].

Quantum Well States

To help understand the mechanisms and origins of interlayer exchange coupling it is useful to consider what the structure of a trilayer looks like from a quantum mechanical viewpoint. In doing this let us first consider the case of two non-magnetic metals A and B which have different electron densities $n_A < n_B$ as shown in Figure 1.4.

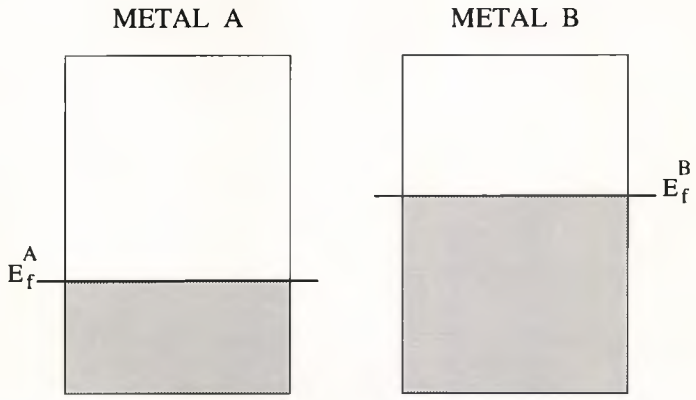

Figure 1.4: Schematic diagram of the electron densities of two non-magnetic metals, A and B, with two different Fermi energy levels.

For non-magnetic metals each electronic state is occupied by two electrons of

opposite spin. In other words the electron densities in Figure 1.4 represent either spin band. Joining the two non-magnetic metals A and B results in a common Fermi energy level with one of the bands being offset as shown in Figure 1.5.

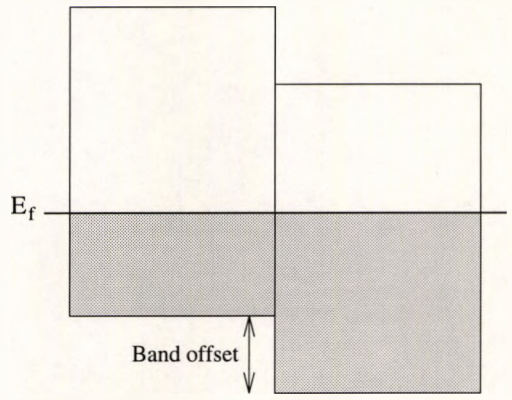

Figure 1.5: Schematic picture of the electron density of the two non-magnetic metals A and B once they have been joined together.

This schematic picture of the electron densities can be visualised if one regards the electrons as water in containers. Joining the two non-magnetic metals together is analogous to placing two containers side by side and allowing the water to move freely between the two containers. The situation that costs the least amount of energy and the one that will therefore occur naturally is when there is a common level of water in both containers. The electrons in metal A and B once joined behave in a similar fashion and result in a common level of electrons or common Fermi level in the multilayer. This process of the electrons forming a common Fermi level occurs in any multilayer. If we were to make a trilayer consisting of metal B sandwiched between two layers of metal A one would see from the schematic plots of the electron densities that the electrons in either spin band move within a potential

well as shown in as shown in Figure 1.6.

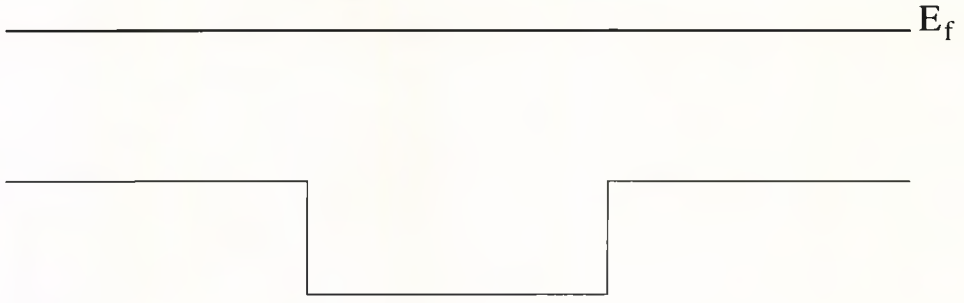

Figure 1.6: Diagram showing the potential well formed for a trilayer made up of metal B sandwiched between two layers of metal A.

Using the principle of the plots of the electron densities we can examine how electrons move across a trilayer with a non-magnetic spacer layer sandwiched between two ferromagnetic metals. For a ferromagnetic metal the up and down spin bands are split resulting in the spontaneous magnetic moment see Figures 1.1 and 1.2 in Section 1.2. The band offsets for the up and down spin electrons means the schematic plots are more complicated than before and they typically look like Figure 1.7.

Hence the electrons moving across the trilayer encounter spin dependent potential wells as shown in Figure 1.8.

Derivation of Main Formulae

The exchange coupling J(N) is defined to be the difference in total energies of the ferromagnetic and antiferromagnetic configurations of the trilayer ie it is

$$J(N) = \frac{E^{\uparrow\uparrow} - E^{\downarrow\uparrow}}{A}, \tag{1.30}$$

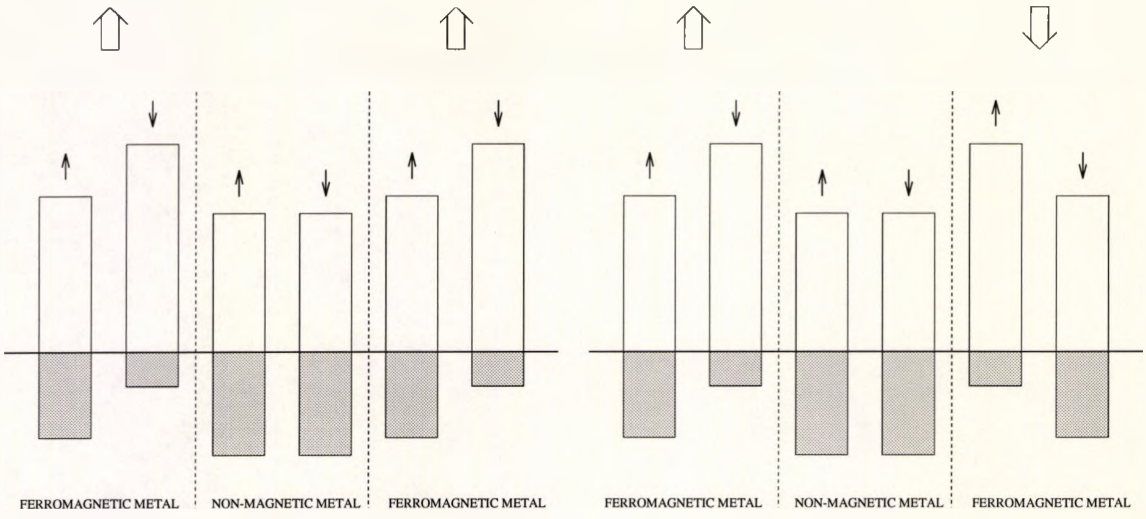

Figure 1.7: Schematic plots of the electron densities of a trilayer for the ferromagnetic (left picture) and antiferromagnetic (right picture) alignments of the magnetic multilayer. The four large arrows at the top of the picture show the magnetic moments of the magnetic moments of the magnetic layers and the small arrows denote either the up spin band $\uparrow$ or the down spin band $\downarrow$ of each layer.

where $E^{\uparrow\uparrow}$ and $E^{\downarrow\uparrow}$ are the total energies of the ferromagnetic and antiferromagnetic alignments respectively for a given spacer thickness N and A is the cross-sectional area. The total energy for a spin orientation s is obtained by integrating the product of the energy E with the density of states up to the common Fermi energy level E_f.

$$E^s_{TOT} = \int_{-\infty}^{E_f} E D^s(E,N) dE, \tag{1.31}$$

where $D^s(E,N)$ is the total density of states for particles of spin s in the trilayer having that configuration. The derivation of $D^s(E,N)$ using the Green's function method is given in Section 1.4. Before we can proceed, one important physical effect

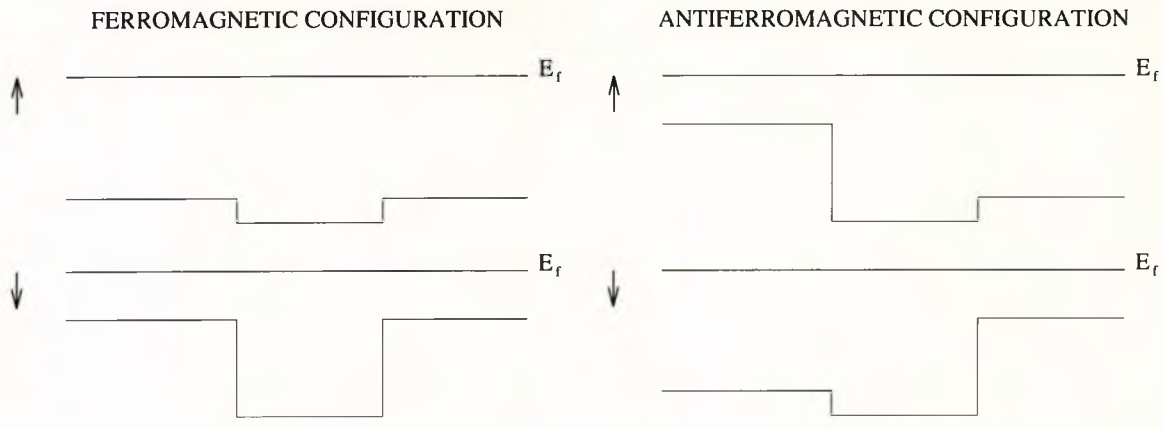

Figure 1.8: Diagram showing plots of the spin dependent (↑ up spin band, ↓ down spin band) potential wells seen by electrons in the trilayer for both the ferromagnetic and antiferromagnetic configurations.

has yet to be considered. As the thickness of the spacer layer N varies, the shape of the density curve also varies in complement. This can result in a change in the number of electrons per atom in the spacer layer. As the spacer layer must remain electrically neutral we need to either add or subtract the appropriate number of electrons to conserve the total charge. Adding or substracting electrons is performed at the Fermi energy level. Recalling our analogy of electrons with water this process of adding (subtracting) electrons can be viewed as pouring (removing) a little water into (from) the container. To take account of this effect we instead consider the thermodynamic potential $\Omega(N)$, where

$$\Omega^s(N) = \int_{-\infty}^{E_F} (E - E_f) D^s(E, N) dE. \tag{1.32}$$

Using this equation we can now write the exchange coupling as

$$J(N) = \frac{\left[\Omega^{\uparrow}(N) + \Omega^{\downarrow}(N)\right]_{FM} - \left[\Omega^{\uparrow}(N) + \Omega^{\downarrow}(N)\right]_{AF}}{A}, \tag{1.33}$$

where FM denotes the ferromagnetic configuration of the trilayer and AF denotes the antiferromagnetic configuration of the trilayer. The model we go on to describe in the following Chapters contain the following approximations:-

- The ferromagnets are taken to be semi-infinite. This approximation makes it reasonable to use the bulk parameters for the ferromagnets such as the position of the bands, the magnetic moment etc. However the models are described in such a way that finite ferromagnets could just as easily be considered, as happens experimentally.

- Bulk parameters are also used for the spacer layer. This is reasonable if the spacer thickness is large.

- Differences in the bulk parameters such as the position of the bands do occur around the interfaces in the trilayer. We neglect this effect in our calculations. However this could be fully taken into account using the adlayering procedure which is fully described in the later Chapters of this thesis.

- The total number of particles is conserved by using the thermodynamic potential instead of minimizing the total energies self-consistently.

1.4 Green functions

Green's functions or Green's functions of operators play a very important role in solid state theory and quantum mechanics. This arises from the fact that many operators such as the density of states (DOS) can be expressed in terms of Green's functions. In this way, we can obtain many physical properties of a system by using the information contained in a Green's function. The quantity we need to find in order to compute the oscillatory interlayer exchange coupling is the DOS. Therefore in this section we concentrate on how to compute the DOS using the Green's function method. For further details on Green's functions and their uses see Ref [35]

The general time-independent Schrödinger equation is

$$(EI - H)\psi = 0, \tag{1.34}$$

where $(EI - H)$ is formally a matrix of infinite size, E is a scalar, I is the unit matrix, H is the Hamiltonian matrix and ψ is the wave function. Leaving aside the trivial solution of $\psi = 0$, a non-trivial solution will exist if det(EI - H) = 0. For simplicity we now drop the unit matrix I. Let $|n>$ be the eigenfunction of the time-independent Hamiltonian operator H and E_n be its corresponding eigenvalue. We can therefore write

$$H|n>= E_n|n> . \tag{1.35}$$

The Green's function of the operator (E-H) is defined as

$$G = (E - H)^{-1}, \tag{1.36}$$

which exists if E $\neq$ eigenvalue of H. Expanding the Green's function in terms of the operator $|n>$ we obtain

$$G = \sum_n (E - H)^{-1} |n><n| \tag{1.37}$$

in the language of projection operators

$$G = \sum_n \frac{|n><n|}{E - E_n}, \tag{1.38}$$

where $|n>$ satisfies $(E_n - H)|n>= 0$, provided 0 is not an eigenvalue of H. We can now define the Green's functions $G^{\pm}$ by

$$G^{\pm} = (E - H \pm i\epsilon)^{-1}, \tag{1.39}$$

where ϵ is a small positive infinitessimal constant. By using Equation 1.37 we find that

$$G^{\pm}(E) = \sum_n \frac{|n><n|}{E - E_n \pm i\epsilon}. \tag{1.40}$$

Using the definition of the delta function $\delta(x)$ which is

$$\delta(x) = \frac{1}{\pi} \lim_{\epsilon \to 0} \left(\frac{\epsilon}{x^2 + \epsilon^2} \right) \tag{1.41}$$

and the Principal value $P(x)$ which is

$$P(x) = \lim_{\epsilon \to 0} \left(\frac{x}{x^2 + \epsilon^2} \right) \tag{1.42}$$

we obtain

$$G^{\pm}(E) = \sum_n |n><n| P(E - E_n) \pm i\pi\delta(E - E_n), \tag{1.43}$$

which gives

$$G^{+}(E) - G^{-}(E) = -2\pi i \sum_n |n><n|\delta(E - E_n). \tag{1.44}$$

Considering Equation 1.44 in the representation $|l>$ we find

$$< l|G^+ - G^-|l' >= -2\pi i \sum_n < l|n >< n|l' > \delta(E - E_n), \tag{1.45}$$

the diagonal elements of which are

$$< l|G^+ - G^-|l >= -2\pi i \sum_n < l|n >< n|l > \delta(E - E_n). \tag{1.46}$$

Summing over all the states l and interchanging the order of summation in the right hand side of the equation just above gives

$$\begin{aligned} \sum_l < l|G^+ - G^-|l > &= -2\pi i \sum_n \sum_l < l|n >< n|l > \delta(E - E_n) \\ \sum_l ImG_{ll}(E) &= -\pi \sum_n \delta(E - E_n), \end{aligned}$$

giving the following

$$-\frac{1}{\pi} TrImG(E) = \sum_n \delta(E - E_n). \tag{1.47}$$

In general the DOS of a system is the sum of delta functions of the exact eigenvalues

$$D(E) = \sum_n \delta(E - E_n), \tag{1.48}$$

therefore expressed in terms of the Green's function of an operator by using Equation 1.46 we find that the density of states is given by

$$D(E) = -\frac{1}{\pi} TrImG(E). \tag{1.49}$$

Chapter 2

Single band theory of exchange coupling in a trilayer

Introduction

The aim of this Chapter is to outline the method for calculating the exchange coupling of a trilayer made up of two semi-infinite ferromagnets separated by a non-magnetic spacer layer. We apply the model to a (001) trilayer with a single simple cubic tight-binding band where we include the effects of nearest neighbour hopping of electrons only. The restriction of the trilayer containing only a single band of electrons is lifted in the next Chapter when we generalize the model to two bands, but for the moment we confine ourselves to the case of a single band of electrons. Finally we consider the case when the temperature is zero.

The outline of this Chapter takes the following form. We start in Section 2.1 by explaining how to obtain the exact Green's function of an arbitrary atomic plane in

the spacer layer. Once this has been obtained we can express the exchange coupling $J(N)$ in terms of these Green's Functions, where N is the number of atomic planes in the spacer layer. Two different approaches are then developed to calculate the exchange coupling. In Section 2.2 we outline a numerical method for performing the calculations using the quantum well theory of Section 1.3.3. However the prohibitive time needed to perform all the calculations render this approach impractical although feasible. To overcome this problem we derive an analytic formula for the exchange coupling in Section 2.3 which is made possible by making some approximations. This method relates some aspects of the exchange coupling to the properties of the Fermi surface of the spacer layer.

2.1 Green's function of an arbitrary atomic plane in the spacer layer

Obtaining the Green's function of an arbitrary atomic plane in the spacer layer involves three steps:-

1. Obtaining the surface Green's function of the substrate.

2. Depositing atomic planes onto the substrate. (we call these atomic planes adlayers)

3. Joining together two substrates, with the appropriate number of adlayers deposited on them to create a trilayer.

We first deal with the problem of how to deposit adlayers onto the substrate. It might seem more logical to start with the surface Green's function of the substrate, especially when the answer will show that the surface Green's function of the substrate is required to proceed with the adlayering algorithm. However if the reader is patient there is a very good reason this.

2.1.1 Adlayering

Adlayering is simply the mathematical analogue of experimentally depositing atomic planes onto a substrate. We use the method set out in Refs [36] and [37] to find the exact Green's function of the surface atomic plane of many adlayers deposited onto a substrate. When formulating the adlayering procedure the parameters that describe the atomic potential and hopping integral of each adlayer are retained as variables of the procedure. This enables us to model many different structures as long as they have a simple cubic crystal lattice structure and a single band of electrons. We also consider the case of a semi-infinite substrate on which to deposit the adlayers. This is not a necessary condition in order to begin the recursive adlayering algorithm. The substrate can be any thickness as long as it contains at least one atomic plane. We start the adlayering procedure by considering the case of a single adlayer.

Single adlayer

Here we deal with how to deposit just one adlayer onto the substrate. This method of depositing an adlayer is applied again in the next subsection thereby enabling us to generalize the model so that we can deposit many adlayers not just the one. For the case of a single adlayer we have the situation as described in Figure 2.1.

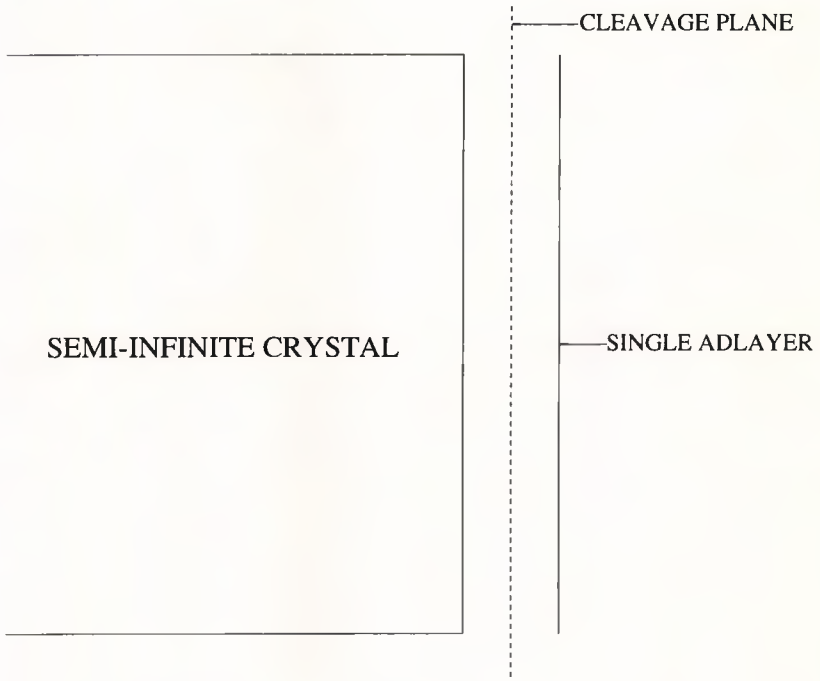

Figure 2.1: Diagram of a single adlayer or atomic plane deposited onto a semi-infinite crystal.

The cleavage plane shown in the diagram is just the mathematical device used to disconnect the adlayer from the substrate. Once disconnected, electrons are not able to hop across the cleavage plane. The adlayer is then reconnected to the substrate

using Dyson's Equation, which is

$$G^1(m,n) = G^0(m,n) + \sum_{p,q} G^0(m,p)W(p,q)G^1(q,n), \tag{2.1}$$

where G^0 are the Green's functions of the system with the cleavage plane, G^1 are the Green's functions of the system without the cleavage plane and $W(p,q)$ describes the perturbation within the system.

Two types of perturbation are present and result from electrons being able to hop from atomic plane to atomic plane and the interaction of an atom with its four nearest neighbours in its particular atomic plane. In this particular case the only non-zero matrix elements are:-

$$\begin{aligned} W(0,1) &= < k_{||}, 0 \mid H \mid k_{||}, 1 > = T, \\ W(1,0) &= < k_{||}, 1 \mid H \mid k_{||}, 0 > = T \quad \text{and} \\ W(1,1) &= < k_{||}, 1 \mid H \mid k_{||}, 1 > = W_1 = E_1 + 2T(cos(k_x a) + cos(k_y a)). \end{aligned} \tag{2.2}$$

Here T is the hopping integral or potential for an electron to hop from atom to atom. $W(0,1)$ and $W(1,0)$ is the hopping of electrons from the substrate to the adlayer and vice versa. $W(1,1)$ is the hopping of the electrons from atom to atom in the adlayer, E_1 is the atomic potential of the adlayer and finally a is the inter-atomic distance.

Placing m=n=1 in Dyson's Equation, Equation 2.1 and taking account of the perturbation defined by Equation 2.2 gives the Green's function of the single adlayer

to be

$$G^1(1,1) = G^0(1,1) + W_1 G^0(1,1) G^1(1,1) + T(G^0(1,0) G^1(1,1) + G^0(1,1) G^1(0,1)).$$

In the presence of a cleavage plane the electrons are unable to hop from the adlayer to the substrate and vice versa, hence

$$G^0(1,0) = G^0(0,1) = 0.$$

The formula for the Green's function of the single adlayer therefore simplifies to

$$G^1(1,1) = G^0(1,1) + W_1 G^0(1,1) G^1(1,1) + T G^0(1,1) G^1(0,1), \tag{2.3}$$

where $G^0(1,1)$ is the Green's function of a single unconnected atomic plane and it is

$$G^0(1,1) = \frac{1}{E}. \tag{2.4}$$

Putting the result from Equation 2.4 into Equation 2.3 and simplifying leaves us with

$$G^1(1,1)\,(E - W_1) = 1 + T G^1(0,1). \tag{2.5}$$

The only term in Equation 2.5 we do not yet know is $G^1(0,1)$. This is found by setting m=0 and n=1 in Dyson's Equation, Equation 2.1 and taking account of the perturbation. We therefore find that

$$G^1(0,1) = T G^0(0,0) G^1(1,1),$$

where $G^0(0,0)$ is the surface Green's function of the substrate which we call G^s. Its computation is not needed to explain the adlayering procedure so we just retain

G^s as one of the parameters of the algorithm. Its calculation is fully explained in Section 2.1.2, so

$$G^0(0,0) = G^s. \tag{2.6}$$

Using the solution of $G^1(0,1)$ and Equation 2.6 we find that the Green's function of a single adlayer is

$$G^1(1,1) = \frac{1}{E - W_1 - T^2 G^s}, \tag{2.7}$$

where

$$W_1 = E_1 + 2T(cos(k_x a) + cos(k_y a)).$$

We now have a relationship for the exact Green's function of a single adlayer, albeit in terms of the surface Green's functon of the substrate G^s.

Multi-adlayering

The process of depositing many adlayers onto the substrate is the same as depositing just one adlayer, the only difference is the process is repeated until the required number of adlayers have been deposited.

The Green's function of the second adlayer is found by treating our single adlayer deposited onto the semi-infinite crystal as the "substrate". Another adlayer is then deposited on top of the single adlayer in exactly the same way as before. Thus setting $m = n = 2$ in Dyson's Equation and taking account of the perturbation within the system we find that

$$G^2(2,2) = \frac{1}{E - W_2 - T^2 G^1(1,1)}, \tag{2.8}$$

where

$$W_2 = E_2 + 2T(cos(k_x a) + cos(k_y a))$$

and E_2 is the atomic potential of the second adlayer. The process of depositing adlayers can be repeated for as long as required until after N steps we find that

$$G^N(N,N) = \frac{1}{E - W_N - T^2 G^{N-1}(N-1,N-1)}, \tag{2.9}$$

where

$$W_N = E_N + 2T(cos(k_x a) + cos(k_y a))$$

and E_N is the atomic potential of the N th adlayer. $G^N(N,N)$ is the surface Green's function of N adlayers deposited onto a substrate, as shown in Figure 2.2 and $G^{N-1}(N-1,N-1)$ is the surface Green's function of N-1 adlayers deposited onto the substrate.

2.1.2 Surface Green's function of a semi-infinite crystal

In the previous section we described the deposition of adlayers onto a substrate where the substrate is a semi-infinite crystal. In order to be able to begin the adlayering procedure we first need to find the surface Green's function of the semi-infinite crystal, which we labelled G^s. Kalkstein and Soven have outlined one approach to finding G^s, which is described in Ref [38]. However there is a more direct way of finding G^s using the adlayering algorithm and it is this direct approach that we outline here, see also Ref [39]. Hence the reason for explaining the adlayering procedure first.

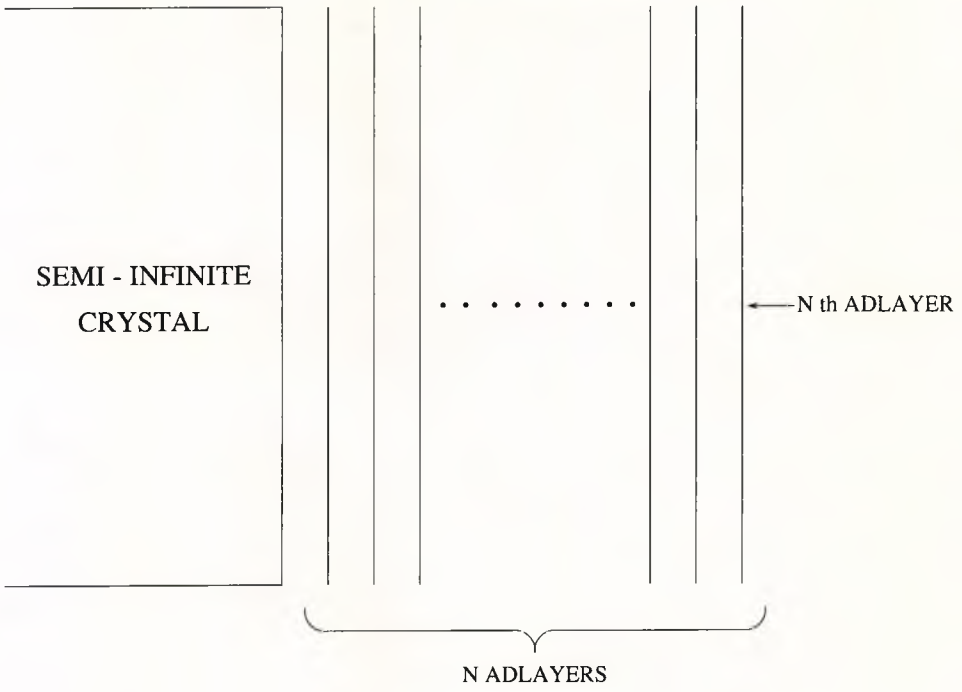

Figure 2.2: Diagram showing N adlayers or atomic planes deposited onto a semi-infinite crystal.

If we were to deposit an adlayer of the same material as the semi-infinite crystal onto the crystal it leaves us again with just a semi-infinite crystal. Therefore the Green's function of the single adlayer $G^1(1,1)$ is equal to the surface Green's function of the semi-infinite crystal G^s. Taking the Green's function of the single adlayer defined by Equation 2.7 we have

$$G^1(1,1) = \frac{1}{E - W_1 - T^2 G^s}.$$

By setting

$$G^1(1,1) = G^s$$

and

$$\omega = E - W_1 = E - E_s - 2T(cos(k_x a) + cos(k_y a)),$$

where E_s is the on-site energy of the substrate we obtain

$$G^s = \frac{1}{\omega - T^2 G^s}.$$

This leads to a quadratic equation in G^s the solution of which is

$$G^s = \frac{\omega}{2T^2} \pm \frac{\sqrt{\omega^2 - 4T^2}}{2T^2}. \tag{2.10}$$

At this point it is useful to note that the complex variable ω is properly denoted by $\omega + i\delta$ where δ is a very small positive constant. Using this we can rearrange the solution of the quadratic to give

$$G^s = \frac{\omega}{2T^2} \pm \frac{\sqrt{\omega^2 - 4T^2}}{2T^2} + \frac{i\delta}{2T^2}\left\{1 \pm \frac{\omega}{\sqrt{\omega^2 - 4T^2}}\right\}. \tag{2.11}$$

The only problem that now remains is which branch of the solution to the quadratic do we take? To help us determine this we use the density of states, which is

$$D^s(E, k_{||}) = -\frac{1}{\pi} \sum_{k_{||}} ImG^s(E, k_{||}) \tag{2.12}$$

and consider the situation when we are either inside or outside the band.

Let us first consider when we are inside the band, which occurs when $\omega^2 < 4T^2$. Here it can be seen from Equation 2.10 that G^s is naturally complex. If we let $\delta \to 0$ in Equation 2.11 then we obtain

$$G^s = \frac{\omega}{2T^2} \pm \frac{i\sqrt{4T^2 - \omega^2}}{2T^2}, \tag{2.13}$$

for the surface Green's function of a semi-infinite crystal. When we are inside the band the density of states must be positive. By using the formula for the density of states it is easy to see that the negative branch of the solution should be taken to obtain a positive density of states.

Now we consider the case when we are outside the band, which occurs when $\omega^2 > 4T^2$. Here the density of states is zero and this can be verified by letting $\delta \rightarrow 0$ in Equation 2.11. Therefore the density of states cannot help determine which branch of the solution to take when we are outside the band. Instead we need to look at the real part of the Green's function. Outside the energy band the real part of the Green's function should tend to zero as $\omega \rightarrow \pm\infty$. If we let $\delta \rightarrow 0$ and $\omega \rightarrow \pm\infty$ in Equation 2.11 then we find that

$$ReG^s \rightarrow \frac{\omega}{2T^2} \pm \frac{|\omega|}{2T^2}. \tag{2.14}$$

Equation 2.14 shows that when $\omega < 0$ the positive branch of the solution has to be taken to obtain a zero ReG^s. Alternatively when $\omega > 0$ the negative branch of the solution should be taken to obtain a zero ReG^s. Summarizing these results we have :-

$$\begin{aligned} G^s &= \frac{\omega}{2T^2} \pm \frac{\sqrt{\omega^2 - 4T^2}}{2T^2} \\ G^s &= \begin{cases} \text{negative branch} & \text{if} \quad \omega^2 < 4T^2 \\ \text{positive branch} & \text{if} \quad \omega^2 > 4T^2 \quad \text{and} \quad \omega < 0 \\ \text{negative branch} & \text{if} \quad \omega^2 > 4T^2 \quad \text{and} \quad \omega > 0, \end{cases} \end{aligned} \tag{2.15}$$

where

$$\omega = E - E_s - 2T(cos(k_x a) + cos(k_y a)).$$

2.1.3 Joining

To calculate the exchange coupling of a trilayer we need to obtain the Green's function of every atomic plane in the spacer layer that is embedded between two semi-infinite ferromagnetic crystals. To find the Green's function of the n th plane out of N planes in the spacer layer we use the method set out in Refs [37] and [39]. We start by passing a cleavage plane between the n th and n+1 st atomic plane in the spacer layer. As in the adlayering procedure, the cleavage plane is just a mathematical device used to "cut" the trilayer and it effectively separates the structure into two independent crystals, which is shown in Figure 2.3.

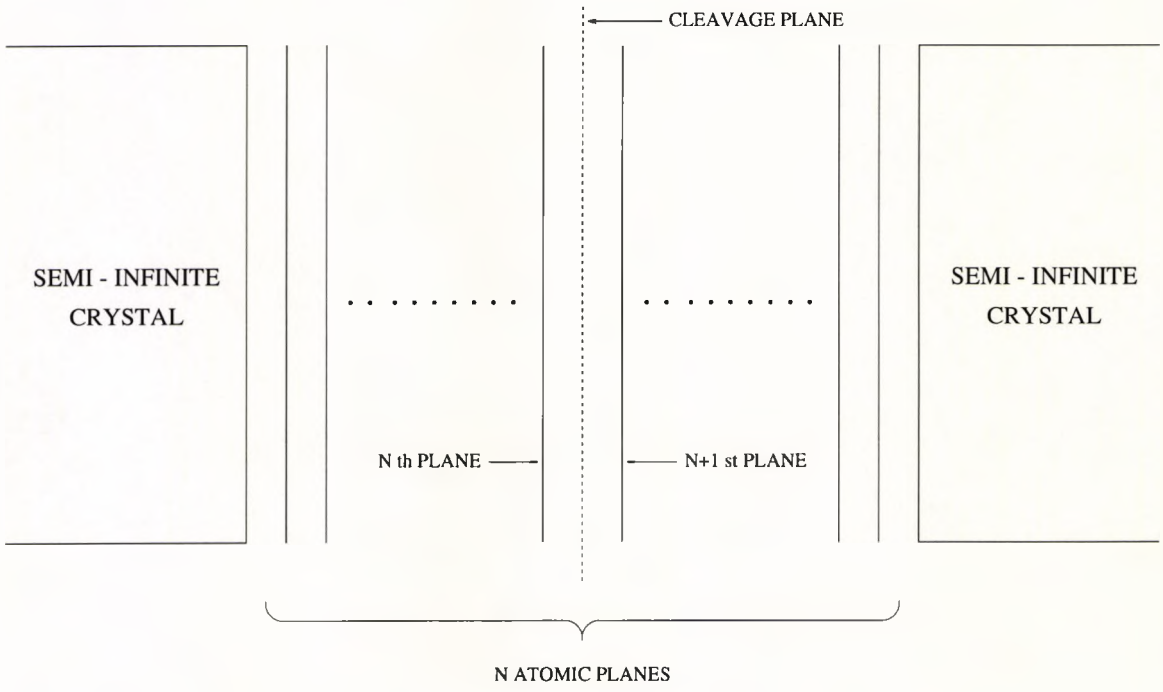

Figure 2.3: Diagram of a trilayer consisting of N atomic planes (spacer layer) sandwiched between two semi-infinite crystals.

The left and right hand crystals are now disconnected so there is no hopping of

electrons across the cleavage plane. The Green's functions for the cleaved crystals are therefore given by

$$G^{cl}(i,j) = \begin{cases} G^{Left}(i,j) & \text{if i,j } \epsilon \text{ L} \\ 0 & \text{if i } \epsilon \text{ L,j } \epsilon \text{ R and vice versa} \\ G^{Right}(i,j) & \text{if i,j } \epsilon \text{ R,} \end{cases} \tag{2.16}$$

where G^{cl} are the Green's functions of the system with the cleavage plane, G^{Left} are the Green's functions of the left independent crystal and G^{Right} are the Green's functions of the right independent crystal. To reconnect the two sides to create the trilayer we use Dyson's Equation again

$$G(i,j) = G^{cl}(i,j) + \sum_{p,q} G^{cl}(i,p)W(p,q)G(q,j), \tag{2.17}$$

where G are the Green's functions of the system without the cleavage plane and G^{cl} are the Green's functions of the system with the cleavage plane. In this case the only non-zero matrix elements describing the perturbation $W(p,q)$ are:-

$$\begin{aligned} W(n,n+1) &= < k_{\|}, n \mid W \mid k_{\|}, n+1 > = T \quad \text{and} \\ W(n+1,n) &= < k_{\|}, n+1 \mid W \mid k_{\|}, n > = T, \end{aligned} \tag{2.18}$$

where $W(n,n+1)$ is the potential for an electron to hop from the n th to the n+1 st atomic plane in the spacer layer and $W(n+1,n)$ is the potential for an electron to hop from the n+1 st to the n th atomic plane. Using this information and setting $i = j = n$ in Equation 2.17 we find that the Green's function of the n th atomic plane in the spacer layer is

$$G(n,n) = G^{cl}(n,n) + T(G^{cl}(n,n)G(n+1,n) + G^{cl}(n,n+1)G(n,n)).$$

$G^{cl}(n,n+1) = G^{cl}(n+1,n) = 0$ because the electrons cannot hop across the cleavage plane so this equation simplifies to

$$G(n,n) = G^{cl}(n,n) + TG^{cl}(n,n)G(n+1,n). \tag{2.19}$$

To complete the solution of Equation 2.19 we need to find $G(n+1,n)$. This is obtained by setting $i = n+1$ and $j = n$ in Dyson's equation, Equation 2.17 and taking account of the perturbation. Once these two tasks have been completed we obtain

$$G(n+1,n) = TG^{cl}(n+1,n+1)G(n,n). \tag{2.20}$$

After substituting the answer from Equation 2.20 into Equation 2.19 and simplifying we find that

$$G(n,n) = \frac{G^{cl}(n,n)}{1 - T^2 G^{cl}(n,n)G^{cl}(n+1,n+1)}. \tag{2.21}$$

$G^{cl}(n,n)$ is the Green's function of the surface atomic plane of the left independent crystal which consists of n adlayers deposited onto the left semi-infinite crystal. $G^{cl}(n+1,n+1)$ is the Green's function of the surface atomic plane of the right independent crystal which consists of N-n adlayers deposited onto the right semi-infinite crystal. These two Green's functions can be obtained using the adlayering procedure which is outlined in Section 2.1.1.

Equation 2.21 is the formula for the Green's function of an arbitrary atomic plane in the spacer layer containing a total of N atomic planes. When computing the exchange coupling we need to take the sum of all the Green's functions of all the atomic planes in the spacer layer. One great advantage of obtaining these local

Green's functions using the adlayering and joining methods is the joining requires little extra computer time over the adlayering. This is because the Green's function of each adlayer is obtained as it is deposited during the adlayering. These Green's functions can therefore be stored in a local array which can then be accessed as needed to do the joining.

2.2 Numerical computation of the exchange coupling J(N)

Using the quantum well theory in Section 1.3.3 we defined the exchange coupling in terms of the thermodynamic potentials $\Omega^s(N)$. We recall from Equation 1.33 that this relationship is

$$J(N) = \frac{\left[(\Omega^{\uparrow}(N) + \Omega^{\downarrow}(N))_{FM} - ((\Omega^{\uparrow}(N) + \Omega^{\downarrow}(N))_{AF}\right]}{A}, \tag{2.22}$$

where FM and AF denotes the ferromagnetic and antiferromagnetic configurations of the trilayer respectively and A is the cross-sectional area. We see from this equation that the final step in computing the exchange coupling is adding or subtracting the thermodynamic potentials, which is trivial. Therefore in this section we concentrate on how to compute the thermodynamic potential itself which is achieved using various numerical techniques. The formula for the thermodynamic potential Ω^s at zero temperature is

$$\Omega^s(N) = -\frac{1}{\pi}\sum_{k||}\int_{-\infty}^{E_f}\sum_{i=1}^{N}(E - E_f)ImG_{ii}^{i,s}(E, k_{||}, N)dE, \tag{2.23}$$

where N is the number of atomic planes in the spacer layer and the local Green's functions of the spacer layer $ImG_{ii}^{i}(E, k_{||}, N)$ are obtained by the methods as set out in Section 2.1. The suffix s denotes the spin band.

Strictly speaking the summation over i in Equation 2.23 should be over all atomic planes in the trilayer and not just the spacer layer. In other words the summation should run from i=$-\infty$ to i=∞ and not just i=1 to i=N. The local density of states of

the atomic planes below the surface atomic plane of the semi-infinite crystals rapidly approaches the bulk density of states as you move away from the interfaces with the spacer layer. Taking this into consideration it can be seen by using Equation 2.22 that the contribution to the exchange coupling arising from the ferromagnetic and antiferromagnetic configurations of the semi-infinite crystals tend to cancel each other out. This effect means that we only need to perform the summation of the Green's functions in the spacer layer only. However it does take several atomic planes for the local density of states of the ferromagnets to approach the bulk density of states but the contribution to the exchange coupling arising from this effect is minimal and can therefore be neglected.

During the formulation of the numerical evaluation of Ω^s we drop the dependence of the Green's functions on the parameters i and N for the sake of convenience. We first of all explain how to perform the energy integral by exploiting the complex nature of the Green's functions and then we discuss how to perform the summation over $k_{||}$.

2.2.1 Complex energy integration

Here we also drop the dependence of the Green's functions on $k_{||}$, again for the sake of convenience. We are therefore left with

$$\Omega^s = -\frac{1}{\pi}\int_{-\infty}^{E_f}(E - E_f)ImG(E)dE \tag{2.24}$$

for the formula for the thermodynamic potential. Once the energy integral has been completed all the parameters are reintroduced for the full solution.

The energy integral of the one-electron Green's functions can require a large number of energy points and a lot of computational time to achieve accurate results. This is especially true for layered systems with size quantized bound states. To help reduce the computational time we use the method in Ref [40] to replace the real energy integration with one in the complex energy plane.

The general Green's function $G(E)$ posseses singularities along the real axis only. $G(E)$ is therefore analytic in the whole complex energy plane except for the real axis. This analytic nature of the Green's functions enables us to use Cauchy's integral formula for complex functions. In order to compute Ω^s using Cauchy's formula we first consider the integral I, where

$$I = \int_{-\infty}^{E_f} ZG(Z)dZ,$$

Z is the complex variable $E + i\delta$ and G(Z) is a complex Green's function which is analytic in the whole complex energy plane except for the real axis. Integrating I along the contour shown in Figure 2.4 using Cauchy's integral formula yields

$$\oint ZG(Z)dZ = \oint ZG(Z)dZ + \oint ZG(Z)dZ = 0. \tag{2.25}$$

After simplifying Equation 2.25 we obtain

$$\oint ZG(Z)dZ = -\oint ZG(Z)dZ. \tag{2.26}$$

The left hand side of Equation 2.26 gives

$$\begin{aligned} \oint ZG(Z)dZ &= \int_{E_0}^{E_f} (E + i\delta)G(E + i\delta)dE + \int_{E_f}^{E_0} (E - i\delta)G(E - i\delta)dE \\ &= \int_{E_0}^{E_f} E(G(E) - G(E^*))dE \end{aligned}$$

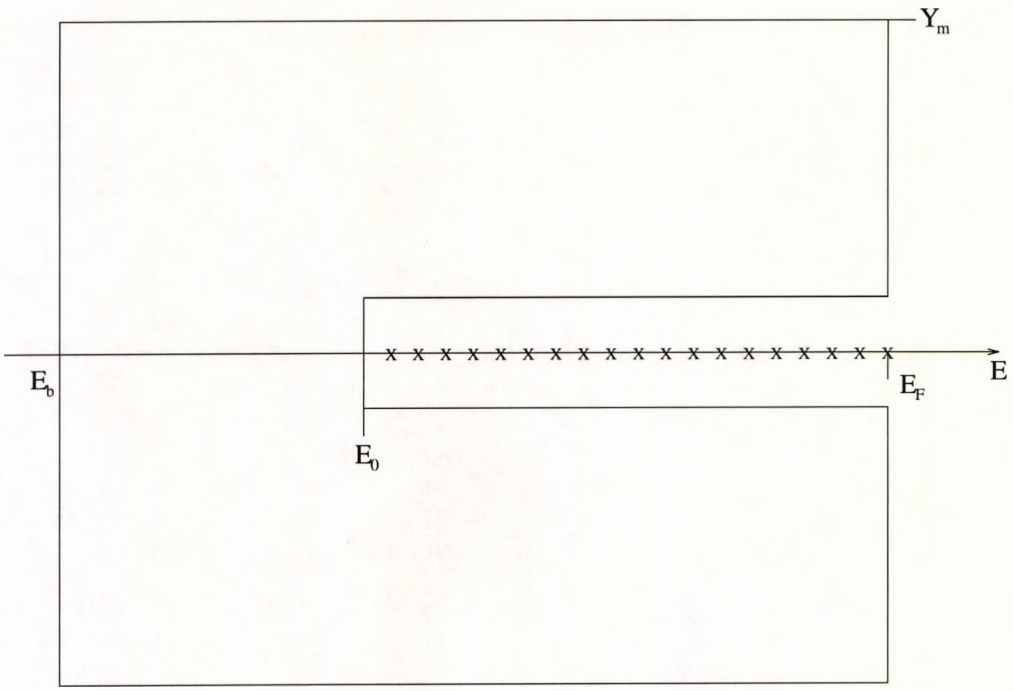

Figure 2.4: Diagram showing the full integration contour in the complex energy plane. E_f is the Fermi energy level, E_0 the bottom of the energy band, E_b is an arbitrary point that lies well below the bottom of the energy band and y_m is a constant that is greater than zero.

and by using $G(Z^*) = G^*(Z)$ we see that this can be further simplified to

$$\oint ZG(Z)dZ = 2i \int_{E_0}^{E_f} EImG(E)dE. \tag{2.27}$$

The right hand side of Equation 2.26 gives

$$\begin{aligned} -\oint ZG(Z)dZ &= \int ZG(Z)dZ + \int ZG(Z)dZ \\ &= \int (ZG(Z) - Z^*G^*(Z))\, dZ, \end{aligned}$$

which simplifies to

$$-\oint ZG(Z)dZ = 2iIm \int ZG(Z)dZ. \tag{2.28}$$

Therefore by using Equations 2.26, 2.27 and 2.28 we find that

$$\int_{E_0}^{E_f} EImG(E)dE = Im \oint ZG(Z)dZ. \tag{2.29}$$

Applying the answer in Equation 2.29 to the real energy integral for Ω^s we can replace the real energy integral with one in the complex energy plane along the contour shown in Figure 2.5.

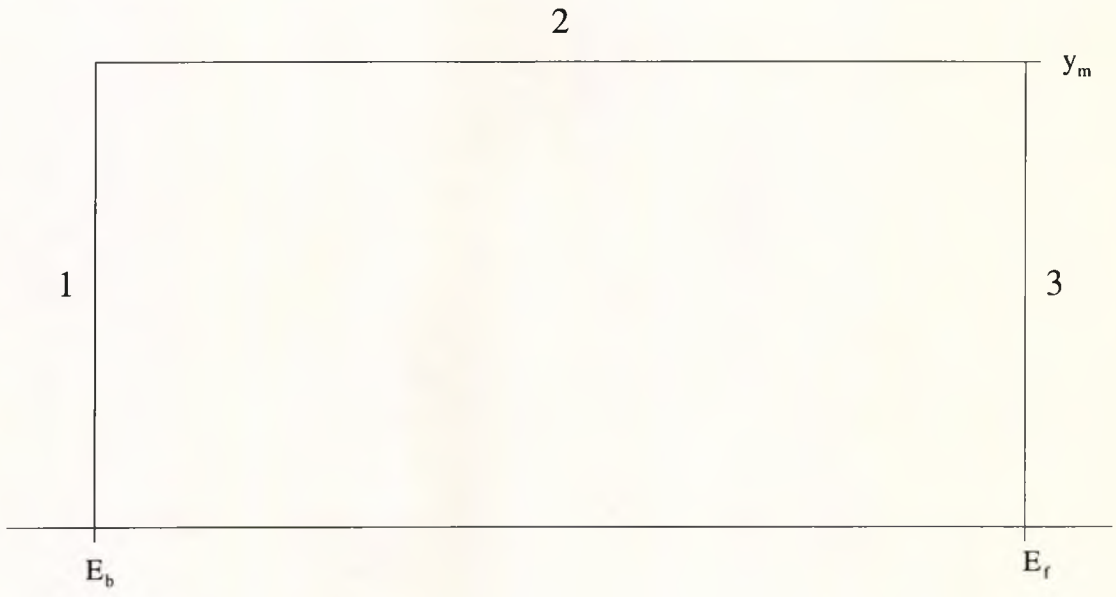

Figure 2.5: Diagram showing the reduced integration contour in the complex energy plane. E_f is the Fermi energy level, E_b is an arbitrary point that lies well below the bottom of the energy band and y_m is a constant that is greater than zero.

This gives

$$\Omega^s = -\frac{1}{\pi} Im \oint (Z - E_F)G(Z)dZ, \tag{2.30}$$

where E_f is the Fermi level, E_0 is the bottom of the energy band, E_b is less than E_0 and y_m is a constant that is greater than zero. The choice of y_m for the contour integral is arbitrary as the integral does not depend on the value of y_m. However the

time it takes to perform the integral is dependent on the length of the contour, the longer the contour the longer it takes to perform the integral. So taking this into consideration y_m should not be made too large. On the other hand for very small values of y_m the singularities of the Green's function $G(E)$ on the real axis could cause problems. The choice of y_m is therefore a compromise arrived at trial and error. Also the integral is not dependent on the path of the contour in Figure 2.5 and can take any route as long as it begins at E_b and ends at E_f.

Integrating Ω^s along 1

$$\begin{aligned} \text{Here} \quad Z &= E_b + iy \Rightarrow dZ = idy \\ Im\int(Z - E_f)G(Z)dZ &= Im\int_0^{y_m} i(E_b + iy - E_f)G(E_b + iy)dy \\ &= \int_0^{y_m}(E_b - E_f)ReG(E_b + iy) - yImG(E_b + iy)dy. \end{aligned} \tag{2.31}$$

Integrating Ω^s along 2

$$\begin{aligned} \text{Here} \quad Z &= x + iy_m \Rightarrow dZ = dx \\ Im\int(Z - E_f)G(Z)dZ &= Im\int_{E_b}^{E_f}(x + iy_m - E_f)G(x + iy_m)dx \\ &= \int_{E_b}^{E_f}(x - E_f)ImG(x + iy_m) + y_m ReG(x + iy_m)dx. \end{aligned} \tag{2.32}$$

Integrating Ω^s along 3

$$\begin{aligned} \text{Here} \quad Z &= E_f + iy \Rightarrow dZ = idy \\ Im\int(E - E_f)G(E)dE &= Im\int_{y_m}^{0}(E_f + iy - E_f)G(E_f + iy)idy \\ &= \int_0^{y_m} yImG(E_f + iy)dy. \end{aligned} \tag{2.33}$$

To complete the energy integral we add Equations 2.31, 2.32 and 2.33 which yields

the following result for Ω^s

$$\Omega^s = -\frac{1}{\pi}\sum_{i=1}^{N}\sum_{k||}\int_0^{y_m}(E_b - E_f)ReG^i_{ii}(E_b + iy, k_{||}, N)$$

$$+y(ImG^i_{ii}(E_f + iy, k_{||}, N) - ImG^i_{ii}(E_b + iy, k_{||}, N))dy$$

$$+\int_{E_b}^{E_f}(x - E_f)ImG^i_{ii}(x + iy_m, k_{||}, N) + y_m ReG^i_{ii}(x + iy_m, k_{||}, N)dx. \tag{2.34}$$

It should be noted that the dependence of the Green's functions on the parameters i,$k_{||}$ and N have been reintroduced for the full solution.

2.2.2 Summation over $k_{||}$

Now the energy integral has been completed we can proceed with the last task in computing Ω^s, the summation over $k_{||}$. The summation based directly on the wave vector from the two-dimensional Brillouin Zone (BZ) requires so much computer time that this approach is not practical. With this in mind several methods have been developed to overcome this problem and reduce the time needed to perform the summation. Of these we are going to use the approach set out by S.L. Cunningham in Ref [41].

The details of the summation method as prescibed by Cunningham are as follows. The BZ is first split into a uniform grid of 4NC(NC+1) squares, where NC is of the form 2^n and n is an integer. The special $k_{||}$ points used to perform the summation are the centre points of the squares in the grid, we therefore have 4NC(NC+1) points to perform the summation. These special points are assumed to be an excellent

approximation of the wave vector to the average value of this periodic function over the whole BZ. The rotational and reflection symmetry of the BZ is then exploited to reduce the number of points needed to perform the summation to the $\frac{1}{8}$ th of the BZ that is irreducible under symmetry. The symmetry of the BZ can be employed in any summation method to reduce the number of points and time needed to perform the summation. After using the symmetry of the BZ the number of $k_{||}$ points used to perform the summation is reduced to $\frac{NC(NC+1)}{2}$. A typical example of the reduced grid is given in Figure 2.6. When performing the summation all the off diagonal points are multiplied by the weight $\frac{1}{NC^2}$ and the diagonal points are multiplied by $\frac{1}{2NC^2}$. The diagonal points have a weight of only half the size of the off diagonal points because otherwise they will have been counted twice during the summation. Finally the number of $k_{||}$ points used to perform the summation is increased until the results converge to a required accuracy.

We find that Cunningham's method of performing the summation over $k_{||}$ is quite efficient. This can be demonstrated by comparing Cunningham's method with the direct summation over the BZ with periodic boundary conditions.

The direct summation takes the following form. The BZ is divided up into a uniform grid with N×N equally sized squares and we let N be any integer. The set of $k_{||}$ points that are used to perform the summation are the corner points of the grid, instead of the centre points. The weight for all the points is $\frac{1}{N^2}$. In common with Cunningham's prescription the number of points used to perform the summation is increased until the results converge to a required accuracy. From this

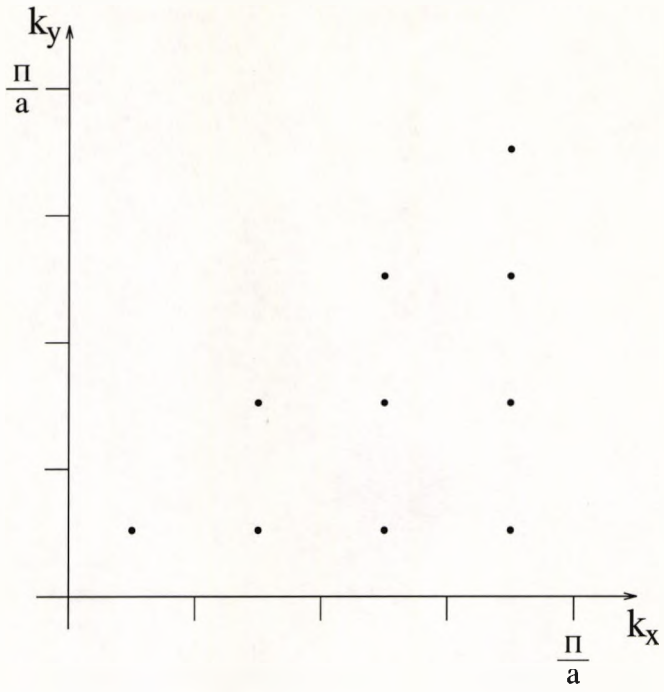

Figure 2.6: An example of the reduced grid of Cunningham points when NC=4.

we can see that the direct summation method differs from Cunningham's method in two fundamental ways, the type of grid used to split up the BZ and the position of the $k_{||}$ points in the grid.

The example we use to compare the efficiency of the Cunningham points is the calculation of the density of states for the surface atomic plane of a semi-infinite crystal. We set the hopping integral T of the crystal to 0.5 and the atomic potential to 0.

The density of states calculated using Cunningham points are shown in Figures 2.7 and 2.8. The curve in Figure 2.7 was obtained when $NC = 8$ which translates into a total of 36 points in the grid. The curve in Figure 2.8 was obtained

when NC was set equal to 32 with a corresponding 528 points in the grid which is when a 2 decimal point accuracy was obtained. Comparing the two graphs we see that using just 36 points already gives a clear indication as to what the results will converge to.

The density of states calculated using the direct summation method are shown in Figures 2.9 and 2.10. The curve in Figure 2.9 is obtained when $N = 6$ resulting in 36 points in the grid. The graph in Figure 2.10 was obtained by setting N equal to 50 which results in a grid of 2601 points which is when a 2 decimal point accuracy was achieved. This accuracy took approximately five times the number of points that Cunningham's method required.

We conclude from this example that Cunningham's approach is the more efficient of the two because it requires only a fifth of the points to achieve convergence when compared to the direct summation method. The point is further emphasized when we compare the results when 36 points were used for both the direct summation and Cunningham points. It is clear from the two graphs that the direct summation gives the less accurate results. Also this example only computes the density of states for the surface atomic plane of a semi-infinite crystal with a single-orbital band which is only a simply structured curve. It is likely for a more complex band structure that one would require considerably more than 5 times the number of points for the direct summation method when compared to Cunningham's method.

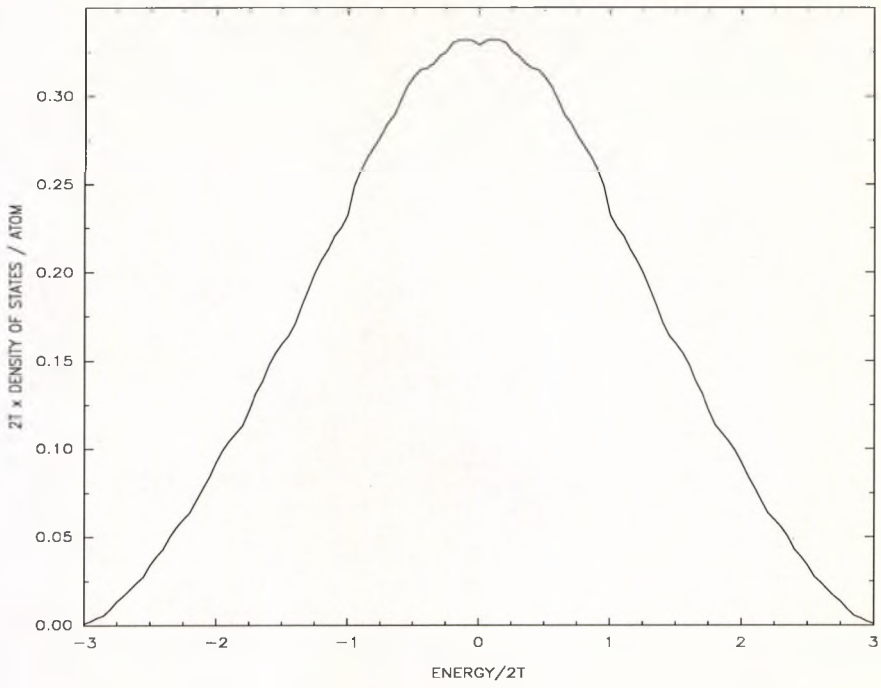

Figure 2.7: Density of states of the surface atomic plane of a semi-infinite crystal. $k_{||}$ summation is calculated using Cunningham's method. Here NC=8.

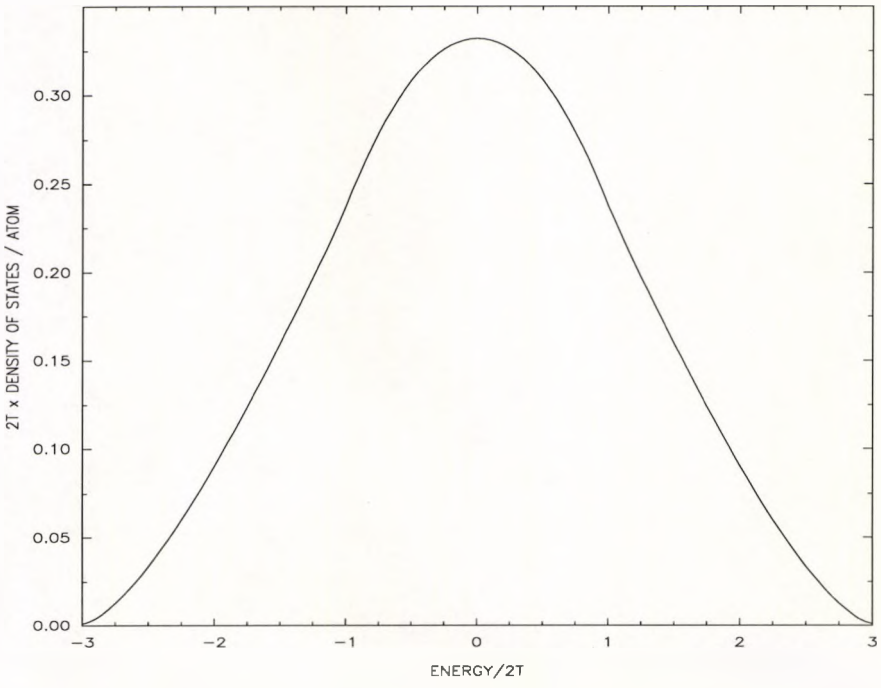

Figure 2.8: Density of states of the surface atomic plane of a semi-infinite crystal. $k_{||}$ summation is calculated using Cunningham's method. Here NC=32.

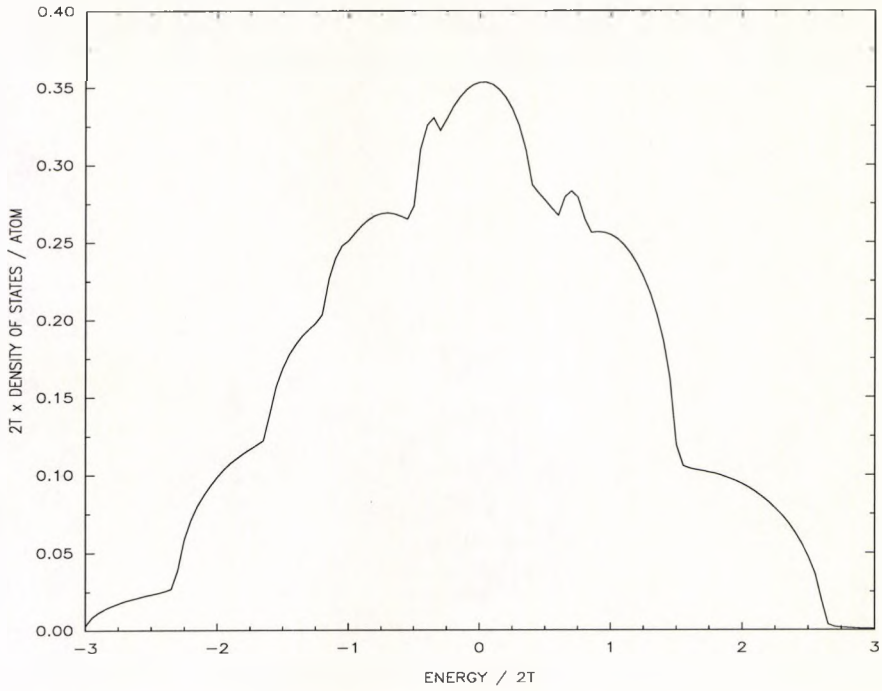

Figure 2.9: Density of states of the surface atomic plane of a semi-infinite crystal which is calculated using the direct summation method. Here N=5.

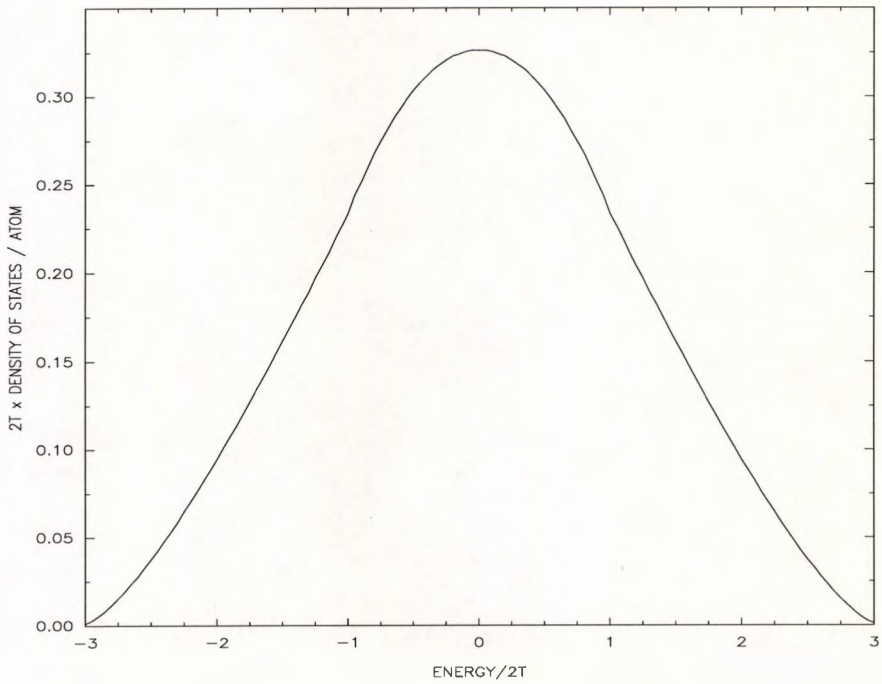

Figure 2.10: Density of states of the surface atomic plane of a semi-infinite crystal which is calculated using the direct summation method. Here N=50.

2.3 Analytic computation of the exchange coupling J(N)

Computing the thermodynamic potential Ω^s and therefore the exchange coupling using the numerical techniques described in Section 2.2 has proved very time consuming. So much so that this method of computing Ω^s is not viable as a practical solution for situations other than the most simple ones. The problem becomes even more acute as we generalize the models to include more than one band of electrons. The reason for this is the summation over $k_{||}$ and the energy integration require a large number of points to achieve accurate results.

In this section we formulate an alternative approach based on the idea outlined in Refs [33], [34] and [42] to compute the thermodynamic potential. The prohibitive $k_{||}$ summation and complex energy integration are replaced by their respective analytic solutions which is made possible using some approximations. This is called the Stationary Phase Approximation, denoted by SPA. The end result being that we can now evaluate Ω^s in a reasonable time. We recall again from Equation 1.33 that the exchange coupling is given by

$$J(N) = \frac{\left[(\Omega^{\uparrow}(N) + \Omega^{\downarrow}(N))_{FM} - (\Omega^{\uparrow}(N) + \Omega^{\downarrow}(N))_{AF}\right]}{A}, \tag{2.35}$$

where FM and AF denotes the ferromagnetic and antiferromagnetic configurations of the trilayer respectively and A is the cross-sectional area. For the same reason as in the numerical computation of the exchange coupling we concentrate on how to compute the thermodynamic potential itself here. The thermodynamic potential at

finite temperature is

$$\Omega^s(N) = -k_B T \int_{-\infty}^{\infty} \ln\left[1 + \exp\left(\frac{\mu - E}{k_B T}\right)\right] D^s(E, N) dE, \tag{2.36}$$

where N is the spacer thickness, T the temperature, μ the chemical potential, k_B is the Boltzmann constant,

$$D^s(E, N) = \sum_{k_\parallel} G^s(E, k_\parallel, N)$$

and finally

$$G^s(E, k_\parallel, N) = -\frac{1}{\pi} \sum_{i=1}^{N} Im G_{ii}^{i,s}(E, k_\parallel, N).$$

Equation 2.36 is the formula for Ω^s now generalized to include temperature as one of its parameters. It is clear that if we let $T \rightarrow 0$ then Equation 2.36 will tend towards the formula for Ω^s we used in Section 2.2 when we considered the case of T=0. This formula is given by Equation 2.23. During the derivation of the SPA we consider a general finite T. Once the derivation has been completed we let $T \rightarrow 0$, which will enable us to compare the results from the SPA with the numerical approach.

From a purely mathematical viewpoint it is obvious by looking at the formula for the thermodynamic potential that the oscillations in the exchange coupling must originate from $D^s(E, N)$. If we can show that the discrete variable N can be replaced by a continous one, say x and the function $\frac{1}{N} G^s(E, k_\parallel, N)$ (which we call the spectral density) is a periodic function of N then we can expand $G^s(E, k_\parallel, N)$ in terms of a Fourier series. We show these two criteria are fulfilled by obtaining an analytic solution for the Green's functions of the spacer layer consisting of N atomic planes

embedded between two semi-infinite crystals. This analytic solution for the single tight-binding band is given in Section 2.4.

It is found from this solution that the spectral density is a periodic function in N, which is now regarded as a continuous variable and its corresponding Fourier series is

$$\frac{1}{N}G^s(E,k_{||},N) = Re\sum_{n=1}^{\infty} C_n^s\left(E,k_{||}\right)\exp\left(2iNan\beta(E,k_{||})\right). \tag{2.37}$$

Here $ReC_n^s\left(E,k_{||}\right)$ is the usual Fourier coefficient a_n, $ImC_n^s\left(E,k_{||}\right)$ is the usual Fourier coefficient $-b_n$ and $\beta(E,k_{||})$ is some as yet unknown function which depends on E and $k_{||}$ and is related to the period of oscillations by $\frac{\pi}{\beta(E,k_{||})}$. In fact we will show in Section 2.4 that β is the wave vector for the bulk spacer layer, which is perpendicular to the layers. Replacing $G^s(E,k_{||},N)$ in Equation 2.36 by its Fourier series expansion given by Equation 2.37 we obtain

$$\begin{aligned}\Omega^s(N) = \; & -\frac{k_BTNA}{4\pi^2}Re\sum_{n=1}^{\infty}\int_{-\infty}^{\infty}\int_{-\infty}^{\infty}\int_{-\infty}^{\infty}\ln\left[1+\exp\left(\frac{\mu-E}{k_BT}\right)\right]\times \\ & C_n^s(E,k_{||})\exp\left(2iNan\beta(E,k_{||})\right)dk_xdk_ydE,\end{aligned} \tag{2.38}$$

where the summation over $k_{||}$ has been converted into two integrals, one with respect to k_x and the other k_y.

2.3.1 k_x and k_y integrals

In the numerical computation of Ω^s we performed the summation over $k_{||}$ using the time consuming Cunningham points. Here in the SPA we have replaced the summation by k_x and k_y integrals which can calculated analytically, after making some approximations.

We begin by looking at the exponential factor $\exp\left(2iNan\beta(E,k_{||})\right)$ in the formula for the thermodynamic potential given by Equation 2.38. This exponential oscillates rapidly as a function of $k_{||}$ for large values of N ie for large spacer thicknesses. These rapid oscillations tend to cancel each other out when performing the integral. The dominant contribution to the integral therefore comes from any region where the exponential factor varies only slowly as a function of $k_{||}$. This occurs when k_x and k_y are in the region of a stationary point, denoted by $k_{||}^0 = (k_x^0, k_y^0)$. We therefore approximate $\beta(E,k_{||})$ by expanding $\beta(E,k_{||})$ in terms of a Taylor series about the stationary point $k_{||}^0$ up to second order. By making this approximation it is now possible to find the analytic solution for the two integrals. With the dominant contribution coming from around the stationary points we approximate the Fourier coefficients by taking their values at $k_{||}^0$.

The Taylor series expansion of $\beta(E,k_{||})$ up to second order about the stationary point $k_{||}^0$ is

$$\begin{aligned}\beta(E,k_{||}^0) &= \beta(E,k_{||}^0) + \left\{\frac{\partial\beta}{\partial k_x}(k_x-k_x^0) + \frac{\partial\beta}{\partial k_y}(k_y-k_y^0)\right\} + \\ &\quad \frac{1}{2}\left\{\frac{\partial^2\beta}{\partial k_x^2}(k_x-k_x^0)^2 + 2\frac{\partial^2\beta}{\partial k_x\partial k_y}(k_x-k_x^0)(k_y-k_y^0) + \frac{\partial^2\beta}{\partial k_y^2}(k_y-k_y^0)^2\right\}.\end{aligned}$$

After simplifying this becomes

$$\beta(E,k_{||}^0) = \beta(E,k_{||}^0) + \frac{1}{2}\left\{\frac{\partial^2\beta}{\partial k_x^2}(k_x-k_x^0)^2 + \frac{\partial^2\beta}{\partial k_y^2}(k_y-k_y^0)^2\right\}. \qquad (2.39)$$

The first simplification of $\dfrac{\partial\beta}{\partial k_x} = \dfrac{\partial\beta}{\partial k_y} = 0$ is an obvious one. In the simple cubic crystal lattice structure there is naturally no mixed derivative. When applying this Taylor series expansion to a material which has a different lattice structure, for

example, this may not be the case. However this second simplification can always be obtained by eliminating the mixed term. This is achieved by reducing the quadratic form to its corresponding diagonal form by rotating the (k_x, k_y) axes. So substituting the simplified Taylor series expansion into Equation 2.38 we obtain

$$\Omega^s = -\frac{k_B T N A}{4\pi^2} Re \sum_{n=1}^{\infty} \int_{-\infty}^{\infty} \ln\left[1 + \exp\left(\frac{\mu - E}{k_B T}\right)\right] C_n^s(E, k_{\|}^0) \exp(2iNan\beta)$$
$$\times \int_{-\infty}^{\infty}\int_{-\infty}^{\infty} \exp\left(iNan\left(\frac{\partial^2\beta}{\partial k_x^2}(k_x - k_x^0)^2 + \frac{\partial^2\beta}{\partial k_y^2}(k_y - k_y^0)^2\right)\right) dk_x dk_y dE. \tag{2.40}$$

Consider first the k_x integral only. By making the substitution $Z = (k_x - k_x^0)$ we find that

$$\int_{-\infty}^{\infty} \exp\left(iNan\frac{\partial^2\beta}{\partial k_x^2}(k_x - k_x^0)^2\right) dk_x = \int_{-\infty}^{\infty} \exp\left(iNan\frac{\partial^2\beta}{\partial k_x^2}Z^2\right) dZ. \tag{2.41}$$

If the factor $\frac{\partial^2\beta}{\partial k_x^2} > 0$ then we let $Z = y\exp\left(\frac{i\pi}{4}\right)$. This substitution for Z in the k_x integral leads to the integral being put in a form of the standard Gaussian integral and gives us the answer to be

$$\int_{-\infty}^{\infty} \exp\left(iNan\frac{\partial^2\beta}{\partial k_x^2}(k_x - k_x^0)^2\right) dk_x = \exp\left(\frac{i\pi}{4}\right)\sqrt{\frac{\pi}{Nan\frac{\partial^2\beta}{\partial k_x^2}}}. \tag{2.42}$$

If on the other hand $\frac{\partial^2\beta}{\partial k_x^2} < 0$ then we let $Z = y\exp\left(-\frac{i\pi}{4}\right)$. This leads to the following solution:

$$\int_{-\infty}^{\infty} \exp\left(iNan\frac{\partial^2\beta}{\partial k_x^2}(k_x - k_x^0)^2\right) dk_x = \exp\left(-\frac{i\pi}{4}\right)\sqrt{\frac{\pi}{Nan\frac{\partial^2\beta}{\partial k_x^2}}}. \tag{2.43}$$

It can be seen that this method of evaluating the k_x integral can also be applied to k_y integral in exactly the same way. Once these two integrals have been performed

we are left with the following formula for Ω^s

$$\begin{aligned}\Omega^s &= -\frac{k_B T A}{4\pi a} Re \sum_{n=1}^{\infty} \frac{\sigma}{n} \int_{\infty}^{\infty} ln\left[1+\exp\left(\frac{\mu-E}{k_B T}\right)\right] C_n^s(E,k_{\|}^0)\times \\ &\exp\left(2iNan\beta(E,k_{\|}^0)\right)\left|\frac{\partial^2\beta}{\partial k_x^2}\frac{\partial^2\beta}{\partial k_y^2}\right|^{-1/2} dE,\end{aligned} \tag{2.44}$$

where

$$\sigma = \begin{cases} e^{i\pi/2} & \text{if } \dfrac{\partial^2\beta}{\partial k_x^2} \text{ and } \dfrac{\partial^2\beta}{\partial k_y^2} > 0 \\ e^{-i\pi/2} & \text{if } \dfrac{\partial^2\beta}{\partial k_x^2} \text{ and } \dfrac{\partial^2\beta}{\partial k_y^2} < 0 \\ 1 & \text{if } \dfrac{\partial^2\beta}{\partial k_x^2} > 0 \text{ and } \dfrac{\partial^2\beta}{\partial k_y^2} < 0 \text{ or vice versa.} \end{cases}$$

2.3.2 Energy integration

The next step is to compute the energy integral. We start the process by noting that the factors $C_n^s(E,k_{\|}^0)$, $\frac{\partial^2\beta}{\partial k_x^2}$ and $\frac{\partial^2\beta}{\partial k_y^2}$ only depend on E weakly. Taking account of this the energy integral for Ω^s is simplified to

$$\begin{aligned}\Omega^s &= -\frac{k_B T A}{4\pi a} Re \sum_{n=1}^{\infty} \left(\frac{\sigma}{n}\right) C_n^s(E,k_{\|}^0)\left|\frac{\partial^2\beta}{\partial k_x^2}\frac{\partial^2\beta}{\partial k_y^2}\right|^{-1/2} \times \\ &\int_{\infty}^{\infty} \ln\left[1+\exp\left(\frac{\mu-E}{k_B T}\right)\right]\exp\left(2iNan\beta(E,k_{\|}^0)\right) dE,\end{aligned} \tag{2.45}$$

which enables us to evalaute the energy integral by parts by letting

$$U = ln\left[1+\exp\left(\frac{\mu-E}{k_B T}\right)\right]$$

and

$$\begin{aligned}\frac{\partial V}{\partial E} &= \exp\left(2iNan\beta(E,k_{\|}^0)\right) \\ \Rightarrow \quad V &= \int \exp\left(2iNan\beta(E,k_{\|}^0)\right)\left(\frac{\partial E}{\partial \beta}\right)\left(\frac{\partial \beta}{\partial E}\right) dE \\ V &= \frac{\partial E}{\partial \beta}\left\{\frac{\exp\left(2iNan\beta(E,k_{\|}^0)\right)}{2iNan}\right\}.\end{aligned}$$

We note that $\frac{\partial E}{\partial \beta}$ also only weakly depends on E. After integrating Equation 2.45 by parts once we obtain

$$\begin{aligned}\Omega^s = & -\frac{A}{8\pi a^2 N} Re \sum_{n=1}^{\infty} \left(\frac{\sigma}{in^2}\right) C_n^s(E, k_{||}^0) \frac{\partial E}{\partial \beta} \left|\frac{\partial^2 \beta}{\partial k_x^2} \frac{\partial^2 \beta}{\partial k_y^2}\right|^{-1/2} \\ & \times \int_{-\infty}^{\infty} \frac{\exp\left(2iNan\beta(E, k_{||}^0)\right)}{\left(1 + \exp\left(\frac{\mu - E}{k_B T}\right)\right)} dE.\end{aligned} \tag{2.46}$$

To complete the energy integration in Equation 2.46 we look at the exponential factor $\exp\left(2iNan\beta(E, k_{||}^0)\right)$. Much the same as before when we were evaluating the k_x and k_y integrals we see that this function oscillates rapidly this time as a function of E for large values of N or large spacer thicknesses. Similar to the k_x and k_y integrals these rapid oscillations lead to a lot of cancellations when performing the energy integral. However the dominant contribution to the integral here comes from around the Fermi level because we have the discrete finite upper limit in the energy integral. The dominant contribution comes from the beginning of the last oscillation up to the Fermi level. We therefore approximate the integral by expanding $\beta(E, k_{||}^0)$ using the Taylor series about the point μ. This time we take the Taylor series up to the first order. Because the dominant contribution comes from around the Fermi energy level we approximate the Fourier coefficients and all the factors that only weakly depend on E by taking their values at μ. The Taylor series expansion of $\beta(E, k_{||}^0)$ about μ is

$$\beta(E, k_{||}^0) = \beta(\mu, k_{||}^0) + \frac{\partial \beta}{\partial E}(E - \mu).$$

Putting this Taylor series expansion for $\beta(E, k_{||}^0)$ given just above into Equation 2.46

we obtain

$$\begin{aligned}\Omega^s = & -\frac{A}{8\pi a^2 N} Re \sum_{n=1}^{\infty} \frac{\sigma}{in^2} \frac{\partial E}{\partial \beta} \left| \frac{\partial^2 \beta}{\partial k_x^2} \frac{\partial^2 \beta}{\partial k_y^2} \right|^{-1/2} \exp\left(2iNan\beta(\mu, k_{\|}^0)\right) \\ & \times C_n^s(\mu, k_{\|}^0) \int_{-\infty}^{\infty} \frac{\exp\left(2iNan\frac{\partial \beta}{\partial E}(E-\mu)\right)}{1+\exp\left(\frac{\mu - E}{k_B T}\right)} dE.\end{aligned} \tag{2.47}$$

Making the substitution $Z = (\mu - E)$ in the energy integral of Equation 2.47 leads to the integral being put in the form of another standard integral

$$\int_{-\infty}^{\infty} \frac{\exp\left(2iNan\frac{\partial \beta}{\partial E}(E-\mu)\right)}{1+\exp\left(\frac{\mu - E}{k_B T}\right)} dE = -\int_{-\infty}^{\infty} \frac{\exp\left(-2iNan\frac{\partial \beta}{\partial E} Z\right)}{1+\exp\left(\frac{Z}{k_B T}\right)} dZ,$$

which gives us the following solution

$$= -k_B T \left\{ \frac{-i\pi}{\sinh\left(-2Nank_B T\pi \frac{\partial \beta}{\partial E}\right)} \right\}.$$

Replacing the energy integral by its solution in Equation 2.47 we obtain

$$\Omega^s = -\frac{Ak_B T}{8a^2 N} Re \sum_{n=1}^{\infty} \frac{\sigma}{n^2} \frac{\partial E}{\partial \beta} \left| \frac{\partial^2 \beta}{\partial k_x^2} \frac{\partial^2 \beta}{\partial k_y^2} \right|^{-1/2} \frac{C_n^s(\mu, k_{\|}^0) \exp\left(2iNan\beta(\mu, k_{\|}^0)\right)}{\sinh\left(-2Nank_B T\pi \frac{\partial \beta}{\partial E}\right)}. \tag{2.48}$$

All that remains for us to do, to be able to compare results from the SPA with the numerical approach is to let $T \to 0$. Letting $T \to 0$ we see that

$$\sinh\left(-2Nank_B T\pi \frac{\partial \beta}{\partial E}\right) \to -2Nank_B T\pi \frac{\partial \beta}{\partial E}$$

and $\mu \to E_f$. Therefore the formula for Ω^s becomes

$$\begin{aligned}\Omega^s = & \frac{A}{16a^3 N^2 \pi} Re \sum_{n=1}^{\infty} \frac{\sigma}{n^3} \left(\frac{\partial E}{\partial \beta}\right)^2 C_n^s(E_f, k_{\|}^0) \left| \frac{\partial^2 \beta}{\partial k_x^2} \frac{\partial^2 \beta}{\partial k_y^2} \right|^{-1/2} \\ & \times \exp\left(2iNan\beta(E_f, k_{\|}^0)\right).\end{aligned} \tag{2.49}$$

We are now able to calculate $J(N)$ using Equation 2.49. This formula is as equally valid for one band as it is for two or more provided that we can show that the spectral density $\frac{1}{N}G^s(E_f, k_{\|}, N)$ is a periodic function of "continuous" N and it is periodic with a single period only.

2.3.3 Application of the SPA to a single orbital trilayer

Now the formula for the thermodynamic potential Ω^s has been derived using the SPA the next step is to apply this formula to a general single orbital trilayer. Once this task has been completed we will then be able to compare the results of computing the exchange coupling numerically with those using the SPA.

In order to apply Equation 2.49 to a single orbital trilayer we first need to find an explicit expression for β. To do this we use the analytic formula for the average spectral density, which is derived in Section 2.4. The end result in Equation 2.85 shows that the period of oscillations is given analytically by π/θ for any given value of E and $k_{||}$. Here θ is the perpendicular wavevector $k_z(E, k_{||})$ of the bulk tight-binding energy band of the spacer metal and therefore $\beta = \theta$. Replacing $k_z(E, k_{||})$ by $\beta(E, k_{||})$ in the bulk tight-binding energy band for the spacer metal we obtain

$$E = E_{sp} - 2T_{sp}\left(\cos(ak_x) + \cos(ak_y) + \cos\left(a\beta(E, k_{||})\right)\right), \tag{2.50}$$

where E_{sp} is the atomic potential of the spacer layer, T_{sp} is the hopping integral of the spacer layer and a is the inter-atomic distance. We can now obtain all the factors in Equation 2.49, except the Fourier coefficients using Equation 2.50. The first task that needs to be completed before we can proceed with the application of the SPA is to find all the possible stationary points $k_{||}^0$. These are found by finding the values of $k_{||}$ where $\dfrac{\partial\beta}{\partial k_x} = \dfrac{\partial\beta}{\partial k_y} = 0$. Differentiating Equation 2.50 once with respect to k_x we obtain

$$\frac{\partial E}{\partial k_x} = 2T_{sp}a\sin(ak_x) + 2T_{sp}a\sin\left(a\beta(E, k_{||})\right)\frac{\partial\beta}{\partial k_x}, \tag{2.51}$$

therefore the stationary point occurs when

$$\sin(ak_x) = 0, \tag{2.52}$$

as $\dfrac{\partial E}{\partial k_x}$ is equal to zero. Similarly differentiating Equation 2.50 with respect to k_y this time, we obtain

$$\frac{\partial E}{\partial k_y} = 2T_{sp}a\sin(ak_y) + 2T_{sp}a\sin\left(a\beta(E,k_{||})\right)\frac{\partial \beta}{\partial k_y}, \tag{2.53}$$

therefore the stationary point occurs when

$$\sin(ak_y) = 0, \tag{2.54}$$

as $\dfrac{\partial E}{\partial k_y}$ is equal to zero. Equations 2.52 and 2.54 gives all the possible stationary points to be

$$(k_x^0, k_y^0) = (0,0), (0, \pm\frac{\pi}{a}), (\pm\frac{\pi}{a}, 0) \ \textit{and} \ (\pm\frac{\pi}{a}, \pm\frac{\pi}{a}). \tag{2.55}$$

Next we find $\beta(E_f, k_{||}^0)$. $\beta(E_f, k_{||}^0)$ is simply found by setting $E = E_f$ and $k_{||} = k_{||}^0$ in Equation 2.50 and rearranging to find that

$$\beta(E_f, k_{||}^0) = \frac{1}{a}\arccos\left(\frac{E_{sp} - E_f - 2T_{sp}(\cos(ak_x^0) + \cos(ak_y^0))}{2T_{sp}}\right). \tag{2.56}$$

Now we obtain $\dfrac{\partial E}{\partial \beta}$. This is found by differentiating Equation 2.50 once with respect to β and this gives us

$$\frac{\partial E}{\partial \beta} = 2T_{sp}a\sin\left(a\beta(E,k_{||})\right). \tag{2.57}$$

Now we find $\dfrac{\partial^2 \beta}{\partial k_x^2}$. Using the right hand side of Equation 2.53 and by noting that this is equal to zero we obtain

$$\sin\left(a\beta(E,k_{||})\right)\frac{\partial \beta}{\partial k_x} = -\sin(ak_x).$$

Differentiating this again with respect to k_x yields

$$a\cos\left(a\beta(E,k_{||})\right)\left(\frac{\partial\beta}{\partial k_x}\right)^2+\sin\left(a\beta(E,k_{||})\right)\frac{\partial^2\beta}{\partial k_x^2}=-a\cos(ak_x),$$

which simplifies to

$$\frac{\partial^2\beta}{\partial k_x^2}=-\frac{a\cos(ak_x)}{\sin\left(a\beta(E,k_{||})\right)} \tag{2.58}$$

because $\frac{\partial\beta}{\partial k_x}=0$ at the stationary points. Applying a similar technique for $\frac{\partial^2\beta}{\partial k_y^2}$ we obtain

$$\frac{\partial^2\beta}{\partial k_y^2}=-\frac{a\cos(ak_y)}{\sin\left(a\beta(E,k_{||})\right)}. \tag{2.59}$$

By substituting the values of $E=E_f$ and $k_{||}=k_{||}^0$ into Equations 2.57, 2.58 and 2.59 we can find σ and by using Equation 2.49 we find that

$$\begin{aligned}\Omega^s(N) &= \frac{A}{16a^2N^2\pi}Re\sum_{n=1}^{\infty}\frac{\sigma}{n^3}4T_{sp}^2\sin^2\left(a\beta(E_f,k_{||}^0)\right)\sqrt{\left|\frac{\sin^2\left(a\beta(E_f,k_{||}^0)\right)}{\cos(k_x^0)\cos(k_y^0)}\right|}\times \\ &\quad C_n^s(E_f,k_{||}^0)\exp\left(2iNan\beta(E_f,k_{||}^0)\right).\end{aligned} \tag{2.60}$$

As can be seen from Equation 2.60 all that remains for us to do to complete the application of the SPA is to compute the Fourier coefficients $C_n^s(E_f,k_{||}^0)$. We recall from Section 2.3 that $C_n^s(E_f,k_{||}^0)$ are the corresponding Fourier coefficients of the periodic spectral density $\frac{1}{N}G^s(E,k_{||},N)$. The Fourier coefficients could be obtained directly from the analytic Green's function of the trilayer, which is outlined in Section 2.4. However we use another equally valid method for computing the Fourier coefficients that does not require the analytic Green's function. The advantage of this method being we can always compute the Fourier coefficients even when we do not have an analytic solution for the Green's function of a trilayer. In the next

Chapter when we consider a two orbital trilayer we do not yet have an analytic solution for the Green's functions. This approach therefore enables us to compute the Fourier coefficients for the two orbital trilayer as well as the one band trilayer provided the spectral density is periodic with one period only.

We start by obtaining a sample data set of the spectral density for which we we usually take the spacer layer to be between 500 and 600 atomic planes. The spacer layer is chosen thus because the spectral density behaves asymptotically like a periodic function for larger spacer thicknesses. This is due to the effects of the left and right semi-infinite crystals, which is demonstrated in Equation 2.85. Using the periodicity of the spectral density we shift the sample data set so that all the values of the spacer layer lie between the two points $-\frac{p}{2}$ and $\frac{p}{2}$ where p is the period of the spectral density. Once this has been completed the shifted data set is ordered so that all the values of the spacer thickness are in ascending order. We should then have a tightly bunched smooth data set which typically looks like Figure 2.11.

The Fourier coefficients are then computed from the shifted ordered sample data set using Simpson's rule of integration for irregularly spaced data. From Figure 2.11 we see that the points are relatively evenly spread out between the two limits of $-\frac{p}{2}$ and $\frac{p}{2}$. Problems occur with this method of computing the Fourier coefficients when the shifted data set becomes bunched. This occurs when the period of the spectral density is or is close to being commensurate with the crystal lattice. An example of this is shown in Figure 2.12.

When the period of the spectral density is close to being commensurate the

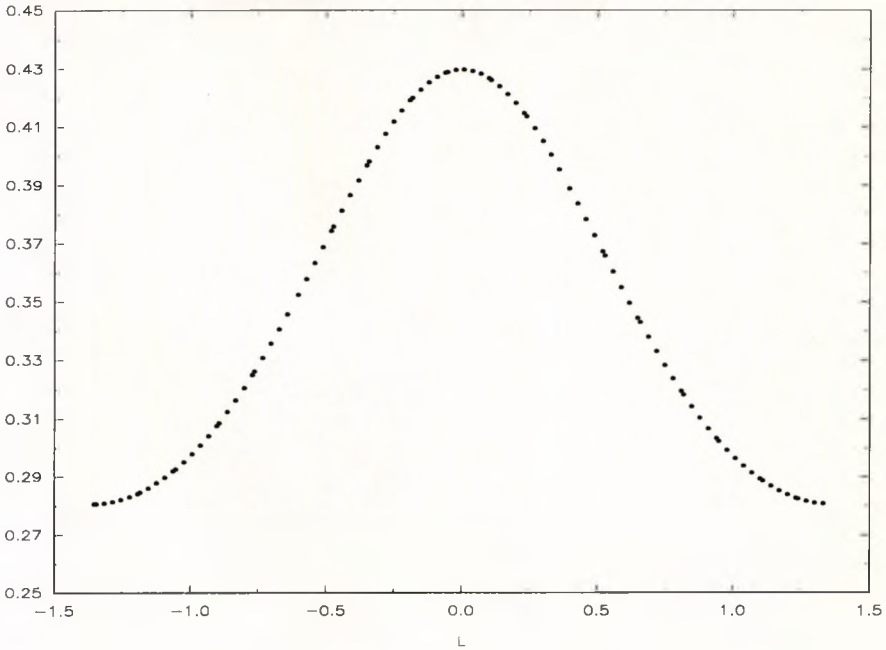

Figure 2.11: Example of the spectral density shifted so that all values of the spacer thickness now lie in the region $\left(-\frac{p}{2}, \frac{p}{2}\right)$ where p is the period of the spectral density. Here p $\simeq 2.71$ atomic planes. It is evaluated at $E = E_f$ and at the point $k_x = k_y = 0$.

bunching of the data can be overcome by simply increasing the number of points in our sample set until the shifted spectral density becomes more evenly spaced. If the period is commensurate then increasing the size of the sample data set does not help overcome the problem of bunching. We know that as long as the period of the spectral density is close to but not actually commensurate then the problem of bunching can always be overcome by simply increasing the size of the data set. So if a parameter or parameters are chosen so that the period of the spectral density is infinitessimally close to being commensurate then we will be able to obtain a good approximation for the exchange coupling when the period is commensurate with the

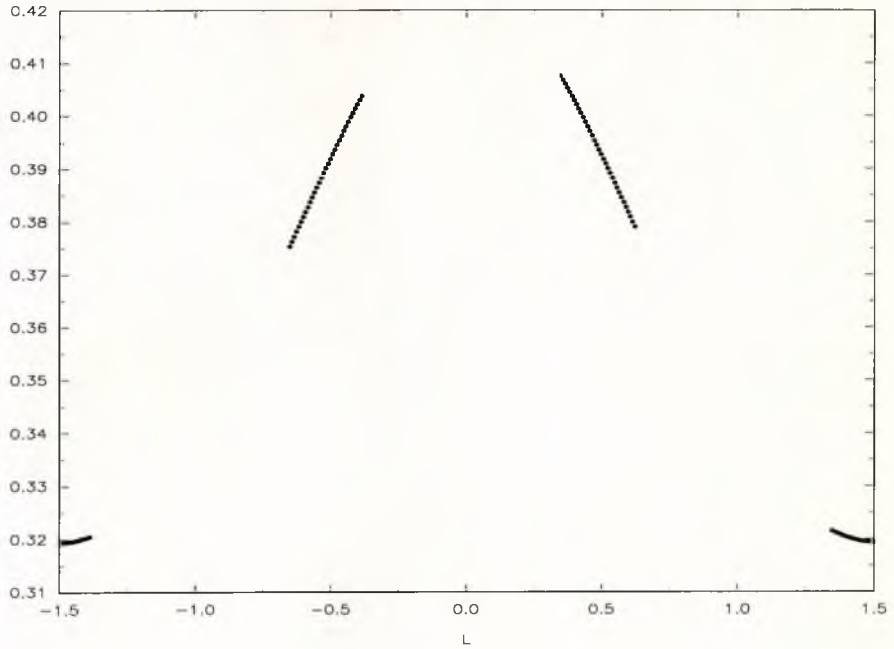

Figure 2.12: Example of the shifted spectral density when the period p is close to being commensurate. Here p $\simeq$ 3.01 atomic planes. It is evaluated at $E = E_f$ and at $k_x = k_y = 0$.

crystal lattice.

One final thing to note about the shifting of the spectral density concerns the period used. There are in fact two possible periods which can be employed to shift the sample data set. In Section 2.4 we show that the spacer thickness N may be mathematically viewed as a continous variable. This property is essential if we wish to Fourier analyse the spectral density. Physically the spacer thickness can only take integer values and we can only take a "sample" of the spectral density at integer values using the numerical techniques such as adlayering. It is this discrete sampling which is responsible for a second possible period of oscillations. This

effect has already been observed in the RKKY theory and is known as aliasing see Refs [31] and [32]. The two possible periods for the period of oscillations of the spectral density are either $p = \frac{\pi}{\beta(E, k_{||})}$ or $p = \frac{\pi}{\pi - \beta(E, k_{||})}$. It is easy to see which of the two periods is appropriate by simply inspecting a plot of the spectral density.

2.4 Analytic solution for the Green's functions of a trilayer

The aim of this section is to show that it is mathematically acceptable to Fourier analyse the spectral density $\frac{1}{N}G^s(E, k_{||}, N)$ and thus use the SPA. In Section 2.1 we obtained the exact Green's function of an arbitrary atomic plane in the spacer layer using numerical techniques such as adlayering. Whilst this approach gives the exact Green's functions we seek it is not sufficient to show that the spectral density can be Fourier analysed. To show this we need to find an analytic solution for the Green's functions of a trilayer, which we do here.

Our analytic solution is obtained by taking three steps. We first obtain the analytic Green's functions of a finite slab. The finite slab is deposited onto a semi-infinite crystal and once deposited we call this layer an overlayer. Finally another semi-infinite crystal is deposited on top of the overlayer to create the trilayer.

2.4.1 Analytic solution for the Green's function of a finite slab

For a finite slab we have the situation as shown in Figure 2.13. The corresponding Green's functions of the finite slab with a single band of electrons are given by

$$\sum_j (EI - H)_{i,j} G_{j,k} = \delta_{i,k} \tag{2.61}$$

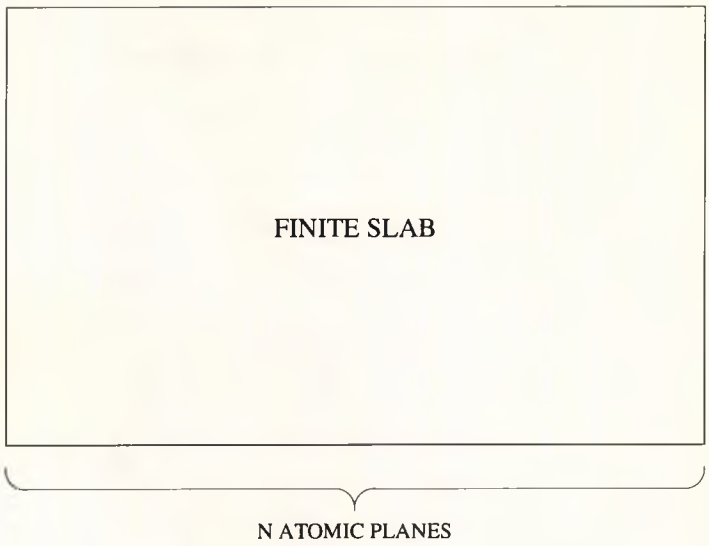

Figure 2.13: Diagram of a finite slab consisting of N atomic planes.

and expressed explicity in matrix form it is

$$\begin{pmatrix} (E-W) & T & 0 & 0 & \dots \\ T & (E-W) & T & 0 & \dots \\ 0 & T & (E-W) & T & \dots \\ & \vdots & \vdots & & \\ & \vdots & \vdots & & \end{pmatrix} \begin{pmatrix} G_{11} & \dots & \dots & \dots & G_{1N} \\ \vdots & & & & \vdots \\ \vdots & & & & \vdots \\ \vdots & & & & \vdots \\ G_{N1} & \dots & \dots & \dots & G_{NN} \end{pmatrix} = I_{NN}, \tag{2.62}$$

where all three matrices have dimension $N \times N$ because we are considering the case of a slab with N atomic planes. $(EI - H)_{i,j}$ is given by the matrix on the far left of Equation 2.62. T is the hopping integral and $W = E_s + 2T(\cos(ak_x) + \sin(ak_y))$, where E_s is the atomic potential of all the atomic planes in the slab. a is the inter-atomic distance. The middle matrix describes the matrix elements of the Green's function. Finally I_{NN} is the identity matrix.

The k^{th} column in the identity matrix is obtained by multiplying the matrix $(EI - H)_{i,j}$ by the k^{th} column of the Green's function matrix. In matrix form it is

$$\begin{pmatrix} (E-W) & T & 0 & 0 & \dots \\ T & (E-W) & T & 0 & \dots \\ 0 & T & (E-W) & T & \dots \\ & \vdots & \vdots & & \\ & \vdots & \vdots & & \\ & \vdots & \vdots & & \\ & \vdots & \vdots & & \end{pmatrix} \begin{pmatrix} G_{1k} \\ \vdots \\ \vdots \\ \vdots \\ \vdots \\ \vdots \\ \vdots \\ G_{Nk} \end{pmatrix} = \begin{pmatrix} 0 \\ \vdots \\ 0 \\ 1 \\ 0 \\ \vdots \\ 0 \end{pmatrix}.$$

The 1 in the column matrix on the right hand side of the equals sign appears in k^{th} row. From this matrix equation we obtain an inhomogeneous difference equation for the Green's functions of the finite slab which is

$$TG(n-1,k)+(E-W)G(n,k)+TG(n+1,k) = \begin{cases} 0 & 0 \leq n < k, k < n \leq N+1 \\ 1 & n = k \end{cases}$$

thus yielding the following general characteristic equation

$$TG(n-1,k) + (E-W)G(n,k) + TG(n+1,k) = 0. \tag{2.63}$$

The solution of the characteristic equation reduces to a simple quadratic in X by substituting X^n for $G(n,k)$ in Equation 2.63. The corresponding quadratic is

$$TX^2 + (E-W)X + T = 0, \tag{2.64}$$

which gives

$$X = -\cos(\theta) \pm i\sin(\theta) = -\exp(\mp i\theta)$$

for the solution of X where

$$\cos(\theta) = \frac{E - W}{2T}$$

and

$$\sin(\theta) = \frac{\sqrt{(E - W)^2 - 4T^2}}{2T}.$$

The general solution for $G(n, k)$ is therefore

$$G(n, k) = A(-1)^n \exp(in\theta) + B(-1)^n \exp(-in\theta). \tag{2.65}$$

All that remains, to complete the solution of the Green's function $G(n, k)$, is to obtain the coefficients A and B. However there is an insufficient number of boundary conditions in the inhomogeneous system to find A and B. In order to do this we need to look at the slab in a slightly different way to the idea of a single finite slab of N atomic planes. Rather we need to view the slab as two isolated finite slabs that meet at the k th atomic plane as shown in Figure 2.14. Both the left and right isolated slabs are finite so they satisfy the same characteristic equation and their respective Green's functions therefore satisfy the same general form as in Equation 2.65. So we now have

$$\begin{aligned} G^L(n, k) &= A^L(-1)^n \exp(in\theta) + B^L(-1)^n \exp(-in\theta) \quad n \leq k \\ \text{and} \qquad & \qquad (2.66) \\ G^R(n, k) &= A^R(-1)^n \exp(in\theta) + B^R(-1)^n \exp(-in\theta) \quad n \geq k, \end{aligned}$$

where G^L denotes the Green's functions of the left isolated slab and G^R denotes the Green's functions of the right isolated slab. The boundary conditions for the left

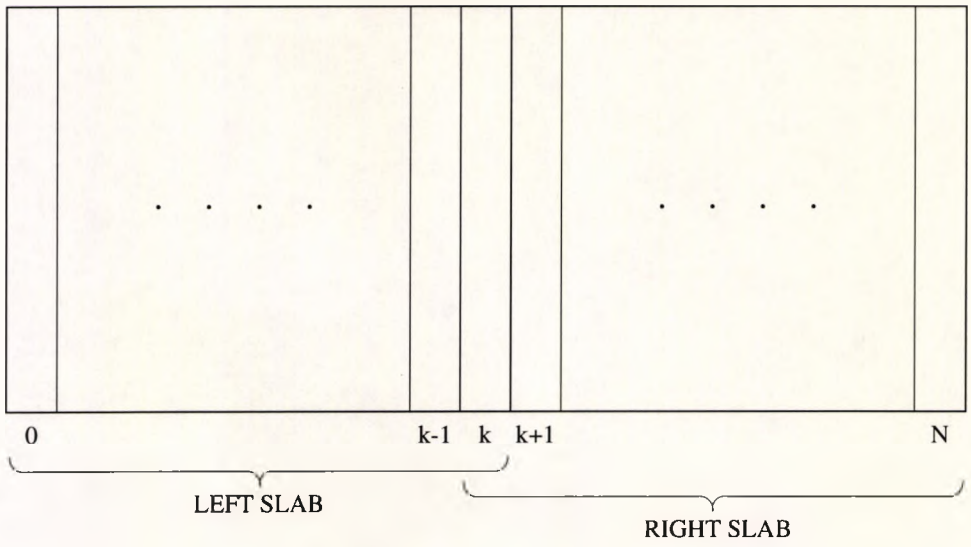

Figure 2.14: Diagram showing two finite slabs that meet at the k th atomic plane. The left slab contains k atomic planes and the right slab contains N-k atomic planes.

and right slabs are:-

$$\text{(a)} \qquad G^L(0,k) = 0$$

$$\text{(b)} \qquad G^R(N+1,k) = 0$$

$$\text{(c)} \qquad G^L(k,k) = G^R(k,k)$$

$$\text{(d)} \qquad 1 = TG^L(k-1,k) + (E-W)G^L(k,k) + TG^R(k+1,k).$$

Boundary condition (c) occurs because the two slabs meet at the k th atomic plane and at this plane G^R and G^L must be equal to one another. Boundary condition (d) arises when we set n=k in the general difference equation that forms the solution for the Green's functions. Using boundary condition (c) we could have $G^L(k,k)$ or $G^R(k,k)$ in boundary condition (d) because $G^L(k,k) = G^R(k,k)$.

Applying boundary condition (a)

$$\begin{aligned} G^L(0,k) &= A^L + B^L = 0 \\ \Rightarrow G^L(n,k) &= 2iA^L(-1)^n \sin(n\theta). \end{aligned}$$

Applying boundary condition (b)

$$\begin{aligned} G^R(N+1,k) &= A^R \exp(i(N+1)\theta) + B^R \exp(-i(N+1)\theta) = 0 \\ \Rightarrow G^R(n,k) &= 2iA^R(-1)^n \exp(i(N+1)\theta) \sin((n-N-1)\theta). \end{aligned}$$

Applying boundary condition (c)

$$\begin{aligned} G^L(k,k) &= G^R(k,k) \\ 2iA^L(-1)^k \sin(k\theta) &= 2iA^R(-1)^k \exp(i(N+1)\theta) \sin((k-N-1)\theta) \\ \Rightarrow A^L &= A^R \frac{\exp(i(N+1)\theta) \sin((k-N-1)\theta)}{\sin(k\theta)} \end{aligned}$$

which gives

$$\begin{aligned} G^L(n,k) &= \frac{2iA^R(-1)^n \exp(i(N+1)\theta) \sin((k-N-1)\theta) \sin(n\theta)}{\sin(k\theta)} \\ G^R(n,k) &= 2iA^R(-1)^n \exp(i(N+1)\theta) \sin((n-N-1)\theta) \end{aligned}$$

Applying boundary condition (d)

$$\begin{aligned} 1 &= TG^L(k-1,k) + (E-W)G^L(k,k) + TG^R(k+1,k) \\ \Rightarrow A^R &= \frac{\sin(k\theta)}{2i(-1)^{k-1} \exp(i(N+1)\theta) T \sin((N+1)\theta) \sin(\theta)} \end{aligned}$$

This finally gives us

$$\begin{aligned} G^L(n,k) &= \frac{(-1)^{n-k+1} \sin(n\theta) \sin((k-N-1)\theta)}{T \sin((N+1)\theta) \sin(\theta)} \quad n \le k \\ \text{and} \\ G^R(n,k) &= \frac{(-1)^{n-k+1} \sin(k\theta) \sin((n-N-1)\theta)}{T \sin((N+1)\theta) \sin(\theta)} \quad n \ge k. \end{aligned} \tag{2.67}$$

Now we have an analytic expression for all the matrix elements of the Green's function of the finite slab we can proceed with the next task. Depositing the slab onto a semi-infinite crystal.

2.4.2 Analytic solution for the Green's function of an overlayer

The next step in obtaining the analytic solution for the Green's function of a trilayer is to deposit the finite slab onto a semi-infinite crystal. In Section 2.1.1 we deposit adlayers onto the substrate one by one as as the second step in finding the Green's function of an arbitrary atomic plane in the spacer layer. Depositing a finite slab onto the semi-infinite crystal is a similar process to the adlayering algorithm. The difference between the two is when we deposit an overlayer all the atomic planes are deposited in one go and not one by one as in the adlayering procedure. The end result will be the same. For the overlayer we have the situation as described in Figure 2.15.

As in previous sections the cleavage plane is the mathematical device used to disconnect the overlayer from the semi-infinite crystal. Once disconnected electrons are not able to hop across the cleavage plane. The overlayer is then reconnected to the semi-infinite crystal using Dyson's Equation which is

$$G^{ov}(i,j) = G^{cl}(i,j) + \sum_{p,q} G^{cl}(i,p)W(p,q)G^{ov}(q,j), \tag{2.68}$$

where G^{cl} are the Green's functions of the system with the cleavage plane and G^{ov}

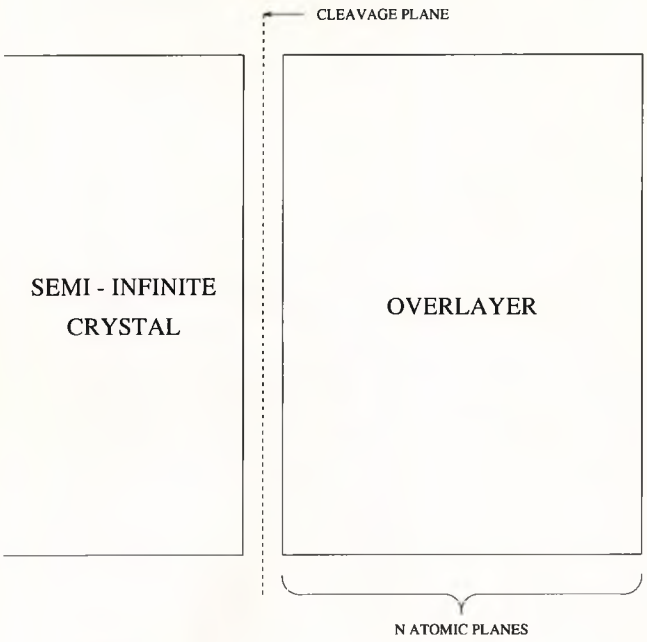

Figure 2.15: Diagram of an overlayer consisting of N atomic planes deposited onto a semi-infinite crystal.

are the Green's functions of the system without the cleavage plane. Here the only non-zero peturbation matrix elements $W(p,q)$ are:-

$$\begin{aligned} W(0,1) &= < k_{||}, 0 \mid H \mid k_{||}, 1 > = T \qquad \text{and} \\ W(1,0) &= < k_{||}, 1 \mid H \mid k_{||}, 0 > = T, \end{aligned} \tag{2.69}$$

where W(1,0) and W(0,1) is the hopping of electrons from the overlayer to the semi-infinite crystal and vice versa and T is the potential for an electron to hop from atom to atom. Substituting the results from Equation 2.69 into Dyson's Equation gives us

$$G^{ov}(i,j) = G^{cl}(i,j) + T(G^{cl}(i,1)G^{ov}(0,j) + G^{cl}(i,0)G^{ov}(1,j)).$$

Assuming that $i,j \epsilon 1,N$ we see that $G^{cl}(i,0) = 0$ because electrons cannot hop across

the cleavage plane. The formula for $G^{ov}(i,j)$ therefore simplifies to

$$G^{ov}(i,j) = G^{cl}(i,j) + TG^{cl}(i,1)G^{ov}(0,j). \tag{2.70}$$

The only term in Equation 2.70 we do not yet know is $G^{ov}(0,j)$. This is found by setting i=0 in Dyson's Equation Equation 2.68 taking account of the perturbation and again assuming that $i,j\epsilon 1,N$. The solution of $G^{ov}(0,j)$ is

$$G^{ov}(0,j) = TG^{cl}(0,0)G^{ov}(1,j). \tag{2.71}$$

Similarly $G^{ov}(1,j)$ is obtained by setting i=1 in Equation 2.68 which gives us

$$G^{ov}(1,j) = G^{cl}(1,j) + TG^{cl}(1,1)G^{ov}(0,j). \tag{2.72}$$

By using Equations 2.71 and 2.72 we find that

$$G^{ov}(0,j) = \frac{TG^{cl}(0,0)G^{cl}(1,j)}{1 - T^2G^{cl}(0,0)G^{cl}(1,1)}. \tag{2.73}$$

Substituting the answer for $G^{ov}(0,j)$ into Equation 2.70 and assuming that $i,j\epsilon 1,N$ we obtain

$$G^{ov}(i,j) = G^{cl}(i,j) + \frac{T^2G^{cl}(0,0)G^{cl}(i,1)G^{cl}(1,j)}{1 - T^2G^{cl}(0,0)G^{cl}(1,1)} \tag{2.74}$$

for the general formula for the Green's functions of an overlayer, where $G^{cl}(0,0)$ is the surface Green's function of the semi-infinite crystal. All the other G^{cl}'s are the Green's functions of the finite slab and their solutions are given by Equation 2.67.

It should be noted that Equation 2.74 is only valid for the Green's functions describing the atomic planes making up the overlayer. This is due to the assumption that $i,j\epsilon 1,N$ which was applied during the derivation of the formula. Now we have

found the Green's functions of the overlayer we can proceed with the final step in finding the Green's functions of the trilayer.

2.4.3 Analytic solution for the Green's function of the spacer layer in a trilayer

The final step in finding the Green's functions of a trilayer is to deposit a semi-infinite crystal onto the overlayer as shown in Figure 2.16. The cleavage plane shown

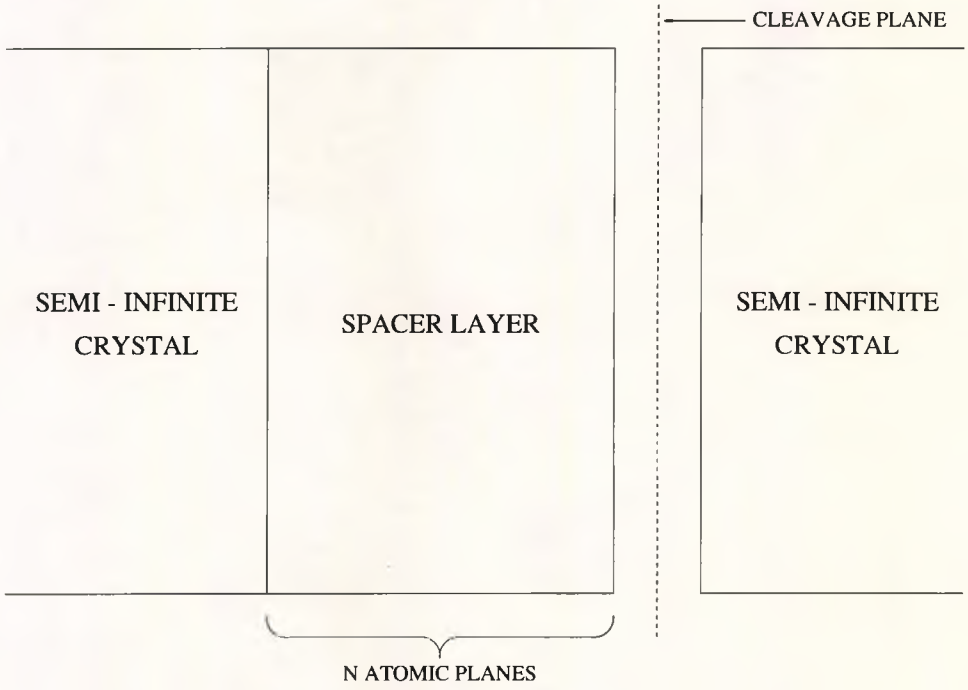

Figure 2.16: Diagram of a trilayer.

in the diagram is just the mathematical device used to disconnect the semi-infinite crystal from the overlayer. Once disconnected the electrons are not able to hop across the cleavage plane. The semi-infinite crystal is reconnected to the overlayer

using Dyson's Equation which is

$$G^{Tr}(i,j) = G^{ov}(i,j) + \sum_{p,q} G^{ov}(i,p)W(p,q)G^{Tr}(q,j), \tag{2.75}$$

where G^{ov} are the Green's functions of the system with the cleavage plane and G^{Tr} are the Green's functions of the system without the cleavage plane. Here the only non-zero perturbation matrix elements $W(p,q)$ are:-

$$\begin{aligned} W(N,N+1) &= < k_{||}, N \mid H \mid k_{||}, N+1 > = T \qquad \text{and} \\ W(N+1,N) &= < k_{||}, N+1 \mid H \mid k_{||}, N > = T, \end{aligned} \tag{2.76}$$

where W(N,N+1) and W(N+1,N) are the hopping of electrons from the N th atomic plane of the overlayer to the surface atomic plane of the right semi-infinite crystal and vice versa. T is the hopping of electrons from atom to atom. Substituting the values of the perturbation given by Equation 2.76 into Dyson's Equation gives the Green's function of the trilayer to be

$$G^{Tr}(i,j) = G^{ov}(i,j) + T(G^{ov}(i,N)G^{Tr}(N+1,j) + G^{ov}(i,N+1)G^{Tr}(N,j)).$$

Assuming that $i,j \epsilon 1,N$ leads to $G^{ov}(i,N+1) = 0$ because electrons cannot hop across the cleavage plane. The formula for the Green's functions of a trilayer simplifies to

$$G^{Tr}(i,j) = G^{ov}(i,j) + TG^{ov}(i,N)G^{Tr}(N+1,j). \tag{2.77}$$

The only term in Equation 2.77 we do not yet know is $G^{Tr}(N+1,j)$. This is found by setting i=N+1 in Dyson's Equation Equation 2.75 taking account of the perturbation and assuming that $i,j \epsilon 1,N$. After performing these tasks we find that

$$G^{Tr}(N+1,j) = TG^{ov}(N+1,N+1)G^{Tr}(N,j). \tag{2.78}$$

Similarly $G^{Tr}(N,j)$ is found by setting i=N in Dyson's Equation

$$G^{Tr}(N,j) = G^{ov}(N,j) + TG^{ov}(N,N)G^{Tr}(N+1,j). \tag{2.79}$$

Substituting the solution of $G^{Tr}(N,j)$ given by Equation 2.79 into Equation 2.78 and simplifying gives

$$G^{Tr}(N+1,j) = \frac{TG^{ov}(N+1,N+1)G^{ov}(N,j)}{1-T^2G^{ov}(N,N)G^{ov}(N+1,N+1)}. \tag{2.80}$$

Placing the solution of $G^{Tr}(N+1,j)$ given by Equation 2.80 into Equation 2.77 gives

$$G^{Tr}(i,j) = G^{ov}(i,j) + \frac{T^2G^{ov}(N+1,N+1)G^{ov}(i,N)G^{ov}(N,j)}{1-T^2G^{ov}(N,N)G^{ov}(N+1,N+1)}, \tag{2.81}$$

for the analytic Green's function of the trilayer. As before with the formula for the Green's functions of the overlayer given by Equation 2.74 the formula for the Green's functions of the trilayer is only valid for the atomic planes making up the spacer layer. Again this is due to the assumption that $i,j\epsilon 1,N$ which was used during the derivation of Equation 2.81.

Now we need to demonstrate that the spectral density can be Fourier analysed. To do this we need to show the spectral density $\frac{1}{N}G^s(E,k_{||},N)$ is a periodic function in N and the discrete variable N can be mathematically viewed as a continuous one. Using Equations 2.67, 2.74 and 2.81 one can eventually find that

$$\sum_{i=1}^{N} G^{Tr}(i,i) = \sum_{i=1}^{N} -\frac{\sin(i\theta+\psi)\sin((i-N-1)\theta-\zeta)}{T\sin(\theta)\sin((N+1)\theta+\psi+\zeta)}, \tag{2.82}$$

where

$$\tan\psi = \frac{TG^{cl}(0,0)\sin\theta}{1-TG^{cl}(0,0)\cos\theta}$$

and

$$\tan\zeta = \frac{TG^{cl}(N+1,N+1)\sin\theta}{1-TG^{cl}(N+1,N+1)\cos\theta}.$$

Here $G^{cl}(0,0)$ is the surface Green's function of the left semi-infinite crystal and $G^{cl}(N+1,N+1)$ is the surface Green's function of the right semi-infinite crystal. Now

$$\frac{1}{N}G^{s}(E,k_{\|},N) = -\frac{1}{\pi}\sum_{i=1}^{N} ImG_{ii}^{Tr}(E,k_{\|},N) \tag{2.83}$$

so by using Equations 2.82 and 2.83 we obtain

$$\begin{aligned}\frac{1}{N}G^{s}(E,k_{\|},N) &= \frac{1}{\pi}Im\left(\frac{\cot((N+1)\theta+\psi+\zeta)}{2T\sin(\theta)}\right) \\ &\quad -\frac{1}{N\pi}Im\left(\sum_{i=1}^{N}\frac{\cos(2i\theta-(N+1)\theta+\psi-\zeta)}{2T\sin(\theta)\sin((N+1)\theta+\psi+\zeta)}\right).\end{aligned} \tag{2.84}$$

It is now clear from Equation 2.84 that the discrete variable N can be mathematically viewed as a continuous one. One of the required conditions for Fourier analysis is therefore fulfilled. We can also see from this Equation that as

$$N\to\infty \quad \text{then} \quad \frac{1}{N}G^{s}(E,k_{\|},N) \to \frac{1}{\pi}Im\left(\frac{\cot((N+1)\theta+\psi+\zeta)}{2T\sin(\theta)}\right), \tag{2.85}$$

which clearly demonstrates that the spectral density behaves asymptotically like a periodic function in N as N becomes large. The other condition for Fourier analysis is therefore satisfied.

2.5 Results for a single orbital trilayer

Here in this section we outline an example of oscillatory exchange coupling for a single orbital (001) trilayer. The parameters describing each layer within the trilayer have been chosen arbitrarily as the aim of this section is to give a visual demonstration of oscillatory exchange coupling and to test all the techniques employed in the model. The parameters have been chosen so that the electrons see a finite potential well and the Fermi energy level lies above the top of the well. In doing so we ensure there is oscillatory exchange coupling and no bound states. A more comprehensive investigation of the possible situations which can occur is given in the next Chapter for the two orbital trilayer. The bands employed in our computation of J(N) are shown in Figure 2.17.

Once the band structure of the trilayer has been set we can proceed with the computation of the exchange coupling. The exact result is first calculated using the numerical approach. J(N) is then computed using the analytic approach of the SPA and finally we compare the two results to ensure they are both in agreement with each other.

Numerical Approach

To compute the exchange coupling using the numerical approach we use the method as set out in Section 2.2. The final step when computing J(N) is given by Equation 2.22. The thermodynamic potentials $\Omega^{\uparrow\downarrow}(N)_{FM}$ and $\Omega^{\uparrow\downarrow}(N)_{AF}$ in this formula are calculated using Equation 2.34, where the summation over $k_{||}$ is per-

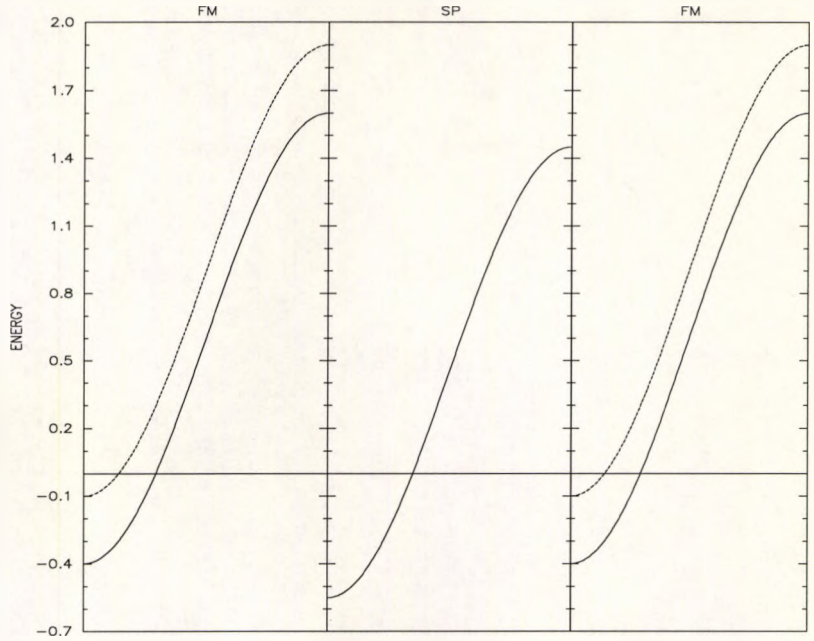

Figure 2.17: Plot of the energy bands of a single orbital (001) trilayer. The middle graph represents the up and down spin bands of the spacer layer. The graphs to the left and right show the up (dashed line) and down (solid line) spin bands of the ferromagnetic layers. Finally the straight solid line is the Fermi energy level.

formed using the method as set out in Section 2.2.2. It will be remembered that the number of $k_{||}$ points used in the summation is arrived at trial and error until the results converge to an acceptable accuracy. So we first need to ensure the results do indeed converge and secondly we need to ascertain how many $k_{||}$ points are needed to achieve convergence for this example of exchange coupling. To do this we start with a small number of $k_{||}$ points and increase the number of points comparing the results of each step with the results obtained from the previous step. There are two things to note about all the graphs in this section. They all have a cubic spline fitted to the data and the vertical axes should read $J(N) \times a^2$, where a is the inter-atomic

distance.

We start in Figure 2.18 by comparing the dependence of the exchange coupling on the spacer thickness for 528 and 2080 points in the $k_{||}$ summation. It is clear from this graph that the results have not yet converged and conclude that more than 2080 $k_{||}$ points are needed in the summation method. We next compare the exchange coupling for 2080 and 8256 $k_{||}$ points in Figure 2.19. As before the results have not yet converged and conclude again that more points are needed in the summation. However the graph does show signs of convergence for smaller spacer thicknesses. In Figure 2.20 we compare the exchange coupling for 8256 and 32896 points in the $k_{||}$ summation. The graph clearly shows the results are converging well and the evidence suggests that 32896 points in the $k_{||}$ summation is sufficient for this example of exchange coupling. To check this we compare the exchange coupling for 32896 and 131328 points in Figure 2.21. This graph clearly shows that it is sufficient for this example to use 32896 points in the $k_{||}$ summation and the results have indeed converged.

One interesting point to note about the convergence is how quickly the results converge. If we look at all four graphs again we can see the results converge for smaller spacer thicknesses more quickly than larger spacer thicknesses. A feature of the summation method is the results converge more quickly when the amplitude of the exchange coupling is greater. The amplitude of the exchange coupling decays like $1/N^2$ so we naturally obtain quicker convergence for smaller spacer thicknesses as the amplitude of the oscillations are greatest here.

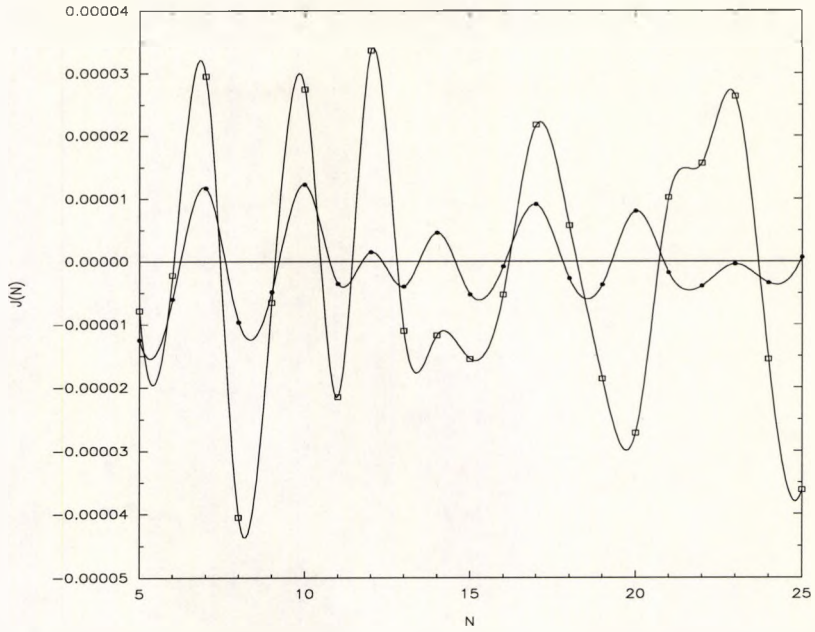

Figure 2.18: Comparison of the exchange coupling obtained using 528 (squares) and 2080 (circles) $k_{||}$ points in the $k_{||}$ summation for the reduced BZ.

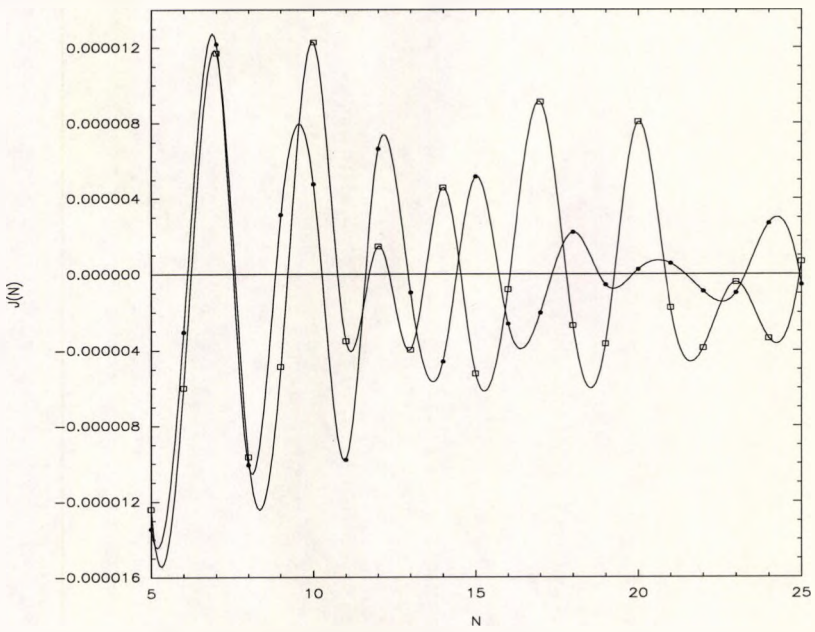

Figure 2.19: Comparison of the exchange coupling obtained using 2080 (squares) and 8256 (circles) $k_{||}$ points in the $k_{||}$ summation for the reduced BZ.

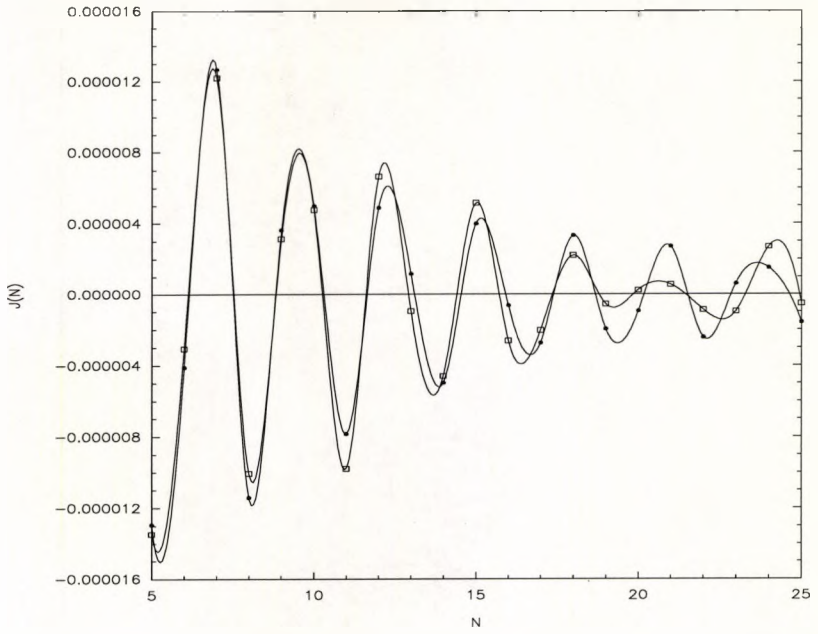

Figure 2.20: Comparison of the exchange coupling obtained using 8256 (squares) and 32896 (circles) $k_{||}$ points in the $k_{||}$ summation for the reduced BZ.

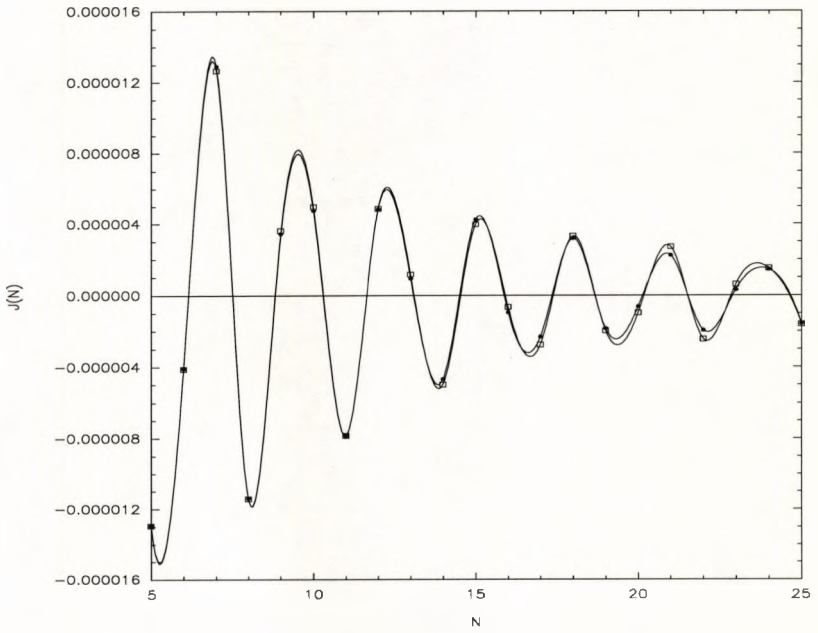

Figure 2.21: Comparison of the exchange coupling obtained using 32896 (squares) and 131328 (circles) $k_{||}$ points in the $k_{||}$ summation for the reduced BZ.

Stationary phase approximation

Now we compute the exchange coupling using the analytic approach of Section 2.3. The final step when computing J(N) is obtained using the same formula as for the numerical approach ie Equation 2.22. The thermodynamic potentials $\Omega^{\uparrow\downarrow}(N)_{FM}$ and $\Omega^{\uparrow\downarrow}(N)_{AF}$ in this equation are calculated by using Equation 2.49 this time. The factors in this equation are computed using the methods as set out in Section 2.3.3.

We use the spectral density to obtain the Fourier coefficients and the spectral density for the up spin band of the ferromagnetic configuration of the trilayer is shown in Figure 2.22. The down spin band is shown in Figure 2.23. The spectral density for the up and down spin bands of the antiferromagnetic configuration of the trilayer is shown in Figure 2.24. Then using the periodicity of the spectral density, which for this case is $\simeq 2.85$ atomic planes, we shift the spectral density using the shifting method as described in Section 2.3.3. The shifted spectral densities are shown in Figure 2.25. Using the shifted spectral densities it is trivial to obtain the Fourier coefficients and then the exchange coupling, which is shown in Figure 2.26. As for the numerical results the vertical axis in the graphs showing the exchange coupling should read $J(N) \times a^2$, where a is the inter-atomic distance and a cubic spline has been fitted to the data.

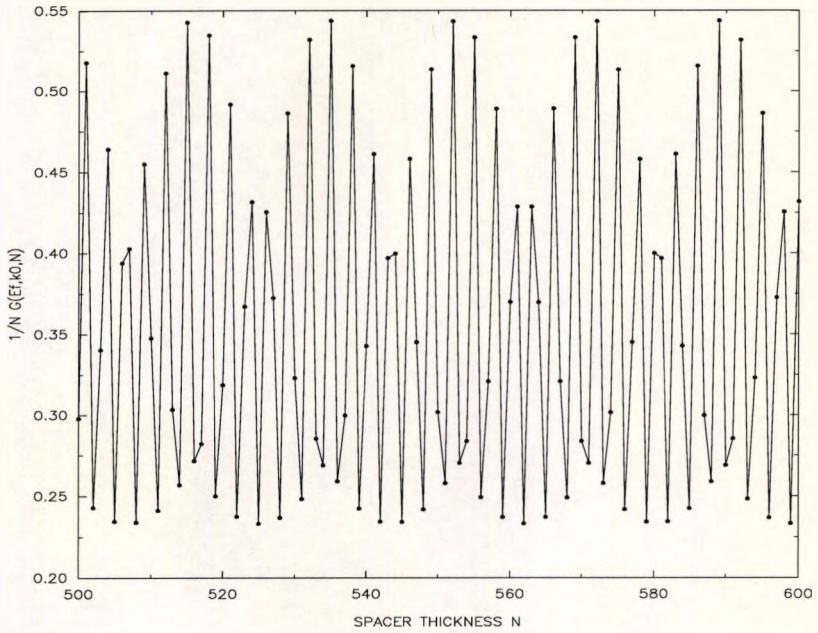

Figure 2.22: Dependence of the spectral density on the spacer thickness N. It is evaluated at $k_x = k_y = 0$ and $E = E_f$. The solid line simply connects the points as a visual aid.

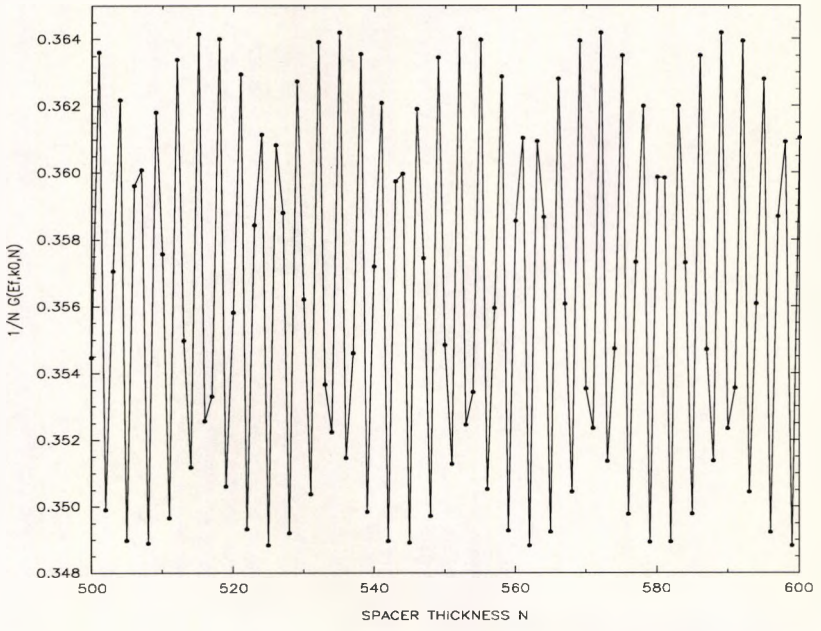

Figure 2.23: Dependence of the spectral density on the spacer thickness N. It is evaluated at the $k_x = k_y = 0$ and $E = E_f$. The solid line simply connects the points as a visual aid.

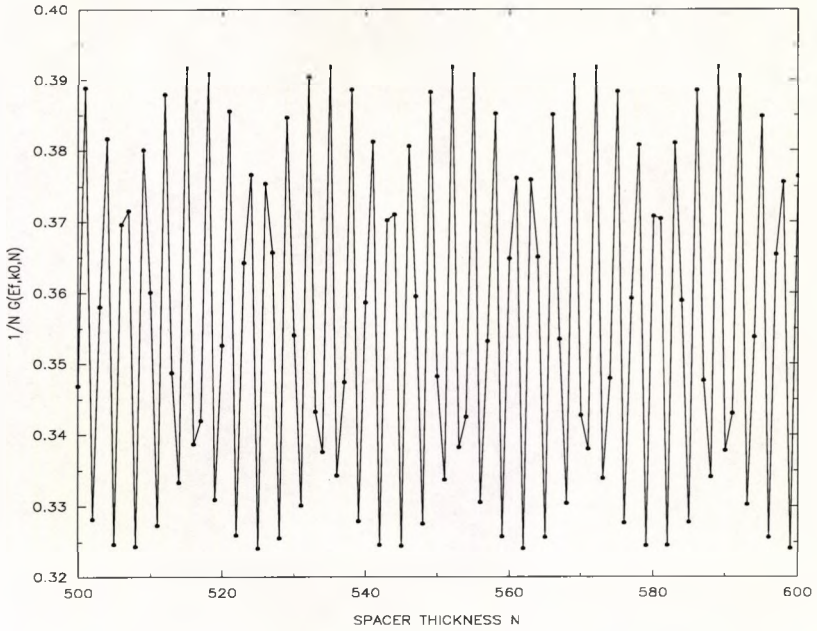

Figure 2.24: Dependence of the spectral density on the spacer thickness N. It is evaluated at $k_x = k_y = 0$ and $E = E_f$. The solid line simply connects the points as a visual aid.

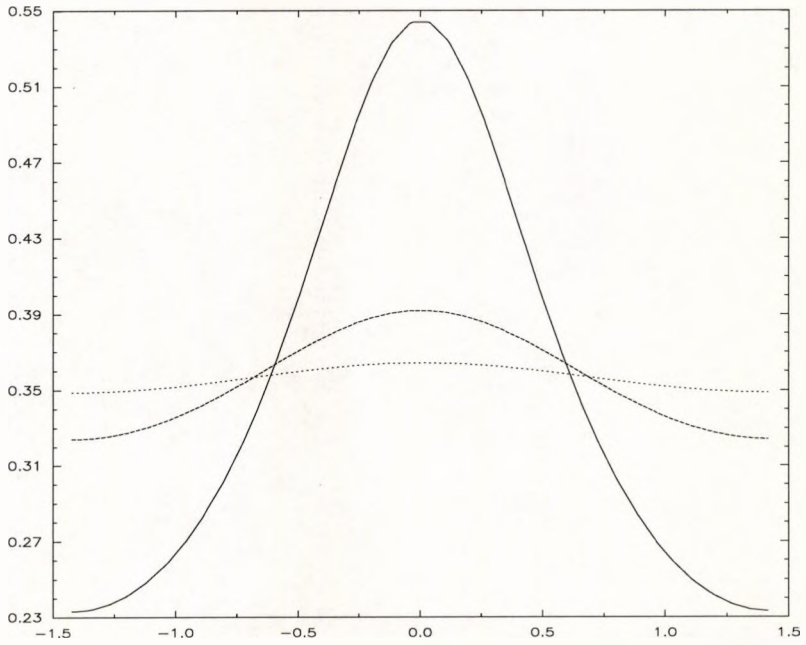

Figure 2.25: Shifted spectral densities of the up spin band (solid line) and down spin band (dotted line) of the ferromagnetic configuration and the up and down spin bands (dashed line) of the antiferromagnetic configuration.

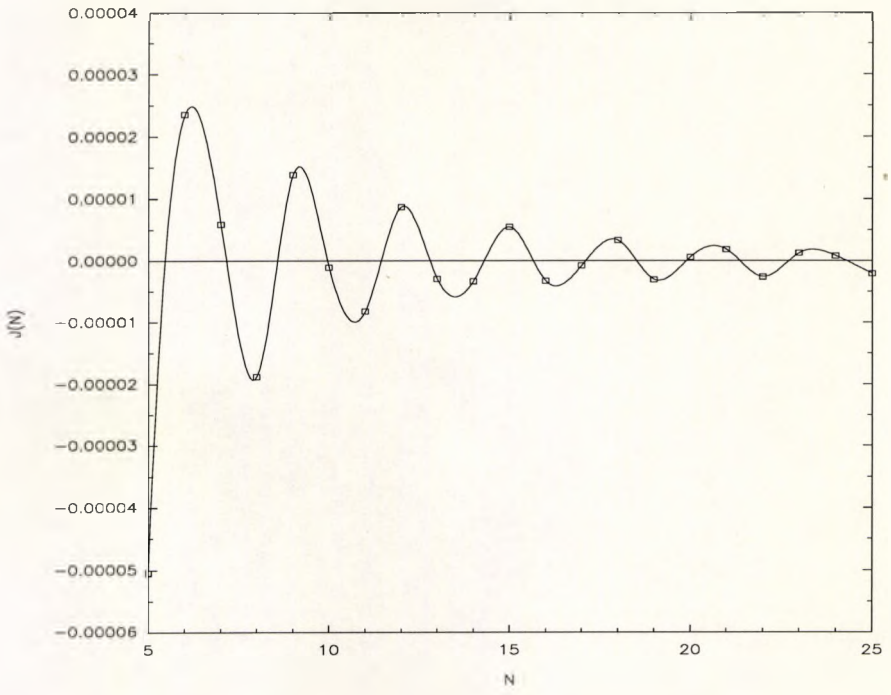

Figure 2.26: Exchange coupling for (001) trilayer associated with the point $k_x = k_y = 0$.

Comparison of results

Now we have computed the exchange coupling using the analytic and numerical approaches we can compare the results to check they are in good agreement with each other. This is displayed in Figure 2.27.

It is clear from this graph that the periods are in good agreement with each other and for this example p$\simeq$ 2.85 atomic planes. However there appears to be a large difference between the amplitude of the SPA and numerical approach for smaller spacer thicknesses. For larger spacer thicknesses the amplitudes converge and the two sets of data are in closer agreement with each other. Also there appears to be a phase shift between the two sets of data. The apparent large difference in the amplitudes and the phase shift can be explained in terms of a phase shift in the asymptotic formula, see Ref [43]. It is a consequence of limiting the asymptotic expansion to the leading term which is of order $1/N^2$ and when the formula is expanded to include terms in $1/N^3$ this apparent phase shift disappears. The apparent phase shift coupled with a short period of oscillations result in an apparently large difference between the two sets of data. A long period would not result in such a large difference. For larger spacer thicknesses the apparent phase shift becomes less significant and the results should converge which is clearly shown in Figure 2.27.

We conclude that apart from the phase shift the two methods are in close agreement with each other. This demonstrates the period of oscillations is determined by the properties of the spacer layer Fermi surface.

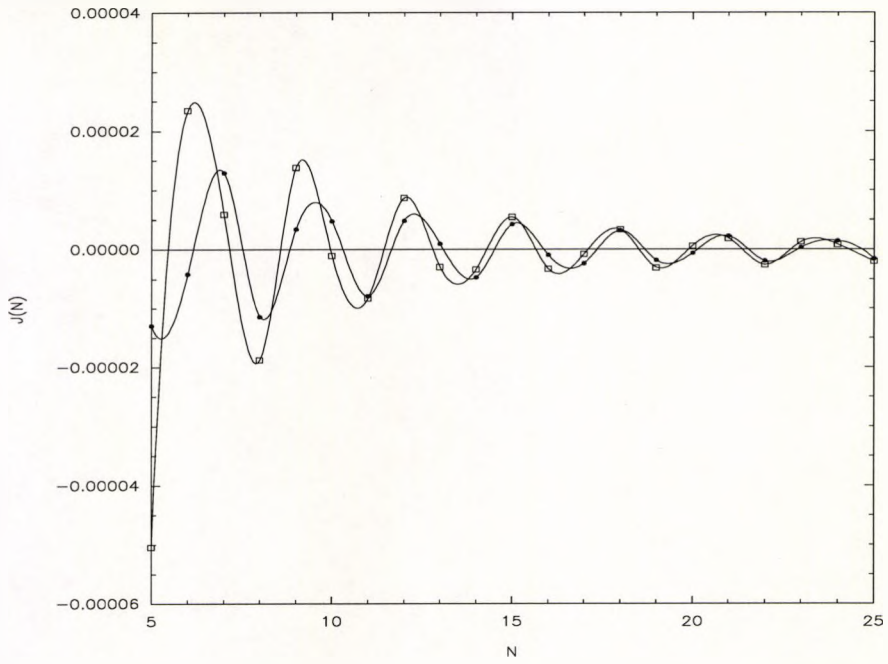

Figure 2.27: Comparison of the exchange coupling obtained using the numerical approach (solid circles) and the SPA (open squares).

Chapter 3

Two band theory of exchange coupling in a trilayer

Introduction

In Chapter 2 we described how to compute the exchange coupling for a single orbital trilayer. The type of metals we most wish to model contain considerably more than just one band of electrons, which would appear to render the model too simple to be of much practical use. However the single orbital model is useful to help understand the physical mechanisms involved in exchange coupling. Also as not all bands in a metal necessarily contribute to the oscillatory exchange coupling some may be neglected for computational purposes. Therefore it may be possible to model exchange coupling realistically using fewer bands than are actually present.

Oscillatory exchange coupling occurs when there is either partial or complete confinement of the electrons to the spacer layer. Partial confinement occurs when

there is a potential well formed by the trilayer and the Fermi energy level lies above the top of the potential well. Complete confinement occurs when the Fermi energy level lies within the potential well formed by the trilayer. Visualised another way oscillatory exchange coupling occurs when a band of electrons in the spacer layer is only partially filled with electrons. With the presence of more than one band of electrons it is possible for electrons to hop from band to band in the same way they hop from atom to atom, which is called hybridization, although this is not always the case. If a band of electrons is not intersected by the Fermi energy level ie it is either completely empty or full and does not hybridize with any other band that is partially filled then this band does not contribute to the oscillatory exchange coupling. Any band which fulfills these criteria can be neglected for computational purposes. In this way one can see that the one band and the two band model, which we describe in this Chapter, has a greater potential for application than is at first apparent.

In transition metals the less mobile d electrons are responsible for the magnetic properties and the more mobile s electrons are responsible for the transport properties. The width of a band reflects the degree of electron hopping and it follows in transition metals that the s-band is much wider in energy than the d-band. The one band model of exchange coupling cannot be used for a Co/Cu trilayer, for example, because although only the s-band is intersected by the Fermi energy level in the spacer layer it hybridizes with the d-band. The minimum model needed here is a two band model which includes hybridization between the bands. All other bands

may be neglected for computational purposes because they are all either empty, full or do not hybridize with the s-band. One of the major motivations in generalizing the models described in Chapter 2 is so that we can model trilayers such as Co/Cu which cannot be adequately described by the single orbital model. In doing so we also extend the possible applications of the quantum well theory of oscillatory exchange coupling.

In this Chapter we outline the method for calculatng the exchange coupling for a trilayer that is made up of two semi-infinite ferromagnets separated by a non-magnetic spacer layer. We apply the model to a two band trilayer in the (001) orientation. The band structure is modelled using the tight-binding band structure where only nearest neighbour hopping of electrons is considered. The lattice structure is simple cubic and finally we consider the case when the temperature is zero. The models will be discussed in such a way that makes the generalization to more than two bands of electrons simple, however in this Chapter we consider a trilayer with two bands only. As the model is the generalization of the one band model the outline of this Chapter takes a similar form to the last one.

We start in Section 3.1 by explaining how to obtain the Green's function of an arbitrary atomic plane in the spacer layer. Once this has been obtained we can express the exchange coupling J(N), where N is the spacer thickness, in terms of these Green's functions. In Section 3.2 we compute the exchange coupling numerically using the same techniques that were employed in Section 2.2 for the one band trilayer. The time required to compute the exchange coupling numerically for the

two band trilayer is a lot greater than for the single orbital trilayer. The reason for this lies in the fact that all the quantities that describe the two band trilayer are all matrices and not scalar quantities as in the single orbital trilayer. This renders the numerical approach even more impractical than for the case of a single orbital trilayer, although feasible. To overcome this problem we apply the SPA to the two band trilayer in Section 3.3 and by deriving the analytic asymptotic formula for the exchange coupling for the two band trilayer we can evaluate the exchange coupling in a reasonable time. Finally in Section 3.4 we investigate what effect the hybridization between the s and d bands has on exchange coupling by considering a variety of different trilayers.

3.1 Green's function of an arbitrary atomic plane in the spacer layer

Obtaining the Green's function for an arbitrary atomic plane in the two band spacer layer involves the same three steps that were used for the one band trilayer and they are:-

1. Obtaining the surface Green's function of the substrate.

2. Depositing adlayers onto the substrate.

3. Joining together two substrates, with the appropriate number of adlayers deposited on them to create the trilayer.

When outlining this process for the single band trilayer in Section 2.1 we started with the adlayering procedure. This is because the adlayering algorithm was used to find the surface Green's function of the semi-infinite substrate. We start by explaining how to deposit adlayers onto the substrate for the two band model for the same reason. This time it is used in two different methods we tried when solving for the surface Green's function of the semi-infinite substrate.

3.1.1 Adlayering

As for one band adlayering two band adlayering is also the mathematical analogue of experimentally depositing atomic planes onto a substrate. Here we generalize the algorithm described in Refs [36], [37] and Section 2.1.1 which obtains the surface

Green's function of many adlayers deposited onto a substrate. The difference here is the adlayers are now made up of two bands of electrons. When formulating the adlayering procedure the parameters that describe the atomic potentials and hopping integrals of each band of the adlayer are retained as variables of the procedure. This again enables us to model many different structures, as long as they have a simple cubic crystal lattice structure and at most two bands of electrons. Obviously due to the inclusion of the second band of electrons and the effect of the hybridization between the bands there are more potential applications for two band adlayering when compared to the single band adlayering. During the formulation of the two band adlayering procedure we only consider a semi-infinite substrate on which to deposit the adlayers. It is not a necessary condition in order to be able to proceed with the adlayering and can in fact be any thickness as long as it contains at least one atomic plane. Later on we use this proviso to help find the surface Green's function of a semi-infinite crystal. We start by considering how to deposit a single adlayer onto the semi-infinite crystal.

Single adlayer

Here we deal with how to deposit just one adlayer onto the substrate. This method of depositing an adlayer will be applied again in the next subsection thereby enabling us to deposit as many adlayers as required onto a substrate and not just the one. For the case of a single adlayer we have the situation as described in Figure 3.1.

The cleavage plane shown in the diagram is just the mathematical device used to

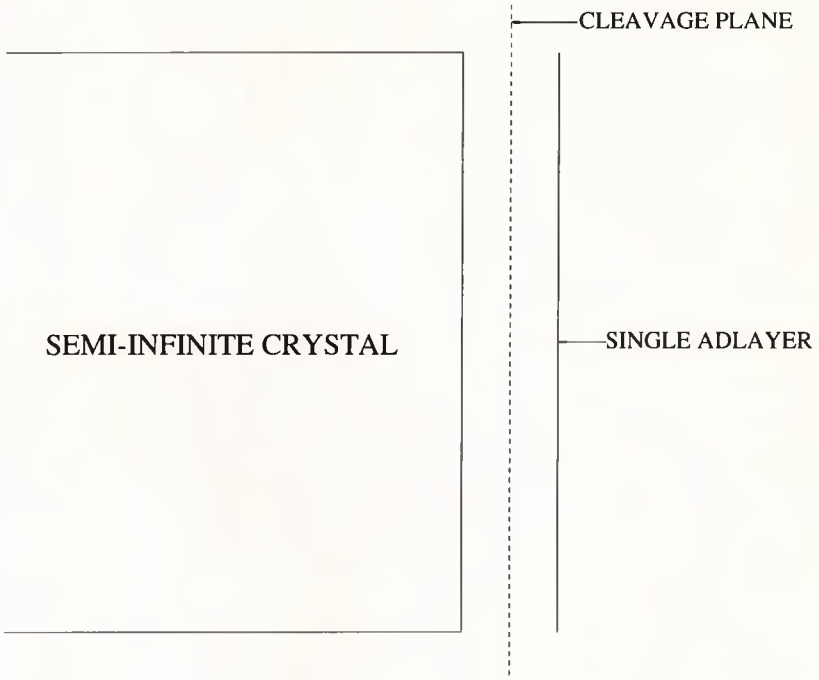

Figure 3.1: Diagram of a single adlayer or atomic plane deposited onto a semi-infinite crystal.

disconnect the adlayer from the substrate. Once disconnected electrons are not able to hop across the cleavage plane. The adlayer is then reconnected to the substrate using Dyson's Equation, which is

$$G^1(m,n) = G^0(m,n) + \sum_{p,q} G^0(m,p)W(p,q)G^1(q,n), \tag{3.1}$$

where G^0 are the Green's functions of the system with the cleavage plane, G^1 are the Green's functions of the system without the cleavage plane and W(p,q) describes the perturbation within the system.

Two types of perturbation are present and result from electrons being able to hop from atomic plane to atomic plane and the interaction of an electron with its

four nearest neighbours in its particular atomic plane. In this case the only non-zero perturbation matrix elements are:-

$$\begin{aligned} W(0,1) &= < k_{||}, 0 \mid H \mid k_{||}, 1 > &= T, \\ W(1,0) &= < k_{||}, 1 \mid H \mid k_{||}, 0 > &= T \qquad \text{and} \\ W(1,1) &= < k_{||}, 1 \mid H \mid k_{||}, 1 > &= W_1 = E_1 + 2T(cos(k_x a) + cos(k_y a)). \end{aligned} \tag{3.2}$$

Here T is the hopping integral or potential for an electron to hop from atom to atom. W(0,1) and W(1,0) is the hopping of the electrons from the substrate to the adlayer and vice versa. W(1,1) is the hopping of the electrons from atom to atom in the adlayer, E_1 is the atomic potential of the adlayer and finally a is the inter-atomic distance.

If we compare this answer with the one obtained at this point in the one band adlayering given by Equation 2.2 they would appear to be the same. There is one subtle but important difference here in the two band adlayering. To fully describe the band structure of the trilayer all the parameters and local Green's functions are no longer scalar but 2×2 matrices. This is the case throughout this Section. The hopping matrix T is

$$T = \begin{pmatrix} ts & tsd \\ tsd & td \end{pmatrix}, \tag{3.3}$$

where ts is the potential for electrons to hop from s-band to s-band, td the hopping of electrons from d-band to d-band and tsd is the potential for electrons to hop from s-band to d-band and vice versa. The hopping of elecrons from s-band to d-band is

called hybridization. E_1 is the atomic potential of the adlayer and is given by

$$E_1 = \begin{pmatrix} Es & 0 \\ 0 & Ed \end{pmatrix}, \tag{3.4}$$

where Es describes the atomic potential of the s-band and Ed the atomic potential of the d-band of the adlayer.

From this brief introduction into obtaining the Green's function of an arbitrary atomic plane in the spacer layer we can already see the similarities with the one band model. For the sake of simplicity we use the same terminology for the two band model as all the quantities describe the same basic physical processes. However it must be remembered that all of these quantities are now 2×2 matrices for the two band model and not scalar.

The Green's function of the single adlayer is obtained by setting m=n=1 in Equation 3.1 and once the perturbation defined by Equation 3.2 has been taken into account we are left with

$$\begin{aligned} G^1(1,1) = \; & G^0(1,1) + G^0(1,1)W_1G^1(1,1) + \\ & G^0(1,0)TG^1(1,1) + G^0(1,1)TG^1(0,1). \end{aligned}$$

In the presence of a cleavage plane electrons are unable to hop from the adlayer to the substrate and vice versa, hence

$$G^0(1,0) = G^0(0,1) = \begin{pmatrix} 0 & 0 \\ 0 & 0 \end{pmatrix}.$$

The formula for the Green's function of the single adlayer therefore simplifies to

$$G^1(1,1) = G^0(1,1) + G^0(1,1)W_1G^1(1,1) + G^0(1,1)TG^1(0,1), \tag{3.5}$$

where $G^0(1,1)$ is the Green's function of a single unconnected atomic plane and it is

$$G^0(1,1) = \frac{1}{E} \times \begin{pmatrix} 1 & 0 \\ 0 & 1 \end{pmatrix}. \tag{3.6}$$

It must be remembered that all the terms in Equation 3.5 are 2×2 matrices so we have to maintain the order of multiplication, unlike the single band adlayering. Putting the result from Equation 3.6 into Equation 3.5 and simplifying leaves us with

$$(E \times I - W_1)\, G^1(1,1) = I + TG^1(0,1), \tag{3.7}$$

where I is the 2×2 identity matrix. The only term we do not yet know is $G^1(0,1)$. This is found by setting $m = 0$ and $n = 1$ in Dyson's Equation, Equation 3.1 and taking account of the perturbation. We therefore find that

$$G^1(0,1) = G^0(0,0)TG^1(1,1),$$

where $G^0(0,0)$ is the surface Green's function of our substrate, which we call G^s. Its computation is not needed to explain the adlayering procedure so for the moment we just retain it as a variable of the adlayering algorithm. Its calculation is fully explained in Section 3.1.2, so

$$G^0(0,0) = G^s. \tag{3.8}$$

Using the solution of $G^1(0,1)$ and Equation 3.8 we find the Green's function of a single adlayer is

$$G^1(1,1) = (E \times I - W_1 - TG^sT)^{-1}, \tag{3.9}$$

where

$$W_1 = \begin{pmatrix} Es & 0 \\ 0 & Ed \end{pmatrix} + 2(cos(k_x a) + cos(k_y a)) \begin{pmatrix} ts & tsd \\ tsd & td \end{pmatrix}.$$

We now have a relationship for the exact Green's function of a single adlayer albeit in terms of the surface Green's function of the substrate G^s. It is important that we have to be strict about the order of multiplication of the terms in Equation 3.9 because they are all matrices.

Multi-adlayering

The process of depositing many adlayers onto a substrate is the same as depositing just one adlayer, the only difference is the process is repeated until the required number of adlayers have been deposited.

The Green's function of the second adlayer is found by treating the single adlayer deposited onto the substrate as the "substrate". Another adlayer is then deposited in exactly the same way as before. Thus setting $m = n = 2$ in Dyson's equation and taking account of the perturbation we find that

$$G^2(2,2) = \left(E \times I - W_2 - TG^1(1,1)T\right)^{-1}, \tag{3.10}$$

where

$$W_2 = E_2 + 2T(cos(k_x a) + cos(k_y a))$$

and E_2 is the atomic potential of the second adlayer. This process of depositing adlayers can be repeated for as long as required until after N steps we find that

$$G^N(N,N) = \left(E \times I - W_N - TG^{N-1}(N-1,N-1)T\right)^{-1}, \tag{3.11}$$

where

$$W_N = E_N + 2T(cos(k_x a) + cos(k_y a))$$

and E_N is the atomic potential of the N th adlayer. $G^N(N, N)$ is the surface Green's function of N adlayers deposited onto a substrate, as shown in Figure 3.2 and $G^{N-1}(N-1, N-1)$ is the surface Green's function of N-1 adlayers deposited onto the substrate.

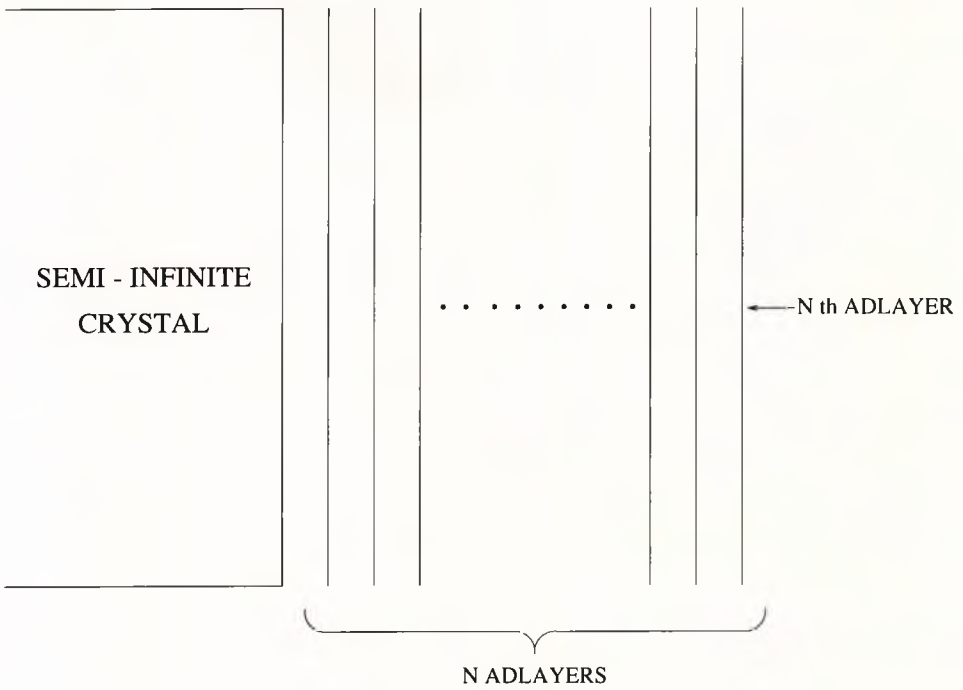

Figure 3.2: Diagram showing N adlayers or atomic planes deposited onto a semi-infinite crystal.

3.1.2 Surface Green's function of a semi-infinite crystal

In the previous section we described the deposition of adlayers onto a substrate where the subsrate is a semi-infinite crystal. In order to be able to proceed with

the adlayering algorithm we first need to find the surface Green's function of the semi-infinite crystal, which we labelled G^s. In Section 2.1.2 we obtained an analytic solution for the surface Green's function of the one band semi-infinite crystal using the adlayering procedure. Similar to the adlayering procedure itself the best approach would appear to be the generalization of the one band analytic solution of G^s to the two band semi-infinite crystal. Unfortunately although this is feasible the execution of such an approach renders it unviable for practical use. When solving for G^s for the one band semi-infinite crystal we needed to decide which branch of the solution to take. Since there were only two possible branches of the solution this task is relatively simple. As a result of all the terms being matrices in the two band model there are considerably more than just two branches in the solution of G^s. This makes the generalization of the analytic solution too complex. Therefore in this section we outline two different trial methods we used when solving for G^s for the two band crystal.

Method 1

In our first trial method we try to obtain a good approximation for the fully hybridized surface Green's function of the semi-infinite crystal with two bands of electrons. We do this by depositing hybridized adlayers onto an unhybridized semi-infinite crystal. Once enough hybridized adlayers have been deposited then the surface Green's function of this crystal should hopefully provide the approximation to G^s we seek. We use an unhybridized semi-infinite crystal as the initial "starting

block" because it is likely the approximation to G^s will be achieved by depositing less adlayers than a thinner finite starting block would need and would therefore require less computational effort.

The surface Green's function of the unhybridized crystal takes the following form. The off diagonal matrix elements are zero because there is no hybridization between the bands in other words the electrons cannot hop from the s-band to the d-band and vice versa. The diagonal elements are obtained using the analytic solution for the surface Green's function of a semi-infinite crystal with a single band of electrons, which is given by Equation 2.15. This solution can be used here because when there is no interaction of the s and d band electrons we can mathematically treat each band as though it is a single band. We call G_{UNS} the surface Green's function of the s-band and G_{UND} the surface Green's function of the d-band. The surface Green's function of the unhybridized two band semi-infinite crytsal G^s_{UN} will therefore look something like

$$G^s_{UN} = \begin{pmatrix} G_{UNS} & 0 \\ 0 & G_{UND} \end{pmatrix}.$$

Now we have the surface Green's function of the unhybridized semi-infinite crystal we deposit hybridized adlayers onto it using the two band adlayering which is outlined in Section 3.1.1. The hybridized adlayers are of exactly the same material as the unhybridized semi-infinite crystal except the hybridization between the two bands has been switched on. Once enough hybridized adlayers have been deposited onto the unhybridized crystal then the surface Green's function of this crystal should

provide us with a very good approximation to the surface Green's function of the hybridized semi-infinite crystal and will look something like

$$G^s_{HY} = \begin{pmatrix} G_{HYS} & G_{HYSD} \\ G_{HYSD} & G_{HYD} \end{pmatrix},$$

where the off-diagonal matrix elements G_{HYSD} are now non-zero. This reflects the fact that electrons are now able to hop from s-band to d-band and vice versa in the fully hybridized crystal.

Now we need some way of demonstrating that this trial method gives the correct approximation to the fully hybridized surface Green's function of the semi-infinite crystal with two bands of electrons we seek. We recall from Section 2.3.3 that the Fourier coefficients in the SPA were obtained from the shifted spectral density. The shifted spectral density can be used here to test our first trial method. As we deposit more hybridized adlayers, the surface Green's function of this crystal should tend towards the surface Green's function of a fully hybridized semi-infinite crystal, hence the shifted spectral density will converge. Once the shifted spectral density converges then we will have shown that this trial method works and will also tell us how many hybridized adlayers need to be deposited onto the unhybridized crystal.

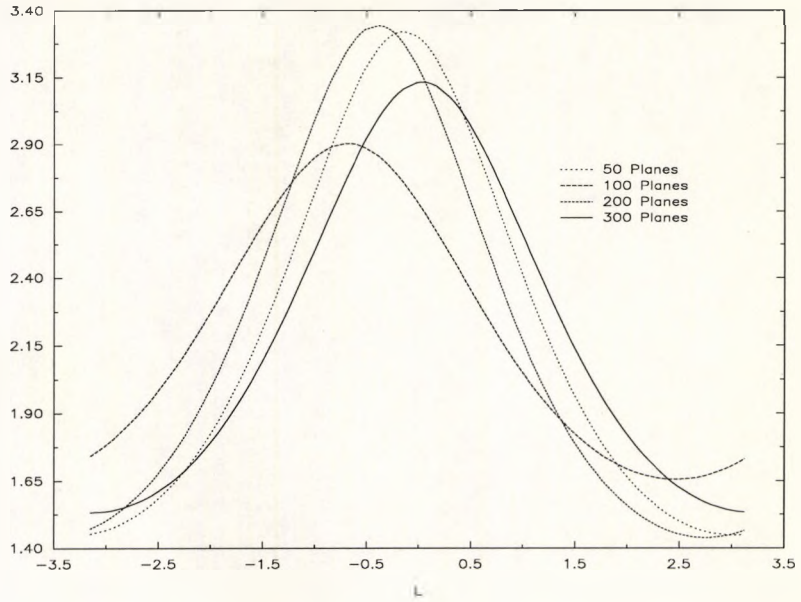

Figure 3.3: Diagram showing plots of the shifted spectral density with 50, 100, 200 and 300 hybridized adlayers or atomic planes deposited onto both the left and right semi-infinite unhybridized crystals.

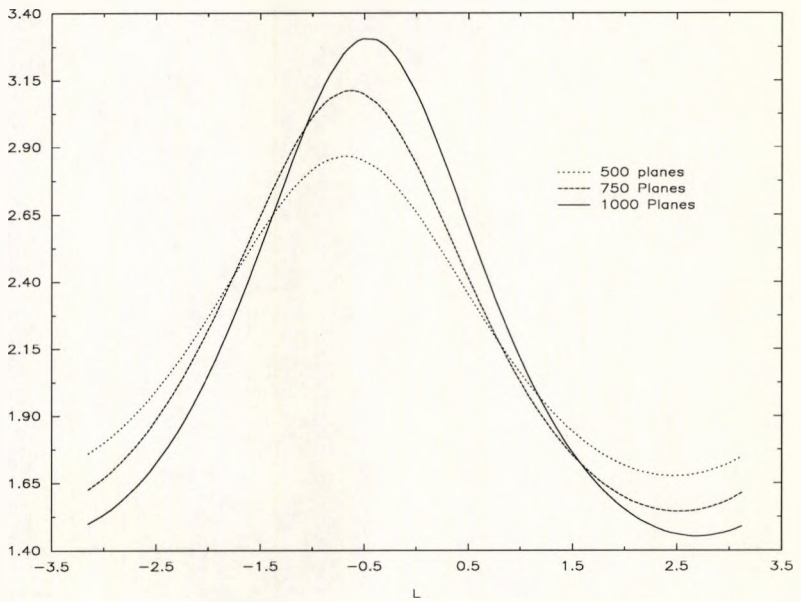

Figure 3.4: Diagram showing plots of the shifted spectral density with 500, 750 and 1000 hybridized adlayers or atomic planes deposited onto both the left and right semi-infinite unhybridized crystals.

Figures 3.3 and 3.4 are made up of several plots of the shifted spectral density. We start in Figure 3.3 by depositing 50 hybridized adlayers onto both the left and right unhybridized semi-infinite crystals. This is slowly increased until 300 adlayers have been deposited. By 300 adlayers we should at least be seeing some evidence that the shifted spectral density is converging, which it clearly isn't. It would appear from this that the shifted spectral density is in some way dependent on the thickness of the hybridized adlayers. To demonstrate this is the case we deposit 500, 750 and 1000 hybridized adlayers onto the unhybridized semi-infinite crystals in Figure 3.4. From this figure we can clearly see that the shifted spectral density does not converge. From this we conclude that trial method 1 does not give the correct approximation to the surface Green's function of a fully hybridized semi-infinite crystal and we reject it as a possible solution.

To see why this is so and explain what is happening we need to look at the energy bands and some basic quantum mechanics. We start by comparing the bulk energy bands of the unhybridized crystal with the hybridized adlayers. These plots are given in Figure 3.5.

Looking at the energy bands in Figure 3.5 we see that the hybridization causes a shift in the energy bands. This means that our trial method has introduced two shallow potential barriers at the edge of the potential well. The potential barriers originate from the hybridized adlayers that were deposited onto the unhybridized semi-infinite crystal. So diagrammatically the trilayer now looks like Figure 3.6.

We conclude that the potential barriers must be the source of the unexpected

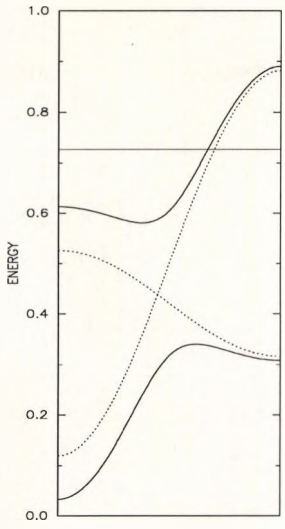

Figure 3.5: Comparison of the energy bands of the unhybridized semi-infinite crystal (Dotted lines) and the hybridized adlayers (Solid lines). The straight solid line is the Fermi energy level.

results obtained in Figure 3.3 and 3.4 and the shifted spectral density is in some way dependent on the thickness of the potential barriers. To gain some insight as to what the effect the potential barriers have let us consider the case of a single potential barrier of height V_0, see Figure 3.7. In particular we look at how the width of the barrier affects the transmission and reflection of the electrons through the barriers. We do this using the parabolic band model, Refs [44] and [45]. There are two possible scenarios, one is when the energy level is less than the height of the potential barrier and the other is when the energy level is greater than the height of the potential barrier.

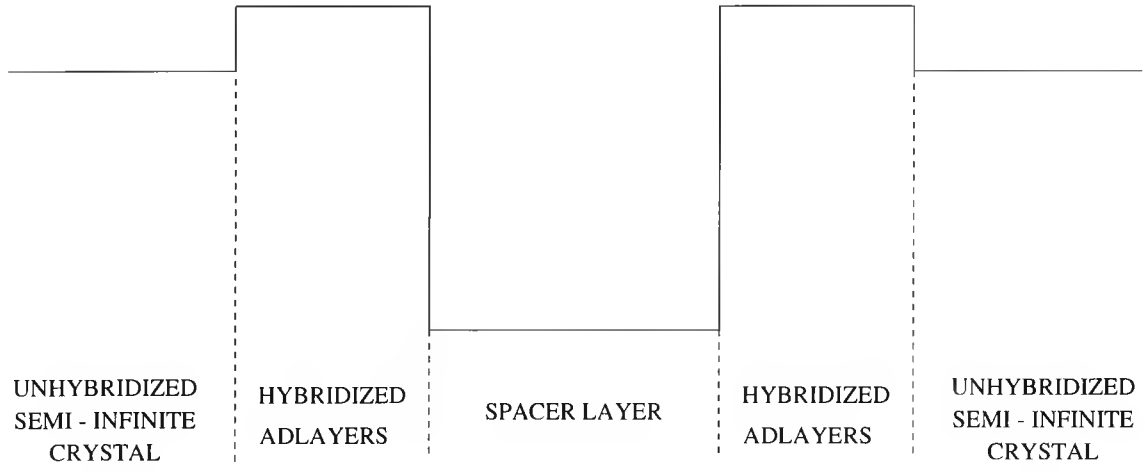

Figure 3.6: Potential well plus barriers.

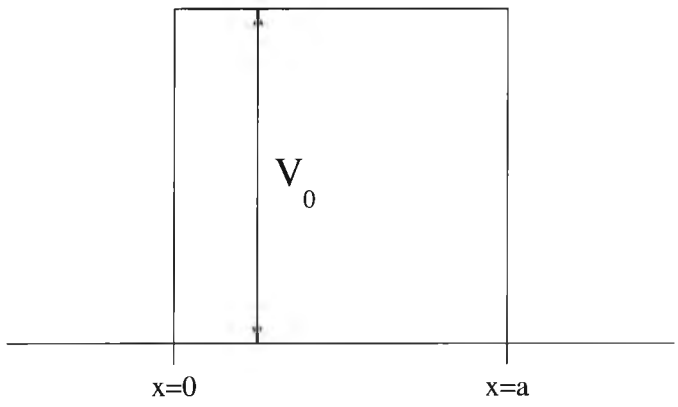

Figure 3.7: Diagram of a potential barrier of height V_0 and width a.

$\epsilon < V_0$

We first consider the case when the energy level ϵ is less than the height the potential barrier V_0. The three wave equations in this case are:-

$$\begin{aligned} \Psi_1 &= A\exp\left(ix\sqrt{\epsilon}\right) + B\exp\left(-ix\sqrt{\epsilon}\right) && x < 0 \\ \Psi_2 &= C\exp\left(x\sqrt{V_0-\epsilon}\right) + D\exp\left(-x\sqrt{V_0-\epsilon}\right) && 0 \le x \le a \\ \Psi_3 &= E\exp\left(ix\sqrt{\epsilon}\right) && x > a \end{aligned} \tag{3.12}$$

and the Transmission and Reflection coefficients are given by

$$\begin{aligned} R &= \frac{|E|^2}{|A|^2} \\ T &= \frac{|B|^2}{|A|^2} \\ R+T &= 1 \end{aligned} \tag{3.13}$$

Without loss of generality we set $A = 1$. The wave function must be continuous at all points thoughout the three regions. We therefore match the wave functions at the edge of the potential barrier ie $x = 0$ and $x = a$. Also we are considering the case of a finite potential barrier. When we have a finite potential barrier then the first derivative of Ψ must also be continuous in all regions. We therefore match the first derivative of Ψ at $x = 0$ and $x = a$ as well. We now have four constants and four boundary conditions which means we can obtain the values of all the coefficients from the four boundary equations which are:-

$$\begin{aligned} (a) \qquad 1 + B &= C + D \\ (b) \qquad i\sqrt{\epsilon}(1 - B) &= (C - D)\sqrt{V_0 - \epsilon} \\ (c) \qquad E\exp(ia\sqrt{\epsilon}) &= C\exp(a\sqrt{V_0 - \epsilon}) + D\exp(-a\sqrt{V_0 - \epsilon}) \\ (d) \quad Ei\sqrt{\epsilon}\exp(ia\sqrt{\epsilon}) &= \sqrt{V_0 - \epsilon}\left(C\exp(a\sqrt{V_0 - \epsilon}) - D\exp(-a\sqrt{V_0 - \epsilon})\right) \end{aligned} \tag{3.14}$$

By using Equations 3.13 and 3.14 we find that the transmission coefficient T is

$$T = \frac{4\epsilon(V_0 - \epsilon)}{4\epsilon(V_0 - \epsilon) + V_0^2 \sinh^2(a\sqrt{V_0 - \epsilon})} \qquad \epsilon < V_0 \tag{3.15}$$

and the Reflection coefficient R is

$$R = \frac{V_0^2 \sinh^2(a\sqrt{V_0 - \epsilon})}{4\epsilon(V_0 - \epsilon) + V_0^2 \sinh^2(a\sqrt{V_0 - \epsilon})} \qquad \epsilon < V_0. \tag{3.16}$$

The solution of T and R now gives us the required insight as to how the width of the potential barrier affects the passage of electrons through it when the energy level is less than the height of the height of the potential barrier. Increasing the width of the potential barrier, which is achieved by increasing the parameter a, reduces the transmission of the electrons through the barrier and consequently increases the reflection of electrons by the barrier. If we take the limit of $a \rightarrow \infty$ we see that there is no transmission of the electrons and all the electrons are reflected by the barrier.

Applying this to our trial method we can now explain what happens when the potential barriers were introduced for the case when the energy level is less than the height of the barriers. Depositing an increasingly large number of adlayers onto the unhybridized semi-infinite crystal translates into increasing the width of the potential barriers. This will restrict the motion of electrons from the substrates into the spacer layer and will have the effect of putting the spacer layer into an infinitely deep potential well at the limit of $a = \infty$. By looking at Figures 3.3 and 3.4 we can see that it is not this we are seeing here. We conclude that the potential barriers must have been smaller than the energy level. So we now look at the case when the energy level ϵ is greater than the height of the potential barrier.

$\epsilon > V_0$

We now consider the case when the energy level is greater than the height of the potential barrier. Again we set A equal 1 without loss of generality to simplify the

calculations. The three wave equations are:-

$$\begin{aligned}
\Psi_1 &= \exp\left(ix\sqrt{\epsilon}\right) + B\exp\left(-ix\sqrt{\epsilon}\right) && x < 0 \\
\Psi_2 &= C\exp\left(ix\sqrt{V_0-\epsilon}\right) + D\exp\left(-ix\sqrt{V_0-\epsilon}\right) && 0 \leq x \leq a \\
\Psi_3 &= E\exp\left(ix\sqrt{\epsilon}\right) && x > a
\end{aligned} \tag{3.17}$$

As before the wave functions and their first derivatives must be continuous at the boundaries of the potential barrier because we are considering a finite potential barrier. We therefore obtain four following boundary conditions :-

$$\begin{aligned}
(a) \qquad 1 + B &= C + D \\
(b) \qquad \sqrt{\epsilon}(1-B) &= (C-D)\sqrt{V_0-\epsilon} \\
(c) \qquad E\exp(ia\sqrt{\epsilon}) &= C\exp(ia\sqrt{V_0-\epsilon}) + D\exp(-ia\sqrt{V_0-\epsilon}) \\
(d) \quad Ei\sqrt{\epsilon}\exp(ia\sqrt{\epsilon}) &= i\sqrt{V_0-\epsilon}\left(C\exp(a\sqrt{V_0-\epsilon}) - D\exp(-a\sqrt{V_0-\epsilon})\right)
\end{aligned} \tag{3.18}$$

By using Equations 3.13 and 3.18 we obtain

$$T = \frac{4\epsilon(V_0-\epsilon)}{4\epsilon(V_0-\epsilon) + V_0^2\sin^2(a\sqrt{V_0-\epsilon})} \quad \epsilon > V_0, \tag{3.19}$$

for the transmission coefficient T and

$$R = \frac{V_0^2\sin^2(a\sqrt{V_0-\epsilon})}{4\epsilon(V_0-\epsilon) + V_0^2\sin^2(a\sqrt{V_0-\epsilon})} \quad \epsilon > V_0, \tag{3.20}$$

for the reflection coeffcient R. This gives us the insight we need when the energy level is greater than the height of the potential barrier. We see that there is an oscillation in the transmission of the electrons through the barrier, a result of the sin term, which is dependent on the width of the barrier. For all values of a that are equal to $\frac{n\pi}{\sqrt{V_0-\epsilon}}$ there is complete transmision of all the electrons and no reflection. At these points it is as if the electrons see no potential barrier at all.

We now apply these results to see how the potential barrier have affected the motion of the electrons in the trilayer. The transmission of the electrons from the ferromagnetic layers is dependent on the thickness of the potential barriers or hybridized adlayers. We therefore conclude that no matter how many hybridized adlayers are deposited onto the substrates the shifted spectral density will oscillate as a function of the number of hybridized adlayers. It is clear we are seeing this effect in Figures 3.3 and 3.4. This will in turn lead to the exchange coupling being dependent on the thickness of the ferromagnetic layers. We conclude that this trial method does not give the correct good approximation to the fully hybridized surface Green's function of a semi-infinite crystal and we reject this method as a possible solution.

This result is particularly interesting. Up until the time when we were deriving this approximation to the surface Green's function it had been assumed that the exchange coupling was roughly independent of the thickness of the ferromagnetic layers, as in Ref [25] for example. Our results gave us the first indication that the exchange coupling may oscillate as a function of the ferromagnetic thickness. The oscillation period being dependent on the perpendicular wave vector in the ferromagnetic layers. For a single-band model we expect two periods to appear in the spectral density, one coming from the up spin Fermi surface and the other from the down spin Fermi surface of the ferromagnetic layers. In this case, the spectral density is a quasi-periodic rather than a periodic function of the ferromagnetic thickness and the usual Fourier analysis is no longer possible. A method for analysing a quasi-

periodic spectral density is discussed in Section 3.3.3 and more details on how this method can be used to calculate the dependence of the exchange coupling on the ferromagnetic thickness can be found in Ref [29].

Method 2

In common with trial method 1 we attempt to obtain a very good approximation to the fully hybridized surface Green's function of a semi-infinite crystal. We do this by building up a very large finite crystal using the two band adlayering procedure of Section 3.1.1. It is hoped that as the finite crystal becomes increasingly large its surface Green's function will tend towards the surface Green's function of the semi-infinite crystal.

We start the procedure by taking a single fully hybridized atomic plane and add a small imaginary part to the energy. Hybridized adlayers are then deposited onto the single atomic plane using the two band adlayering algorithm. In this way we can build the finite crystal up so that it contains as many atomic planes as required.

We now need to demonstrate that this second trial method does give the correct approximation to the surface Green's function of the fully hybridized semi-infinite crystal we seek. When a crystal is semi-infinite depositing an adlayer of the same material as the semi-infinite crystal on top of it will leave us again with just a semi-infinite crystal. Therefore the Green's function of the adlayer will be equal to the surface Green's function of the semi-infinite crystal. We can use this property to test this trial method. As the adlayers are deposited their Green's functions can

be compared with surface Green's function of the finite block on which it has been deposited. The two Green's functions should be equal to another once the finite block is thick enough and its surface Green's function is a very good approximation to the surface Green's of a semi-infinite crystal.

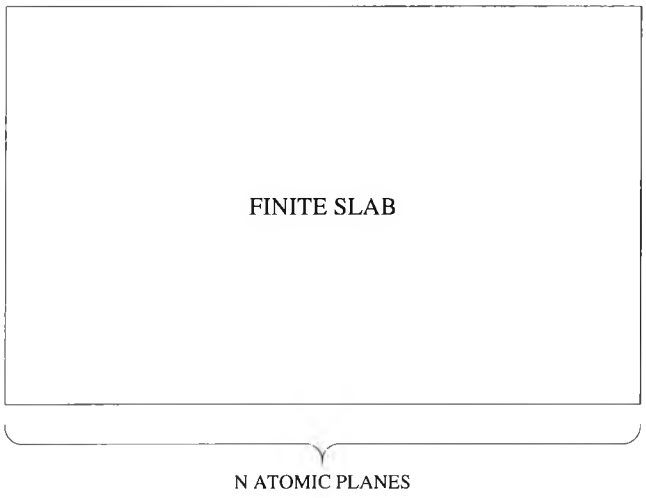

Figure 3.8: Diagram of a finite crystal containing N atomic planes.

It is found that once the finite block is thick enough then its surface Green's function is approximately equal to the surface Green's function of a semi-infinite crystal. The exact thickness of the finite crystal can be determined computationally. Therefore we accept this method. One important thing to note about this trial method is it will only work if a small imaginary part is added to the energy at the beginning of the procedure. This ensures the electrons do not reach the other edge of the finite block thereby simulating the same effect as happens in the semi-infinite crystal. This also implies there is no interference effect from the far edge of the very large finite block.

3.1.3 Joining

To calculate the exchange coupling of a trilayer we need to obtain the Green's function of every atomic plane in the spacer layer that is embedded between two semi-infinite ferromagnetic crystals. To find the Green's function of the n th plane out of N planes in the spacer layer for the two band trilayer we generalize the method as set out in Refs [37], [39] and Section 2.1.3. We start by passing a cleavage plane between the n th and n+1 st atomic plane in the spacer layer. The cleavage plane is again just the mathematical device used to "cut" the trilayer and it effectively separates the structure into two independent crystals, which is shown in Figure 3.9.

The left and right hand sides are now disconnnected so there is no hopping of electrons across the cleavage plane and the Green's functions of the cleaved crystals are therefore given by

$$G^{cl}(m,n) = \begin{cases} G^{Left}(m,n) & \text{if n,m } \epsilon \text{ L} \\ 0 & \text{if n } \epsilon \text{ L,m } \epsilon \text{ R and vice versa} \\ G^{Right}(n,m) & \text{if n,m } \epsilon \text{ R,} \end{cases} \tag{3.21}$$

where G^{cl} are the Green's functions of the system with the cleavage plane, G^{Left} are the Green's functions of the left unconnected crystal and G^{Right} are the Green's functions of the right unconnected crystal. To reconnect the two sides we use Dyson's Equation again. It is

$$G(n,m) = G^{cl}(n,m) + \sum_{p,q} G^{cl}(n,p)W(p,q)G(q,m), \tag{3.22}$$

where G are the Green's functions of the system without the cleavage plane, G^{cl} the Green's functions of the system with the cleavage plane and $W(p,q)$ describes the

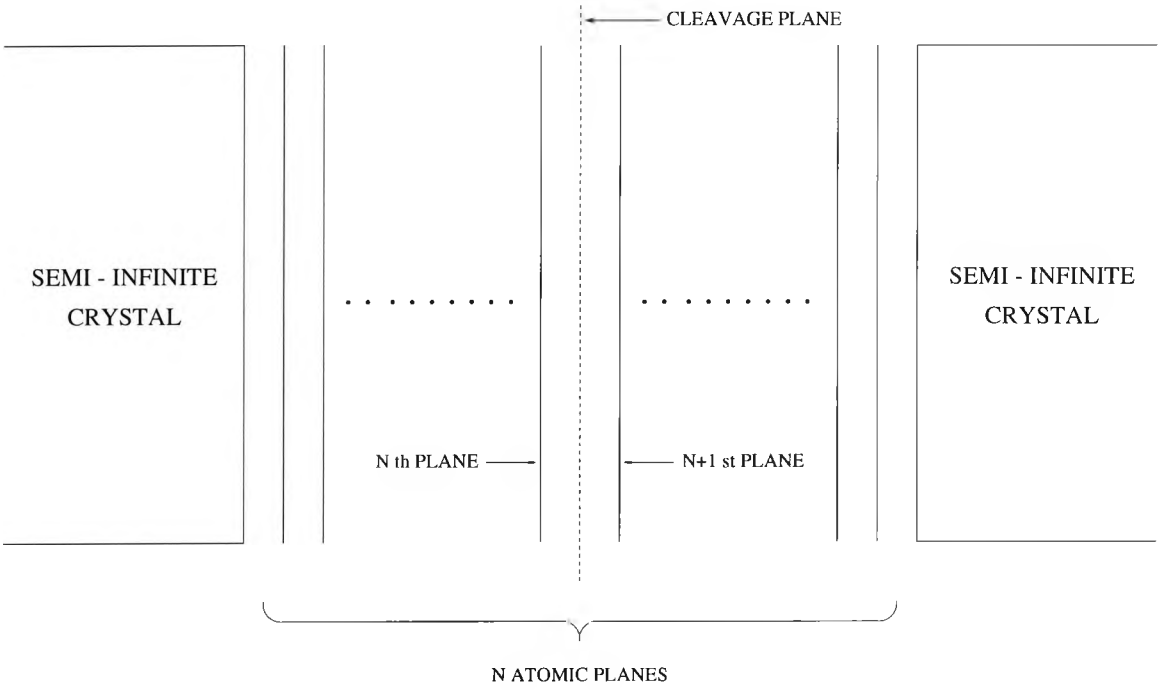

Figure 3.9: Diagram of a trilayer consisting of N atomic planes in the spacer layer sandwiched between two semi-infinite crystals.

perturbation within the system. Here the only non-zero matrix elements describing the perturbation $W(p,q)$ are $W(n,n+1)$ and $W(n+1,n)$.

$$\begin{aligned} W(n,n+1) &= < k_{||}, n \mid W \mid k_{||}, n+1 > = T \qquad \text{and} \\ W(n+1,n) &= < k_{||}, n+1 \mid W \mid k_{||}, n > = T, \end{aligned} \tag{3.23}$$

where $W(n,n+1)$ describes the potential for an electron to hop from the n th atomic plane to the n+1 st plane in the spacer layer and $W(n+1,n)$ the potential for electrons to hop from the n+1 st plane to the n th atomic plane. Finally T is

the hopping integral and it is

$$T = \begin{pmatrix} ts & tsd \\ tsd & td \end{pmatrix},$$

where ts is the potential for electrons to hop from s-band to s-band, td is the potential for electrons to hop from d-band to d-band and tsd is the potential for electrons to from s-band to d-band and vice versa. Using this information and setting $m = n$ in Equation 3.22 we find the solution of the Green's function of the n th atomic plane of the spacer layer in the trilayer to be

$$G(n,n) = G^{cl}(n,n) + G^{cl}(n,n)TG(n+1,n) + G^{cl}(n,n+1)TG(n,n).$$

Using Equation 3.21 we find that

$$G^{cl}(n+1,n) = G^{cl}(n,n+1) = \begin{pmatrix} 0 & 0 \\ 0 & 0 \end{pmatrix}, \tag{3.24}$$

as electrons cannot hop across the cleavage plane. The Green's function of the n th atomic plane of the spacer layer therefore simplifies to

$$G(n,n) = G^{cl}(n,n) + G^{cl}(n,n)TG(n+1,n). \tag{3.25}$$

To complete the solution of Equation 3.25 we need to find $G(n+1,n)$. This is obtained by setting $m = n+1$ in Dyson's equation, Equation 3.22 and taking account of the perturbation within the system. Once these two tasks have been completed we obtain

$$G(n+1,n) = G^{cl}(n+1,n+1)TG(n,n). \tag{3.26}$$

After substituting the answer for $G(n+1,n)$ into Equation 3.25 and simplifying we find that

$$G(n,n) = \left(I - G^{cl}(n,n)TG^{cl}(n+1,n+1)T\right)^{-1} G^{cl}(n,n), \qquad (3.27)$$

where I is the 2×2 identity matrix. Equation 3.27 is the formula for the Green's function of the n th atomic plane of the spacer layer. $G^{cl}(n,n)$ is the surface Green's function of the left unconnected crystal which is made up of n adlayers deposited onto the left semi-infinite crystal. $G^{cl}(n+1,n+1)$ is the surface Green's function of the right unconnected which consists of N-n adlayers deposited on the right semi-infinite crystal. These two Green's functions can therefore be obtained using the two band adlayering procedure which is outlined in Section 3.1.1.

Equation 3.27 is the formula for the Green's function of an arbitrary atomic plane in the spacer layer containing a total of N atomic planes. When computing the exchange coupling we need to take the sum of all the local Green's functions of all the atomic planes in the spacer layer. One great advantage of obtaining these local Green's functions using the adlayering and joining methods is the joining requires little extra computer time over the adlayering. This is because the Green's function of each adlayer is obtained as it is deposited during the adlayering algorithm. These Green's functions can therefore be stored in a local array which can then be accessed as needed to do the joining. The potential time saved is all the more important here than it was for the one band trilayer because all the local Green's functions and parameters are matrices which naturally takes a lot more computational effort to perform even the simplest of mathematical calculations.

One final thing to note about this method of finding the local Green's functions of the trilayer is they have been derived in such a way as to make the generalization to more than two bands trivial.

3.2 Numerical computation of the exchange coupling J(N)

The exchange coupling for a two band trilayer is the same relationship of the thermodynamic potentials we had for a single band trilayer. We recall from Equation 1.33 that this relationship is

$$J(N) = \frac{\left[(\Omega^{\uparrow}(N) + \Omega^{\downarrow}(N))_{FM} - ((\Omega^{\uparrow}(N) + \Omega^{\downarrow}(N))_{AF}\right]}{A}, \tag{3.28}$$

where FM and AF denotes the ferromagnetic and antiferromagnetic configuration of the trilayer respectively, Ω^s is the thermodynamic potential for spin band s at zero temperature and A is the cross-sectional area. Ω^s is

$$\Omega^s(N) = -\frac{1}{\pi}\sum_{k||}\int_{-\infty}^{E_f}\sum_{i=1}^{N}(E - E_f)TrImG_{ii}^{i,s}(E, k_{||}, N)dE, \tag{3.29}$$

were N is the number of atomic planes in the spacer layer and the local Green's functions of the spacer layer are obtained using the method outlined in Section 3.1. As previously we concentrate on how to compute the thermodynamic potential itself as the last step in calculating the exchange coupling is trivial.

There is one important difference between the formula for the thermodynamic potential for the one band trilayer given by Equation 2.23 and the formula for the two band trilayer just above. We saw in the last Section that all the local Green's functions in the two band trilayer are 2×2 matrices. Here we need to take the trace of the local Green's functions in the spacer layer to take this into account. This task did not need to be performed in the one band model because all the local Green's

functions are scalar quantities.

We start the computation of the thermodynamic potential by first considering the energy integral. Once this has been performed we then compute the $k_{||}$ summation.

3.2.1 Complex energy integration

When performing the energy integral for the one band model in Section 2.2.1 we used the method as set out by Zeller el al in Ref [40] to replace the real energy integral with one in the complex energy plane. This step is possible because the general Green's function G(E) possesses singularities along the real axis only and is therefore complex in the whole energy plane except for the real axis. Here in the two band model the singularities of the Green's functions also occur along the real axis only. The Green's functions are therefore analytic functions for the whole complex energy plane except for the real axis. We can therefore apply the same method of computing the real energy integral using the complex energy plane. For the sake of simplicity we use the same contour to perform the integral which was used for the one band model. For the sake of brevity we will not repeat the derivation of the complex energy integral here as the steps taken are the same as in Section 2.2.1. As a reminder the contour we use to perform the complex energy integral is the one shown in Figure 3.10. After performing the complex energy integral we obtain

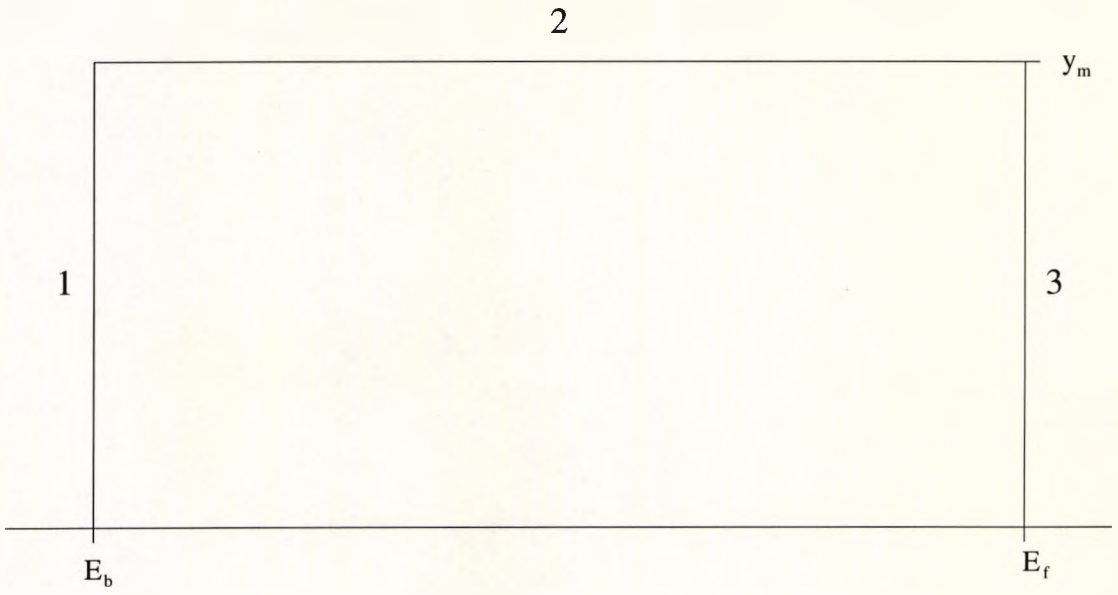

Figure 3.10: Diagram showing the reduced integration contour in the complex energy plane. E_f is the Fermi energy level, E_b is an arbitrary point that lies below the bottom of the energy bands and y_m is a constant that is greater than zero.

$$\begin{aligned}\Omega^s = \; & -\frac{1}{\pi}\sum_{i=1}^{N}\sum_{k||}\int_0^{y_m}(E_b - E_f)TrReG^i_{ii}(E_b + iy, k_{||}, N) \\ & + y(TrImG^i_{ii}(E_f + iy, k_{||}, N) - TrImG^i_{ii}(E_b + iy, k_{||}, N))dy \\ & + \int_{E_b}^{E_f}(x - E_f)TrImG^i_{ii}(x + iy_m, k_{||}, N) + y_m TrReG^i_{ii}(x + iy_m, k_{||}, N)dx.\end{aligned} \tag{3.30}$$

The only difference between this answer and the one obtained for the single band is we need to take the trace of the local Green's functions for the two band model because they are all matrices. Another thing to note about using this contour for the two band trilayer is where we chose our E_b to be. In the one band trilayer it is straightforward to determine exactly where the bottom of the energy band lies

and therefore where E_b should be. The bulk energy bands for the two band trilayer can become slightly shifted because of the effect of hybridization, which is clearly demonstrated in Figure 3.5. When choosing E_b for the two band trilayer the effect hybridization has on the relative position of the bands needs to be taken into account to ensure correct computation of the integral. Finally the formula in Equation 3.30 is as equally valid for trilayers of more than two bands of electrons, as well as for a two band trilayer.

3.2.2 Summation over $k_{||}$

Once the energy integral has been completed we can proceed with the last task in computing Ω^s the summation over $k_{||}$. In the one band model we performed this summation using the prescription as set out by Cunningham in Ref [41]. This method is as equally valid for structures containing more than one band of electrons as it is for a single orbital system. Therefore there is no need to generalize this summation technique here for the two band trilayer. For the sake of brevity we will not go over the process again here as full details are given in Section 2.2.2.

3.3 Analytic computation of the exchange coupling J(N)

The numerical evaluation of the thermodynamic potential Ω^s and therefore the exchange coupling J(N) for the two band trilayer requires a considerable amount of computational time. As we have already seen all the parameters and local Green's functions describing the two band trilayer are matrices. Here even the simplest of mathematical operations such as adding or subtracting need more time to compute. It is therefore obvious the numerical computation of J(N) will take considerably longer for the two band model than it does for the one band model. We conclude from this that although the numerical approach is theoretically possible it is not viable as a practical method. This makes the analytic computation for the two band trilayer more important. We again recall from Equation 1.33 that the exchange coupling is given by

$$J(N) = \frac{\left[(\Omega^{\uparrow}(N) + \Omega^{\downarrow}(N))_{FM} - (\Omega^{\uparrow}(N) + \Omega^{\downarrow}(N))_{AF}\right]}{A}, \tag{3.31}$$

where FM and AF denotes the ferromagnetic and antiferromagnetic configurations of the trilayer respectively and A is the cross-sectional area. The thermodynamic potential Ω^s for spin band s at finite temperature is

$$\Omega^s(N) = -k_B T \int_{-\infty}^{\infty} \ln\left[1 + \exp\left(\frac{\mu - E}{k_B T}\right)\right] D^s(E, N) dE, \tag{3.32}$$

where N is the spacer thickness, T the temperature, μ the chemical potential, k_B is the Boltzmann constant,

$$D^s(E,N) = \sum_{k_\parallel} G^s(E,k_\parallel,N)$$

and finally

$$G^s(E,k_\parallel,N) = -\frac{1}{\pi}\sum_{i=1}^{N} TrImG^s_{ii}(E,k_\parallel,N). \tag{3.33}$$

In accordance with what has already been seen before in this Chapter we need to take the trace of the Green's functions because they are all matrices. Also as before we concentrate on how to compute the thermodynamic potential itself as the last step in computing the exchange coupling is trivial. Here in this Section we replace the prohibitive energy integral and $k_\parallel$ summation with their respective analytic solutions using Refs [33], [34], [42] and Section 2.3. This enables us to compute the exchange coupling in a reasonable time for the two band trilayer.

Before we can proceed with the derivation of the SPA we first need to consider the band structure of the trilayer. Oscillatory exchange coupling occurs when the Fermi energy level intersects a band in the spacer layer. When we considered a single orbital trilayer in the last Chapter, the exchange coupling was found to oscillate with at most one period only because there is only one band of electrons. The Fermi energy level may intersect both the s and d-band for a two band trilayer. If this does occur then the exchange coupling may oscillate with two periods. However if only one band of electrons is partially filled we expect one period only. Due to this possibility we need to consider single-period and double-period exchange coupling

separately. We start by first considering single-period exchange coupling.

3.3.1 Single-period exchange coupling

From a purely mathematical viewpoint it is clear from Equation 3.32 that the term responsible for the oscillatory exchange coupling is $D^s(E,N)$ and we define the average spectral density to be $\frac{1}{N}G^s(E,k_{||},N)$. When only one of the bands is partially filled then the spectral density is periodic in N with one period only. If this is the case then we are able to expand the spectral density in terms of a single Fourier series as in Section 2.3. There we show the spectral density can be Fourier analysed because it fulfills two important criteria ie the discrete spacer thickness N can be mathematically viewed as a continous one and the spectral density is a periodic function in N. The proof that this is the case is given by obtaining an analytic solution for the spectral density which is given in Section 2.4. To rigorously prove the two criteria are satisfied for the two band trilayer would require an analytic solution for the matrix elements of the Green's function for the two band trilayer. As yet we are unable to obtain such an analytic solution. Therefore we must assume that the spectral density does actually fulfill the required conditions to be able Fourier analyse it and all the circumstantial evidence agrees with this assumption. Since the spectral density is periodic with one period only we can use the same Fourier series expansion that was used in the one band model and it is

$$\frac{1}{N}G^s(E,k_{||},N) = Re\sum_{n=1}^{\infty} C_n^s\left(E,k_{||}\right)\exp\left(2iNan\beta(E,k_{||})\right). \qquad (3.34)$$

Here $ReC_n^s\left(E,k_{||}\right)$ is the usual Fourier coefficient a_n and $-ImC_n^s\left(E,k_{||}\right)$ is the usual Fourier coefficient b_n. Our working hypothesis is that, by analogy with the single orbital trilayer, $\beta(E,k_{||})$ is the wave vector of the bulk spacer metal, which is perpendicular to the atomic planes and is related to the period of oscillations by $\dfrac{\pi}{\beta(E,k_{||})}$. Replacing $G^s(E,k_{||},N)$ in Equation 3.32 by its Fourier series expansion we obtain

$$\begin{aligned}\Omega^s(N) = & -\frac{k_BTNA}{4\pi^2}Re\sum_{n=1}^{\infty}\int_{-\infty}^{\infty}\int_{-\infty}^{\infty}\int_{-\infty}^{\infty}\ln\left[1+\exp\left(\frac{\mu-E}{k_BT}\right)\right]\times \\ & C_n^s(E,k_{||})\exp\left(2iNan\beta(E,k_{||})\right)dk_xdk_ydE,\end{aligned} \tag{3.35}$$

where the summation over $k_{||}$ has been converted into two integrals one with respect to k_x and the other with respect to k_y.

Equation 3.35 is exactly the same formula we obtained after we replaced the spectral density by its Fourier series expansion for the one band trilayer which is given by Equation 2.38. Applying all the same techniques as is used in Section 2.3 we eventually obtain the same formula for Ω^s. For the sake of brevity the derivation of the formula is not repeated here. We recall from Equation 2.49 the answer is

$$\begin{aligned}\Omega^s(N) = & \frac{A}{16a^3N^2\pi}Re\sum_{n=1}^{\infty}\frac{\sigma}{n^3}\left(\frac{\partial E}{\partial\beta}\right)^2 C_n^s(E_f,k_{||}^0)\left|\frac{\partial^2\beta}{\partial k_x^2}\frac{\partial^2\beta}{\partial k_y^2}\right|^{-1/2} \\ & \times\exp\left(2iNan\beta(E_f,k_{||}^0)\right),\end{aligned} \tag{3.36}$$

where

$$\sigma = \begin{cases} e^{i\pi/2} & \text{if } \dfrac{\partial^2\beta}{\partial k_x^2} \text{ and } \dfrac{\partial^2\beta}{\partial k_y^2} > 0 \\ e^{-i\pi/2} & \text{if } \dfrac{\partial^2\beta}{\partial k_x^2} \text{ and } \dfrac{\partial^2\beta}{\partial k_y^2} < 0 \\ 1 & \text{if } \dfrac{\partial^2\beta}{\partial k_x^2} > 0 \text{ and } \dfrac{\partial^2\beta}{\partial k_y^2} < 0 \text{ and vice versa.} \end{cases}$$

3.3.2 Application of the SPA for single-period exchange coupling

Now the formula for the thermodynamic potential has been derived using the SPA, the next step is to apply this formula to a two orbital trilayer and compute all the unknown factors in Equation 3.36.

We start by setting the perpendicular wavevector $k_z(E, k_{||})$ equal to $\beta(E, k_{||})$ in the bulk tight-binding energy bands of the spacer layer. The bulk energy bands of the spacer layer are computed by solving the following matrix equation

$$\begin{vmatrix} E_s + 2ts\epsilon(\vec{k}) - E & 2tsd\epsilon(\vec{k}) \\ 2tsd\epsilon(\vec{k}) & E_d + 2td\epsilon(\vec{k}) - E \end{vmatrix} = 0. \tag{3.37}$$

Here E_s and E_d are the atomic potentials of the s and d bands of the spacer layer respectively. ts is the hopping integral of the s-band of the spacer layer, td the hopping integral of the d-band and tsd is the hybridization between the bands. Finally $\epsilon(\vec{k}) = \cos(ak_x) + \cos(ak_y) + \cos(a\beta)$, where a is the inter-atomic distance. All the factors in Equation 3.36 are obtained by solving Equation 3.37 and the resulting characteristic equation is

$$E^2 - E\left(E_s + E_d + 2(ts + td)\epsilon(\vec{k})\right) + (E_s + 2ts\epsilon(\vec{k}))(E_d + 2td\epsilon(\vec{k})) - 4tsd^2\epsilon^2(\vec{k}) = 0. \tag{3.38}$$

The first task we need to complete before we can proceed with the application of the SPA to a two orbital trilayer is to locate all the possible stationary points. The general stationary point $k_{||}^0$ is obtained by finding the values of $k_{||}$ where $\dfrac{\partial\beta}{\partial k_y}$ and

$\frac{\partial \beta}{\partial k_y}$ are equal to zero. By solving Equation 3.38 for E and differentiating it once with respect to k_x and then k_y we obtain

$$\frac{\partial E}{\partial k_x} = \frac{\partial \epsilon(\vec{k})}{\partial k_x} \left\{ ts + td \pm \frac{xy + 2\epsilon(\vec{k})(y^2 + 4tsd^2)}{\sqrt{x^2 + 4xy\epsilon(\vec{k}) + 4\epsilon^2(\vec{k})(y^2 + 4tsd^2)}} \right\} \tag{3.39}$$

and

$$\frac{\partial E}{\partial k_y} = \frac{\partial \epsilon(\vec{k})}{\partial k_y} \left\{ ts + td \pm \frac{xy + 2\epsilon(\vec{k})(y^2 + 4tsd^2)}{\sqrt{x^2 + 4xy\epsilon(\vec{k}) + 4\epsilon^2(\vec{k})(y^2 + 4tsd^2)}} \right\}, \tag{3.40}$$

where $x = E_s - E_d$ and $y = t_s - t_d$. Since $\frac{\partial E}{\partial k_x}$ and $\frac{\partial E}{\partial k_y}$ are equal to zero and by using Equations 3.39 and 3.40 we find all the possible stationary points are

$$(0,0),\ (0, \pm\frac{\pi}{a}),\ (\pm\frac{\pi}{a}, 0),\ (\pm\frac{\pi}{a}, \pm\frac{\pi}{a})$$

and the values of k_x and k_y where

$$\left\{ ts + td \pm \frac{xy + 2\epsilon(\vec{k})(y^2 + 4tsd^2)}{\sqrt{x^2 + 4xy\epsilon(\vec{k}) + 4\epsilon^2(\vec{k})(y^2 + 4tsd^2)}} \right\} = 0.$$

The choice of which branch to take in the equation just above and all future equations for this subsection is determined by the band structure and in particular which band is intersected by the Fermi energy level in the spacer layer. Next we obtain $\beta(E_f, k_{||}^0)$. $\beta(E_f, k_{||}^0)$ is simply obtained be setting $E = E_f$ and $k_{||} = k_{||}^0$ in Equation 3.38 and solving it to find that

$$\beta(E_f, k_{||}^0) = \frac{1}{a} \arccos \left\{ \frac{-s \pm \sqrt{s^2 - 4rt}}{2r} - \cos(ak_x^0) - \cos(ak_y^0) \right\}, \tag{3.41}$$

where $r = 4(tstd - tsd^2)$, $s = 2(ts(E_d - E_f) + td(E_s - E_f))$ and $t = (E_s - E_f)(E_d - E_f)$. The choice of which branch to take in Equation 3.41 is determined by the

band structure of the spacer layer. Now we compute $\frac{\partial E}{\partial \beta}$. $\frac{\partial E}{\partial \beta}$ is simply found by differentiating the solution of E once with respect to β. Once this has been performed we find that

$$\frac{\partial E}{\partial \beta} = -a\sin(a\beta(E,k_{||}))\left\{ts + td \pm \frac{xy + 2\epsilon(\vec{k})(y^2+4tsd^2)}{\sqrt{x^2+4xy\epsilon(\vec{k})+4\epsilon^2(\vec{k})(y^2+4tsd^2)}}\right\}. \quad (3.42)$$

Now we obtain $\frac{\partial^2\beta}{\partial k_x^2}$ and $\frac{\partial^2\beta}{\partial k_y^2}$, but first we calculate $\frac{\partial^2\beta}{\partial k_x^2}$. Using the property that $\frac{\partial E}{\partial k_x}$ is equal to zero, we differentiate the right hand side of Equation 3.39 again with respect to k_x and simplify to find that

$$\frac{\partial^2\beta}{\partial k_x^2} = -\frac{a\cos(ak_x)}{\sin(a\beta(E,k_{||}))}. \quad (3.43)$$

After performing a similar process for $\frac{\partial^2\beta}{\partial k_y^2}$ we obtain

$$\frac{\partial^2\beta}{\partial k_y^2} = -\frac{a\cos(ak_y)}{\sin(a\beta(E,k_{||}))}. \quad (3.44)$$

Now we have found the factors $\frac{\partial E}{\partial \beta}$, $\frac{\partial^2\beta}{\partial k_x^2}$ and $\frac{\partial^2\beta}{\partial k_y^2}$ it is trivial to take their values at the point $E = E_f$ and $k_{||} = k_{||}^0$. We can then also calculate the factor σ. All that remains is to compute the Fourier coefficients $C_n^s(E_f, k_{||}^0)$. Since we are considering single-period exchange coupling here the spectral density is a periodic function in N with a single period only. Therefore we can employ the shifting method here to the two orbital trilayer to compute the Fourier coefficients. Since we have already outlined this process the reader is referred to Section 2.3.3 for the full details of the shifting method to obtain the Fourier coefficients.

3.3.3 Double-period exchange coupling

Now we consider the situation when the oscillatory exchange coupling has two periods, which occurs when two bands in the spacer intersect the Fermi surface. For each $k_{||}$ we therefore have two perpendicular wave vectors $k_{\perp}^{a}$, $k_{\perp}^{b}$ obtained by solving the bulk dispersion $E = E(k_{||}, k_{\perp})$ in the spacer. Guided by our results for the single-orbital model, we expect that the average spectral density (per atomic plane) to depend on the spacer thickness only via the products $k_{\perp}^{a}Na$ and $k_{\perp}^{b}Na$. Since in general $\frac{\pi}{k_{\perp}^{a}}$ and $\frac{\pi}{k_{\perp}^{b}}$ are incommensurate, it is clear that the average spectral density is no longer a periodic function of N. This is a serious problem since our analytic approach is based on a Fourier series expansion of the spectral density. To resolve this problem, consider two independent bands. Our analytic formula for the spectral density, Equation 2.84, can be trivially generalized to this situation and it is clear that the average spectral density is now a function of two periodic functions of N, one of them having the period $\frac{\pi}{k_{\perp}^{a}}$ and the other $\frac{\pi}{k_{\perp}^{b}}$. Such a function is called a quasi-periodic function and can be expanded in terms of trigonometric functions using the following trick. We replace the true spacer thickness N by two fictitious ones N and M, so that N appears in the factor $k_{\perp}^{a}N$ and M in the other factor $k_{\perp}^{b}M$. The spectral density $\overline{G}^{s}(E, k_{||}, N, M)$ for such a fictitious system, regarded as a function of two independent variables N and M, is a periodic function in N and M and can therefore be expanded in terms of a double Fourier series.

$$\frac{1}{N}\overline{G}^{s}(E, k_{||}, N, M) = \sum_{n,m=1}^{\infty} a_{nm} \cos\left(\frac{2n\pi N}{K} + \frac{2m\pi M}{L}\right) + b_{nm} \sin\left(\frac{2n\pi N}{K} + \frac{2m\pi M}{L}\right), \tag{3.45}$$

where K is the period $\frac{\pi}{\beta^a(E,k_{||})}$ and L is the period $\frac{\pi}{\beta^b(E,k_{||})}$. As with the single-period exchange coupling our working hypothesis is that β^a and β^b are the wave vectors of the bulk spacer metal. The physical spectral density is given by $G^s(E,k_{||},N) = \overline{G}^s(E,k_{||},N,M)$ and its expansion takes the complex form of

$$\frac{1}{N}G^s(E,k_{||},N) = Re\sum_{n,m=1}^{\infty} C^s_{nm}\exp\left(2iNa(m\beta^a(E,k_{||}) + n\beta^b(E,k_{||}))\right). \qquad (3.46)$$

Here ReC^s_{nm} is the Fourier coefficient a_{nm} given in Equation 3.45 and $-ImC^s_{nm}$ is the Fourier coefficient b_{nm}. After substituting the complex Fourier series expansion into the formula for the thermodynamic potential given by Equation 3.32 we find that

$$\begin{aligned}\Omega^s(N) &= -\frac{k_BTNA}{4\pi^2}\int_{-\infty}^{\infty}\int_{-\infty}^{\infty}\int_{-\infty}^{\infty}\ln\left[1+\exp\left(\frac{\mu-E}{k_BT}\right)\right]C^s_{nm}(E,k_{||})\times \\ &\quad \exp\left(2iNa(m\beta^a(E,k_{||}) + n\beta^b(E,k_{||}))\right)dk_xdk_ydE,\end{aligned} \qquad (3.47)$$

where the summation over $k_{||}$ has been converted into a double integral one with respect to k_x and the other with respect to k_y.

The procedure we have described can be easily implemented for two independent bands when we have an analytic expression for the spectral density. In the most general case of two hybridized bands we do not have such an analytic formula but our procedure is still applicable provided the average spectral density is a quasi-periodic function. The evaluation of the Fourier coefficients C^s_{nm} in Equation 3.46 in the most general case of two hybridized bands and is described in Section 3.3.6.

3.3.4 k_x and k_x integrals

We proceed with the derivation of the SPA by first making the substitution $\phi(m,n,E,k_{||}) = m\beta^a(E,k_{||}) + n\beta^b(E,k_{||})$ to simplify the calculations. Once this has been made we are left with

$$\begin{aligned}\Omega^s(N) &= -\frac{k_BTNA}{4\pi^2}Re\sum_{n,m}^{\infty}\int_{-\infty}^{\infty}\int_{-\infty}^{\infty}\int_{-\infty}^{\infty}\ln\left[1+\exp\left(\frac{\mu-E}{k_BT}\right)\right]C^s_{nm}(E,k_{||}) \\ &\quad\times\exp\left(2iNa\phi(m,n,E,k_{||})\right)dk_xdk_ydE.\end{aligned} \tag{3.48}$$

Here the exponential factor $\exp\left(2iNa\phi(m,n,E,k_{||})\right)$ again oscillates rapidly as a function of $k_{||}$ for large values of N ie large spacer thicknesses. As the rapid oscillations tend to cancel each other out when performing the integrals the dominant contribution to the integral comes from around the region where k_x and k_y are in the region of a stationary point denoted by $k^0_{||} = (k^0_x, k^0_y)$. We approximate $\phi(m,n,E,k_{||})$ by expanding it in terms of a Taylor series about the stationary point $k^0_{||}$ up to second order. The Taylor series expansion of $\phi(m,n,E,k_{||})$ is

$$\begin{aligned}\phi(E,k_{||}) &\simeq \phi(E,k^0_{||}) + \left\{\frac{\partial\phi}{\partial k_x}(k_x-k^0_x) + \frac{\partial\phi}{\partial k_y}(k_y-k^0_y)\right\} + \\ &\quad\frac{1}{2}\left\{\frac{\partial^2\phi}{\partial k_x^2}(k_x-k^0_x)^2 + 2\frac{\partial^2\phi}{\partial k_x\partial k_y}(k_x-k^0_x)(k_y-k^0_y) + \frac{\partial^2\phi}{\partial k_y^2}(k_y-k^0_y)^2\right\},\end{aligned}$$

which reduces to

$$\phi(m,n,E,k_{||}) \simeq \phi(m,n,E,k^0_{||}) + \frac{1}{2}\left\{\frac{\partial^2\phi}{\partial k_x^2}(k_x-k^0_x)^2 + \frac{\partial^2\phi}{\partial k_y^2}(k_y-k^0_y)^2\right\} \tag{3.49}$$

after simplifying. The first simplification of $\dfrac{\partial\phi}{\partial k_x} = \dfrac{\partial\phi}{\partial k_y} = 0$ is obvious. The second simplification of $\dfrac{\partial^2\phi}{\partial k_x\partial k_y} = 0$ comes about because there is naturally no mixed derivative for the simple cubic lattice structure, which is the crystal structure we

are considering. Even if the mixed derivative were non-zero this second simplification can always be achieved by reducing the quadratic form to its corresponding diagonal form by effectively rotating the (k_x, k_y) axis. Finally the Fourier coefficients $C^s_{nm}(E, k_{||})$ are approximated by taking their values at $k^0_{||}$. Substituting the simplified Taylor's series expansion into Equation 3.48 we obtain

$$\begin{aligned}\Omega^s &= -\frac{k_B T N A}{4\pi^2} Re \sum_{n,m=1}^{\infty} \int_{-\infty}^{\infty} ln\left[1 + \exp\left(\frac{\mu - E}{k_B T}\right)\right] C^s_{nm}(E, k^0_{||}) \exp(2iNa\phi) \\ &\times \int_{-\infty}^{\infty}\int_{-\infty}^{\infty} \exp\left(iNa\left(\frac{\partial^2\phi}{\partial k_x^2}(k_x - k_x^0)^2 + \frac{\partial^2\phi}{\partial k_y^2}(k_y - k_y^0)^2\right)\right) dk_x dk_y dE. \end{aligned} \tag{3.50}$$

Let us first consider the k_x integral only. If we let $y = k_x - k_x^0$ then

$$\int_{-\infty}^{\infty} \exp\left(iNa\left(\frac{\partial^2\phi}{\partial k_x^2}(k_x - k_x^0)^2\right)\right) dk_x = \int_{-\infty}^{\infty} \exp\left(iNay^2\frac{\partial^2\phi}{\partial k_x^2}\right) dy. \tag{3.51}$$

If the factor $\dfrac{\partial^2\phi}{\partial k_x^2} > 0$ then let $y = z\exp\left(\dfrac{i\pi}{4}\right)$. This substitution for y in the k_x integral leads to the integral being put in a form similar to the standard Gaussian integral and gives us an answer of

$$\int_{-\infty}^{\infty} \exp\left(iNa\left(\frac{\partial^2\phi}{\partial k_x^2}(k_x - k_x^0)^2\right)\right) dk_x = \exp\left(\frac{i\pi}{4}\right)\sqrt{\frac{\pi}{Na\frac{\partial^2\phi}{\partial k_x^2}}}. \tag{3.52}$$

If on the other hand the factor $\dfrac{\partial^2\phi}{\partial k_x^2} < 0$ then let $y = z\exp\left(-\dfrac{i\pi}{4}\right)$, which gives us

$$\int_{-\infty}^{\infty} \exp\left(iNa\left(\frac{\partial^2\phi}{\partial k_x^2}(k_x - k_x^0)^2\right)\right) dk_x = \exp\left(-\frac{i\pi}{4}\right)\sqrt{\frac{\pi}{Na\frac{\partial^2\phi}{\partial k_x^2}}}. \tag{3.53}$$

It can easily be seen that this method of evaluating the k_x integral can also be applied to the k_y integral in exactly the same way. Once these two integrals have

been performed we are left with

$$\begin{aligned}\Omega^s &= -\frac{k_BTA}{4a\pi}Re\sum_{n,m=1}^{\infty}\sigma\int_{-\infty}^{\infty}ln\left[1+\exp\left(\frac{\mu-E}{k_BT}\right)\right]C^s_{nm}(E,k^0_{||})\times \\ &\quad \exp\left(2iNa\phi(n,m,E,k^0_{||})\right)\left|\frac{\partial^2\phi}{\partial k_x^2}\frac{\partial^2\phi}{\partial k_y^2}\right|^{-1/2}dE,\end{aligned} \tag{3.54}$$

where

$$\sigma=\begin{cases} e^{i\pi/2} & \text{if } \dfrac{\partial^2\phi}{\partial k_x^2} \text{ and } \dfrac{\partial^2\phi}{\partial k_y^2}>0 \\ e^{-i\pi/2} & \text{if } \dfrac{\partial^2\phi}{\partial k_x^2} \text{ and } \dfrac{\partial^2\phi}{\partial k_y^2}<0 \\ 1 & \text{if } \dfrac{\partial^2\phi}{\partial k_x^2}>0 \text{ and } \dfrac{\partial^2\phi}{\partial k_y^2}<0 \text{ or vice versa.}\end{cases}$$

3.3.5 Energy integration

We can now proceed with evaluating the energy integral. We start by noting for larger spacer thicknesses the factors $C^s_{nm}(E,k_{||})$, $\frac{\partial^2\phi}{\partial k_x^2}$ and $\frac{\partial^2\phi}{\partial k_y^2}$ only weakly depend on E when compared to the exponential factor. Taking this into account the formula for Ω^s therefore simplifies to

$$\begin{aligned}\Omega^s &= -\frac{k_BTA}{4a\pi}Re\sum_{n,m=1}^{\infty}\sigma C^s_{nm}(E,k^0_{||})\left|\frac{\partial^2\phi}{\partial k_x^2}\frac{\partial^2\phi}{\partial k_y^2}\right|^{-1/2}\times \\ &\quad \int_{-\infty}^{\infty}ln\left[1+\exp\left(\frac{\mu-E}{k_BT}\right)\right]\exp\left(2iNa\phi(n,m,E,k^0_{||})\right)dE\end{aligned} \tag{3.55}$$

which enables us to evaluate the energy integral by parts after letting

$$U=ln\left[1+\exp\left(\frac{\mu-E}{k_BT}\right)\right]$$

and

$$\begin{aligned}\frac{\partial V}{\partial E} &= \exp\left(2iNa\phi(n,m,E,k^0_{||})\right) \\ \Rightarrow\ V &= \int\exp\left(2iNa\phi(n,m,E,k^0_{||})\right)\left(\frac{\partial E}{\partial\phi}\right)\left(\frac{\partial\phi}{\partial E}\right)dE \\ V &= \frac{\partial E}{\partial\phi}\left(\frac{\exp(2iNa\phi(m,n,E,k^0_{||}))}{2iNa}\right).\end{aligned}$$

We also note that $\frac{\partial E}{\partial \phi}$ also only weakly depends on E as well. After integrating Equation 3.55 by parts once we obtain

$$\begin{aligned}\Omega^s &= -\frac{A}{8a^2\pi N} Re \sum_{n,m=1}^{\infty} \frac{\sigma}{i} C^s_{nm}(E, k^0_{||}) \left| \frac{\partial^2\phi}{\partial k_x^2} \frac{\partial^2\phi}{\partial k_y^2} \right|^{-1/2} \frac{\partial E}{\partial \phi} \times \\ &\int_{-\infty}^{\infty} \frac{\exp(2iNa\phi(n, m, E, k^0_{||})}{1 + \exp\left(\frac{\mu - E}{k_B T}\right)} dE.\end{aligned} \tag{3.56}$$

To complete the integral we again look at the exponential factor. Much the same as before this is a rapidly oscillating factor which oscillates this time as a function of E for large spacer thicknesses. These will therefore lead to a lot of calculations when performing the integral. However this time the dominant contribution to the integral comes from around the Fermi level because there is a discrete upper limit in the integral. The dominant contribution will come from the beginning of the last oscillation upto the Fermi energy level. We therefore approximate the exponential factor by expanding ϕ in terms of a Taylor series about the Fermi level up to the first order this time. As the dominant contribution comes from around the Fermi level we approximate all the factors that only weakly depend on E by taking their values at $E = \mu$. The Taylor series expansion of ϕ up to the first order is

$$\phi(n, m, E, k^0_{||}) \simeq \phi(n, m, \mu, k^0_{||}) + \frac{\partial \phi}{\partial E}(E - \mu).$$

Putting this Taylor series expansion into the formula for the thermodynamic potential we obtain

$$\begin{aligned}\Omega^s &= -\frac{A}{8a^2\pi N} Re \sum_{n,m=1}^{\infty} \frac{\sigma}{i} C^s_{nm}(\mu, k^0_{||}) \left| \frac{\partial^2\phi}{\partial k_x^2} \frac{\partial^2\phi}{\partial k_y^2} \right|^{-1/2} \frac{\partial E}{\partial \phi} \times \\ &\exp(2iNa\phi(n, m, \mu, k^0_{||})) \int_{-\infty}^{\infty} \frac{\exp(2iNa\frac{\partial\phi}{\partial E}(E - \mu))}{1 + \exp\left(\frac{\mu - E}{k_B T}\right)} dE.\end{aligned} \tag{3.57}$$

If we let $\frac{\mu - E}{k_B T} = x$ then it leads to the integral being put in the form of another standard integral

$$\int_{-\infty}^{\infty} \frac{\exp(2iNa\frac{\partial\phi}{\partial E}(E-\mu))}{1+\exp\left(\frac{\mu-E}{k_BT}\right)}dE = -k_BT\int_{-\infty}^{\infty}\frac{\exp(-2iNak_BTx\frac{\partial\phi}{\partial E})}{1+\exp(x)}dx$$

which gives the following solution

$$= \frac{ik_BT\pi}{\sinh\left(-2\frac{\partial\phi}{\partial E}k_BTNa\pi\right)}.$$

Replacing the energy integral by its solution given above we obtain

$$\begin{aligned}\Omega^s &= -\frac{k_BTA}{8a^2N}Re\sum_{n,m=1}^{\infty}\sigma C^s_{nm}(\mu,k_{\|})\left|\frac{\partial^2\phi}{\partial k_x^2}\frac{\partial^2\phi}{\partial k_y^2}\right|^{-1/2}\frac{\partial E}{\partial\phi}\times \\ &\quad \frac{\exp(2iNa\phi(m,n,\mu,k^0_{\|}))}{\sinh\left(-2k_BTNa\pi\frac{\partial\phi}{\partial E}\right)}.\end{aligned} \tag{3.58}$$

All that remains for us to do to be able to compare the results from the SPA with the numerical results is to let $T \to 0$. Letting $T \to 0$ we see that

$$\sinh\left(-2k_BTNa\pi\frac{\partial\phi}{\partial E}\right) \to -2k_BTNa\pi\frac{\partial\phi}{\partial E}$$

and $\mu \to E_f$. Therefore Ω^s becomes

$$\begin{aligned}\Omega^s &= \frac{A}{16a^3\pi N^2}Re\sum_{n,m=1}^{\infty}\sigma C^s_{nm}(E_f,k_{\|})\exp\left(2iNa\phi(m,n,E_f,k^0_{\|})\right)\times \\ &\quad \left(\frac{\partial E}{\partial\phi}\right)^2\left|\frac{\partial^2\phi}{\partial k_x^2}\frac{\partial^2\phi}{\partial k_y^2}\right|^{-1/2},\end{aligned} \tag{3.59}$$

where $\phi(m,n,E_f,k^0_{\|}) = m\beta^a(E_f,k^0_{\|}) + n\beta^b(E_f,k^0_{\|})$ and

$$\sigma = \begin{cases} e^{i\pi/2} & \text{if } \dfrac{\partial^2\phi}{\partial k_x^2} \text{ and } \dfrac{\partial^2\phi}{\partial k_y^2} > 0 \\ e^{-i\pi/2} & \text{if } \dfrac{\partial^2\phi}{\partial k_x^2} \text{ and } \dfrac{\partial^2\phi}{\partial k_y^2} < 0 \\ 1 & \text{if } \dfrac{\partial^2\phi}{\partial k_x^2} > 0 \text{ and } \dfrac{\partial^2\phi}{\partial k_y^2} < 0 \text{ or vice versa.} \end{cases}$$

Now we compute all the as yet unknown factors.

3.3.6 Application of the SPA for double-period exchange coupling

Now we apply the formula for the thermodynamic potential given by Equation 3.59 to a two orbital trilayer where the oscillatory exchange coupling has two periods. First we need to locate all the possible stationary points $k_{||}^0$ and compute $\beta^a(E_f, k_{||}^0)$ and $\beta^b(E_f, k_{||}^0)$. The method used to compute $k_{||}^0$ when the exchange coupling has only one period is as equally valid here when the exchange coupling has two periods. Therefore for the sake of brevity the reader is referred to Section 3.3.2 for the method of computing all the possible stationary points $k_{||}^0$. Now we obtain $\beta^a(E_f, k_{||}^0)$ and $\beta^b(E_f, k_{||}^0)$. In common with the stationary points the method used to compute β^a and β^b is the same here as it was for single-period exchange coupling, which is given by Equation 3.41. Previously the band structure determined which branch of the solution of β should be taken. Since the Fermi level intersects both bands for double-period exchange coupling we take both branches of the solution to obtain $\beta^a(E_f, k_{||}^0)$ and $\beta^b(E_f, k_{||}^0)$. Now we obtain $\dfrac{\partial E}{\partial \phi}$. By differentiating ϕ once with respect E we obtain

$$\frac{\partial \phi}{\partial E} = m\frac{\partial \beta^a}{\partial E} + n\frac{\partial \beta^b}{\partial E},$$

therefore

$$\frac{\partial E}{\partial \phi} = \frac{1}{m\frac{\partial \beta^a}{\partial E} + n\frac{\partial \beta^b}{\partial E}}, \tag{3.60}$$

where $\frac{\partial \beta^a}{\partial E}$ and $\frac{\partial \beta^b}{\partial E}$ are computed by using Equation 3.42. By differentiating ϕ twice with respect to k_x we find that

$$\frac{\partial^2 \phi}{\partial k_x^2} = m\frac{\partial^2 \beta^a}{\partial k_x^2} + n\frac{\partial^2 \beta^b}{\partial k_x^2}, \tag{3.61}$$

where $\frac{\partial^2 \beta^a}{\partial k_x^2}$ and $\frac{\partial^2 \beta^b}{\partial k_x^2}$ are computed using Equation 3.43. Similarly

$$\frac{\partial^2 \beta}{\partial k_y^2} = m\frac{\partial^2 \beta^a}{\partial k_y^2} + n\frac{\partial^2 \beta^b}{\partial k_y^2}, \tag{3.62}$$

where $\frac{\partial^2 \beta^a}{\partial k_y^2}$ and $\frac{\partial^2 \beta^b}{\partial k_y^2}$ are computed using Equation 3.44. We now have all the information to calculate the factor σ and all that remains for us to compute is the Fourier coefficients $C^s_{nm}(E_f, k^0_{||})$. Since we are considering double-period exchange coupling here we cannot use the shifting method to obtain the Fourier coefficients. This is because the average spectral density is no longer a periodic function of N. Instead we use a fitting procedure to obtain the Fourier coefficients. It should be noted that this procedure can also be used to obtain the Fourier coefficients for the spectral density when it is periodic function in N with a single period.

We first take a sample of the spectral density and as before we usually take the spacer thickness to be between 500 and 600 atomic planes as the spectral density behaves asymptotically like a quasi-periodic function for larger spacer thicknesses. Now we call the sample of the spectral density $g(x_k)$ say, where there are a total of N data points. We wish to fit a continuous function $f(x)$ to the sample of the spectral density which can be represented by a Fourier like series as in Equation 3.46. The

best bit to the data occurs when

$$\sum_{k=1}^{N} |f(x_k) - g(x_k)|^2 \tag{3.63}$$

is a minimum. If we rewrite $f(x)$ as

$$f(x_k) = \sum_{\alpha}^{R} C_\alpha \phi_\alpha(x_k), \tag{3.64}$$

where C_α represents the Fourier coefficients $C^s_{nm}(E_f, k^0_{||})$ and $\phi_\alpha(x_k)$ the exponentials $\exp(2ix_k(m\beta^a + n\beta^b))$ then we obtain

$$\sum_{k=1}^{N} \left| \sum_{\alpha}^{R} C_\alpha \phi_\alpha(x_k) - g(x_k) \right|^2 \tag{3.65}$$

for the function that needs to be minimised. We can express all the terms in Equation 3.65 in terms of matrices. Let G_{N1} be a N$\times$1 matrix containing the $g(x_k)$'s, $C_{\alpha 1}$ a $\alpha\times$1 matrix containing the C_α's and $\Phi_{N\alpha}$ be a N$\times\alpha$ matrix containing the $\phi_\alpha(x_k)$'s. Equation 3.65 therefore becomes

$$\Phi_{N\alpha} C_{\alpha 1} - G_{N1}. \tag{3.66}$$

Once the problem has been rewritten in terms of matrices, as just above, one can see the best fit of the Fourier series to the spectral density occurs when the sum of the squares of the matrix elements in the resultant vector is minimised. This is best determined computationally. A unique solution for the matrix elements of $C_{\alpha 1}$ can therefore be found using Equation 3.66 provided N is either greater than or equal to R.

To help visualise what the matrices in Equation 3.66 actually look like let us consider a general example when the summation indices in the Fourier series run

from 0 to 1 for both n and m.

$$G_{N1} = \begin{pmatrix} g(x_1) \\ g(x_2) \\ . \\ . \\ g(x_N) \end{pmatrix}, \tag{3.67}$$

$$C_{\alpha 1} = \begin{pmatrix} C_{00} \\ C_{01} \\ C_{10} \\ C_{11} \end{pmatrix}, \tag{3.68}$$

and

$$\Phi_{N\alpha} = \begin{pmatrix} 1 & \exp(2ix_1 + \beta^a) & \exp(2ix_1\beta^b) & \exp(2ix_1(\beta^a + \beta^b) \\ 1 & \exp(2ix_2 + \beta^a) & \exp(2ix_2\beta^b) & \exp(2ix_2(\beta^a + \beta^b) \\ . & & & . \\ . & & & . \\ 1 & \exp(2ix_N + \beta^a) & \exp(2ix_N\beta^b) & \exp(2ix_N(\beta^a + \beta^b) \end{pmatrix}. \tag{3.69}$$

3.4 Results for the two band trilayer

The aim of this section is to investigate what effect hybridization has on the exchange coupling for a two orbital trilayer. We start in Section 3.4.1 by explaining how the results presented in this section have been computed. In Section 3.4.2 we first consider a two orbital trilayer where there is no hybridization between the bands in the spacer layer only. Electrons are free to hop from band to band in the semi-infinite ferromagnetic layers. In Section 3.4.3 we investigate what effect the hybridization in the spacer layer has on the exchange coupling. Once this has been completed we look at what effect the hybridization in the ferromagnetic layers has on the exchange coupling in Section 3.4.4. Finally in Section 3.4.5 we look at a single example of exchange coupling for a two orbital trilayer when there are two periods of oscillations.

3.4.1 Method of computation

Computing the exchange coupling for a two orbital trilayer using the numerical approach as outlined in Section 3.2 requires a large amount of time. As we wish to model a variety of trilayers here we use the alternative analytic approach of Section 3.3. Since we have to treat the single and double period exchange coupling separately using this method we also outline their method of computation separately.

Single-period exchange coupling

The final step when computing the exchange coupling is obtained using Equation 3.31. The thermodynamic potentials $\Omega^{\uparrow\downarrow}(N)_{FM}$ and $\Omega^{\uparrow\downarrow}(N)_{AF}$ in this formula are calculated by using Equation 3.36. It can be seen from the formula for $\Omega^{s}(N)$ that several factors need to be obtained and they are all found using the method as set out in Section 3.3.2.

Double-period exchange coupling

The final step when computing the exchange coupling is obtained using the same formula as for single-period exchange coupling ie Equation 3.31. The difference here for double-period exchange coupling is the thermodynamic potentials $\Omega^{\uparrow\downarrow}(N)_{FM}$ and $\Omega^{\uparrow\downarrow}(N)_{AF}$ are calculated by using Equation 3.59 instead. Finally all the factors in this formula are obtained using the methods as set out in Section 3.3.6.

3.4.2 No hybridization in the spacer layer

The first example of exchange coupling for a two orbital (001) trilayer we consider is when there is no hybridization in the spacer layer only. Electrons are free to hop from band to band in the semi-infinite ferromagnetic layers. The bands employed in our calculation of J(N) are shown in Figure 3.11. From this diagram we see that only one band is intersected by the Fermi energy level in the spacer layer. The exchange coupling oscillates with one period only so we compute J(N) using the single-period method.

The dependence of the spectral density on the spacer thickness for the up spin band of the ferromagnetic configuration of the trilayer is shown in Figure 3.12. The spectral density for the down spin band is shown in Figure 3.13. The dependence of the spectral density on the spacer thickness for the up and down spin bands of the antiferromagnetic configuration is shown in Figure 3.14. The samples of the spectral densities are all taken to be between 500 and 600 atomic planes as they behave asymptotically like periodic functions for larger spacer thicknesses. Then using the periodicity of the spectral densities, which for this example is $\simeq 7.55$ atomic planes, the data sets are shifted. The shifted spectral densities are shown in Figure 3.15. The Fourier coefficients are computed from the shifted spectral densities and finally the exchange coupling is shown in Figure 3.16. The vertical axis in this graph should read $\mathrm{J(N)}a^2$ and a cubic spline has been fitted to the data.

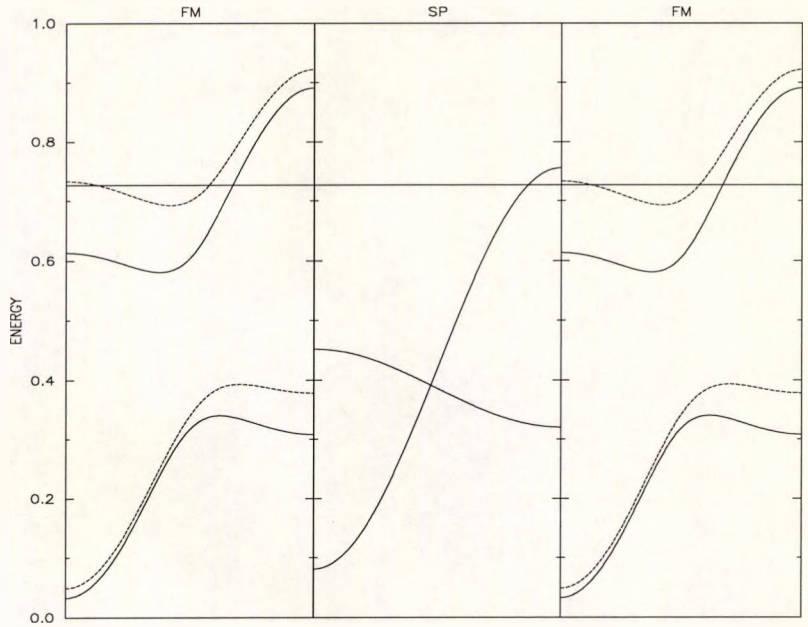

Figure 3.11: Bands in the ferromagnetic layers $FM^{\uparrow}$ (solid line) and $FM^{\downarrow}$ (dashed line) and the spacer layer SP. The straight solid line is the Fermi energy level.

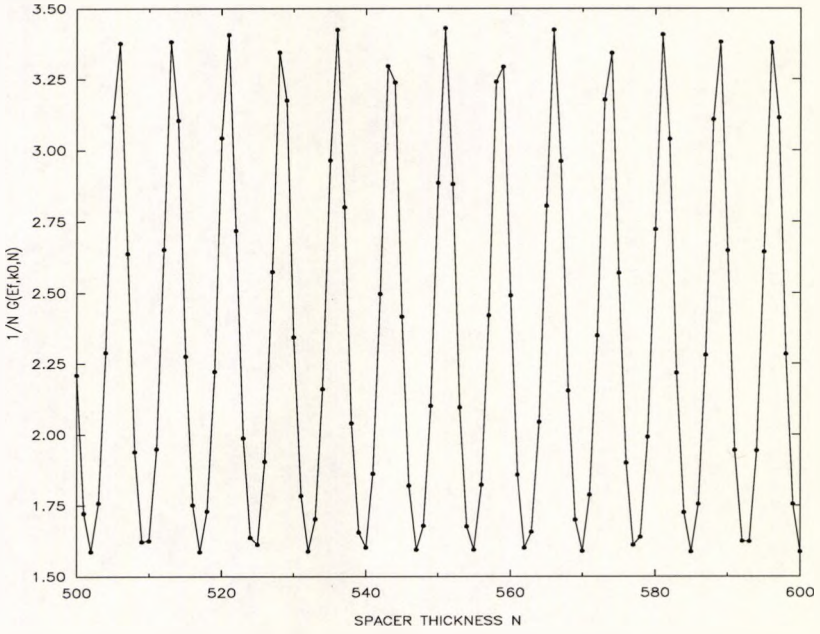

Figure 3.12: Dependence of the spectral density on N for the up spin band of the FM configuration of the trilayer. It is evaluated at $k_x = k_y = 0$ and $E = E_f$. The solid line simply connects the points (solid circle) as a visual aid.

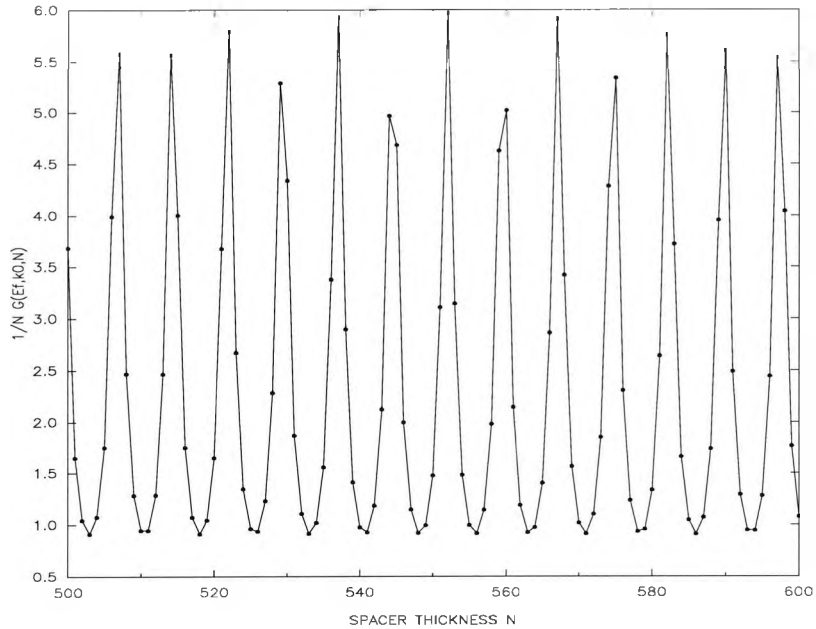

Figure 3.13: Dependence of the spectral density on N for the down spin band of the FM configuration of the trilayer. It is evaluated at $k_x = k_y = 0$ and $E = E_f$.

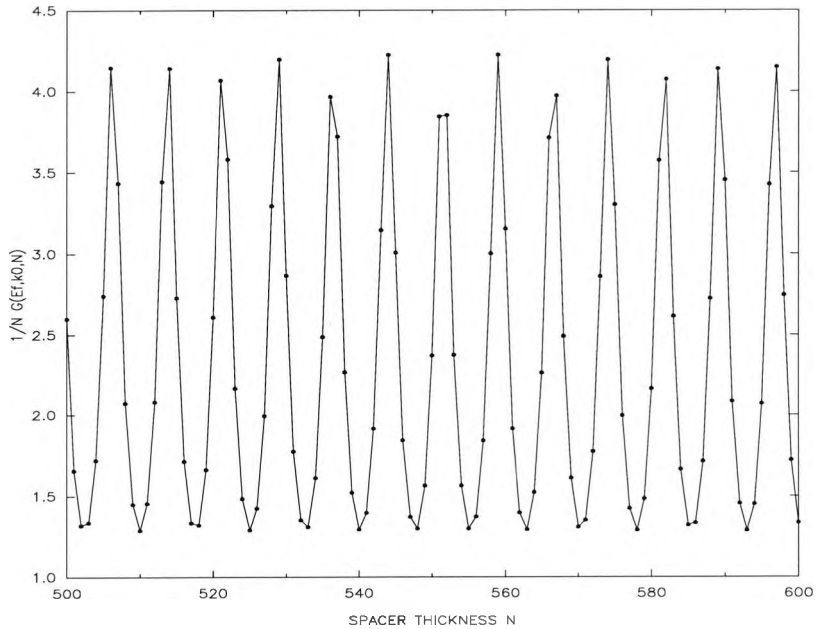

Figure 3.14: Dependence of the spectral density on N for the up and down spin bands of the AF configuration of the trilayer. It is evaluated at $k_x = k_y = 0$ and $E = E_f$.

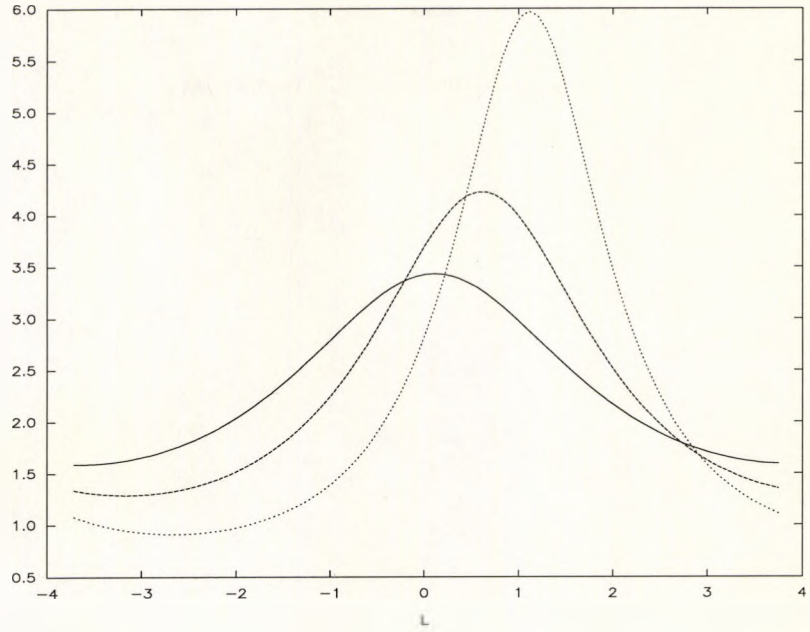

Figure 3.15: Plot of the shifted spectral density for the up spin band (solid line) and down spin band (dotted line) of the ferromagnetic configuration of the trilayer. The dashed line is the shifted spectral density for the up and down spin bands of the antiferromagnetic configuarion of the trilayer.

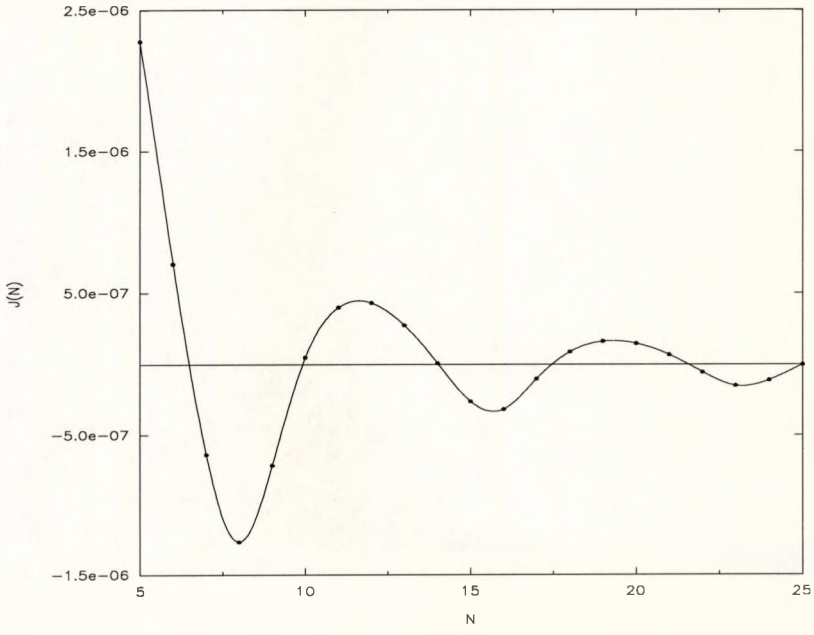

Figure 3.16: Exchange coupling for (001) trilayer associated with the point $k_x = k_y = 0$.

3.4.3 Hybridization in the spacer layer

The aim of this section is to investigate what effect the hybridization in the spacer layer has on the exchange coupling for a two orbital (001) trilayer. To do this we consider three separate example trilayers and once the exchange coupling has been computed for each trilayer we compare the results. All the parameters describing each of the three trilayers are the same except for the hybridization in the spacer layer. In doing this we can isolate what effect the hybridization in the spacer layer has on the exchange coupling. We use as our "basis" trilayer the one that was used in Section 3.4.2 where there was no hybridization in the spacer layer. For our first trilayer we add a small amount of hybridization to the spacer layer. In the second trilayer we increase the hybridization in the spacer layer some more and for the third example we increase the hybridization even further. In all three examples only one band in the spacer layer is intersected by the Fermi energy level so the exchange coupling oscillates with a single period and we use the single-period method to compute J(N).

The band structure for the first trilayer is shown in Figure 3.17. The dependence of the spectral density for the up spin band of the ferromagnetic configuration of the trilayer is shown in Figure 3.18. The dependence of the spectral density for the down spin band is shown in Figures 3.19. The dependence of the spectral density on the spacer thickness for the up and down spin bands of the antiferromagnetic configuration of the trilayer in shown in Figure 3.20. The spectral densities are shifted using its periodicity, which for this trilayer is $\simeq 7.39$ atomic planes and are

shown in Figure 3.21.

The bands employed in our second trilayer are shown in Figure 3.22. The dependence of the spectral density on the spacer thickness for the up spin band of the ferromagnetic configuration of the trilayer is shown in Figure 3.23. The dependence of the spectral density for the down spin band is shown in Figure 3.24. The dependence of the spectral density on the spacer thickness for the up and down spin bands of the antiferromagnetic configuration of the trilayer is shown in Figure 3.25. The spectral densities are shifted using the periodicity which for this example is $\simeq$ 6.97 atomic planes and are shown in Figure 3.26.

The bands employed in our third trilayer are shown in Figure 3.27. This trilayer is a (001) Co/Cu trilayer, see Ref [46]. There is only one Cu band in the (001) direction which is intersected by the Fermi surface. It hybridizes with the d-band and it follows that it is only these two bands in Cu that determine the coupling. Therefore we can describe the electronic structure of the (001) Co/Cu trilayer using two hybridizing tight-binding bands. The dependence of the spectral density on the spacer thickness for the up spin band of the ferromagnetic configuration of the trilayer is shown in Figure 3.28. The dependence of the spectral density for the down spin band is shown in Figure 3.29. The dependence of the spectral density on the spacer thickness for the up and down spin bands of the antiferromagnetic configuration of the trilayer is shown in Figure 3.30. The spectral densities are shifted using its periodicity which for this trilayer is $\simeq$ 6.32 atomic planes and are shown in Figure 3.31.

Once the Fourier coefficents have been obtained using the shifted spectral densities we can compute the exchange coupling for each trilayer. A comparison of the results is shown in Figure 3.32. The vertical axis in this graph should read $J(N)a^2$, where a is the inter-atomic distance and a cubic spline has been fitted to the data. It is immediately obvious that the hybridization in the spacer layer has a significant effect on the exchange coupling.

One feature it clearly affects is the period of oscillations. The period is related to the Fermi surface of the spacer layer. As the spacer layer of each trilayer are all different from one another, due to the difference in the hybridization, we expect the periods to be different even before proceeding with the calculations. The results in Figure 3.32 clearly agrees with this. It also shows that as we increase the hybridization between the bands in the spacer layer then the period of oscillations is decreased. This effect can also be confirmed analytically as we can obtain the period analytically.

Another feature to be affected is the amplitude of oscillations. The amplitude of the oscillations is directly related to the difference between the ferromagnetic and antiferromagnetic configurations of the trilayer. One factor that plays a part in this is the exchange splitting of the ferromagnetic layers. The ferromagnetic layers in all three trilayers are the same so the difference in the amplitudes cannot be due to the ferromagnetic layers here. We recall from the introduction to the quantum well theory in Section 1.3.3 that exchange coupling occurs when there is a potential well formed by the trilayer. The strength of the exchange coupling can be directly

related to the depth of the potential well. The hybridization has caused a shift in the bands of the spacer layer and altered the relative depth of the wells, which in turn effects the amplitude of oscillations. We make the conclusion from Figure 3.32 that increasing the hybridization in the spacer layer increases the amplitude of the oscillatory exchange coupling.

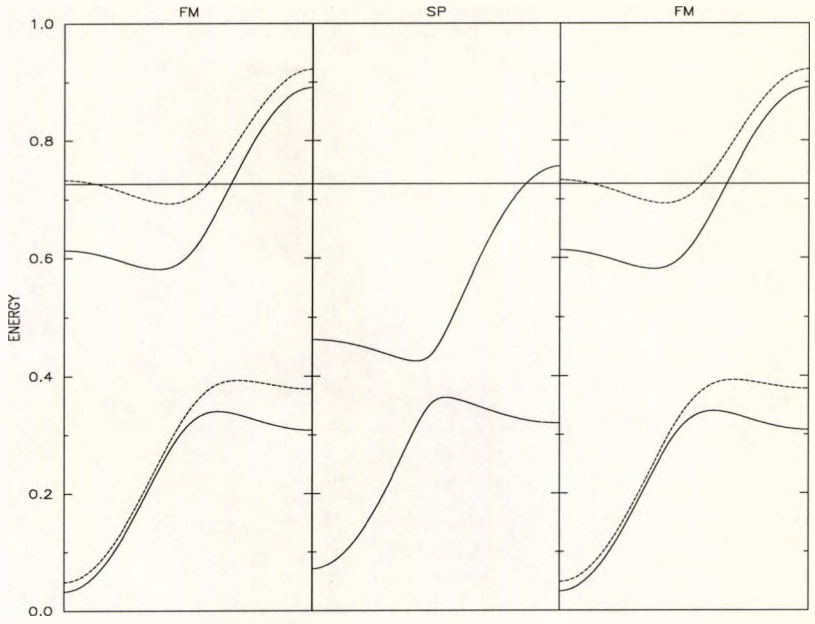

Figure 3.17: Bands in the ferromagnetic layers $FM^{\uparrow}$ (solid line) and $FM^{\downarrow}$ (dashed line) and the spacer layer SP. The straight solid line is the Fermi energy level.

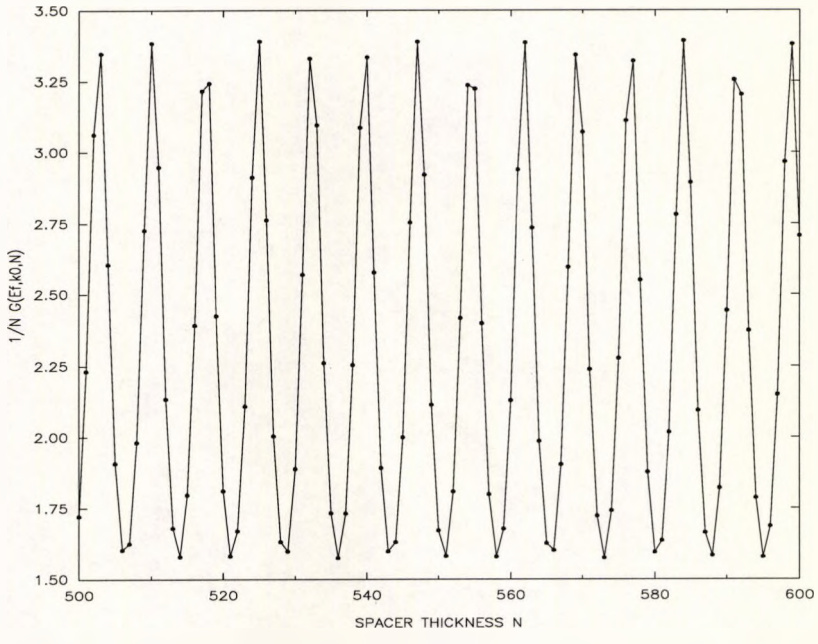

Figure 3.18: Dependence of the spectral density on N for the up spin of the FM configuration of the trilayer. It is evaluated at $k_x = k_y = 0$ and $E = E_f$.

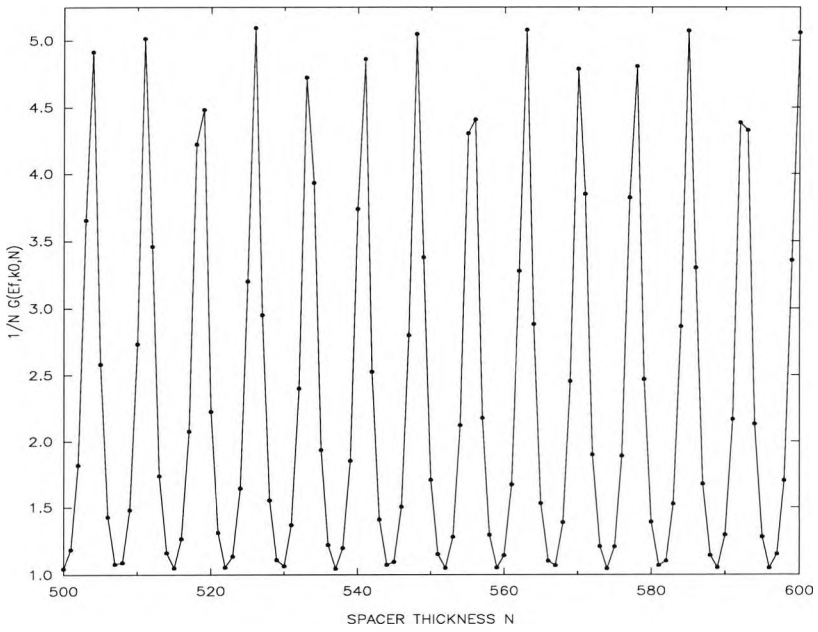

Figure 3.19: Dependence of the spectral density on N for the down spin band of the FM configuration of the trilayer. It is evaluated at $k_x = k_y = 0$ and E = E_f.

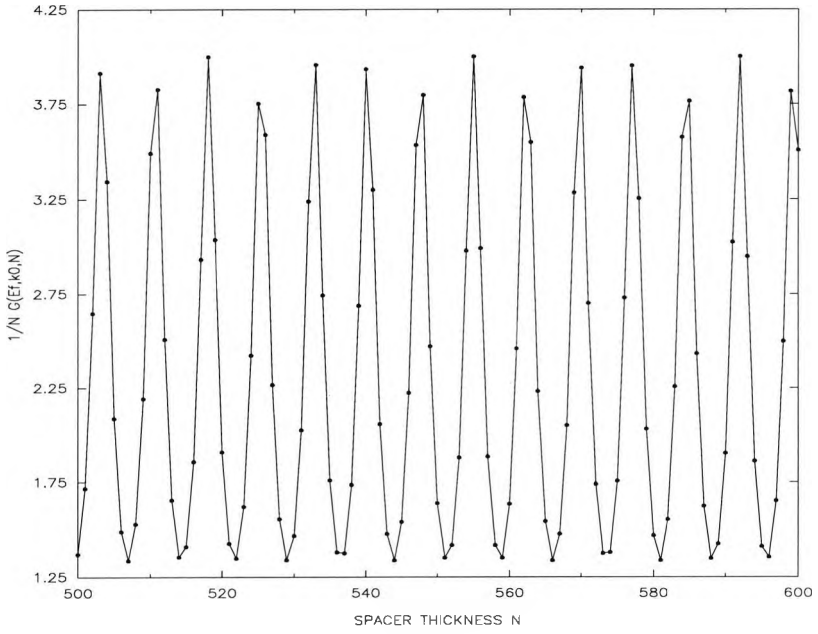

Figure 3.20: Dependence of the spectral density on N for the up and down spin bands of the AF configuration of the trilayer. It is evaluated at $k_x = k_y = 0$ and E = E_f.

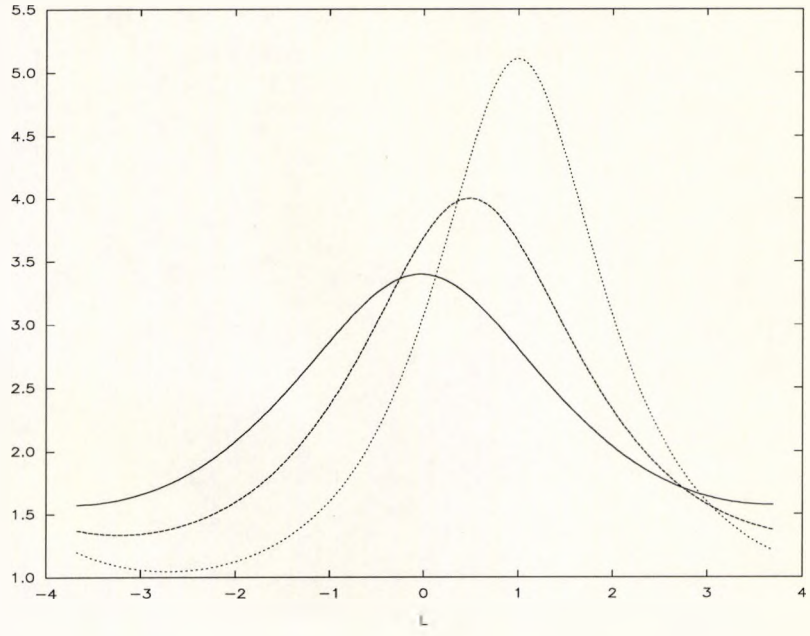

Figure 3.21: Plot of the shifted spectral density for the up spin band (solid line) and down spin band (dotted line) of the ferromagnetic configuration of the trilayer. The dashed line is the shifted spectral density for the up and down spin bands of the antiferomagnetic configuration of the trilayer.

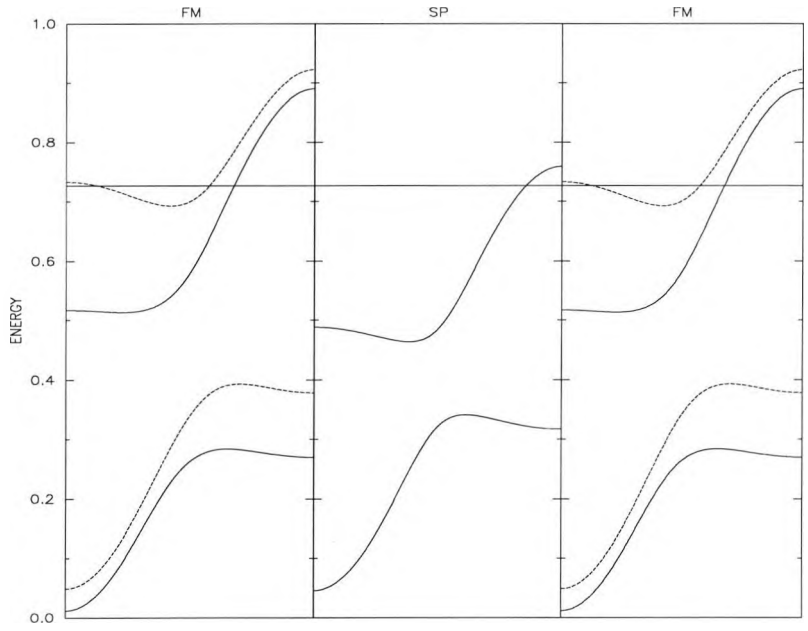

Figure 3.22: Bands in the ferromagnetic layers $FM^{\uparrow}$ (solid line) and $FM^{\downarrow}$ (dashed line) and the spacer layer SP. The straight solid line is the Fermi energy level.

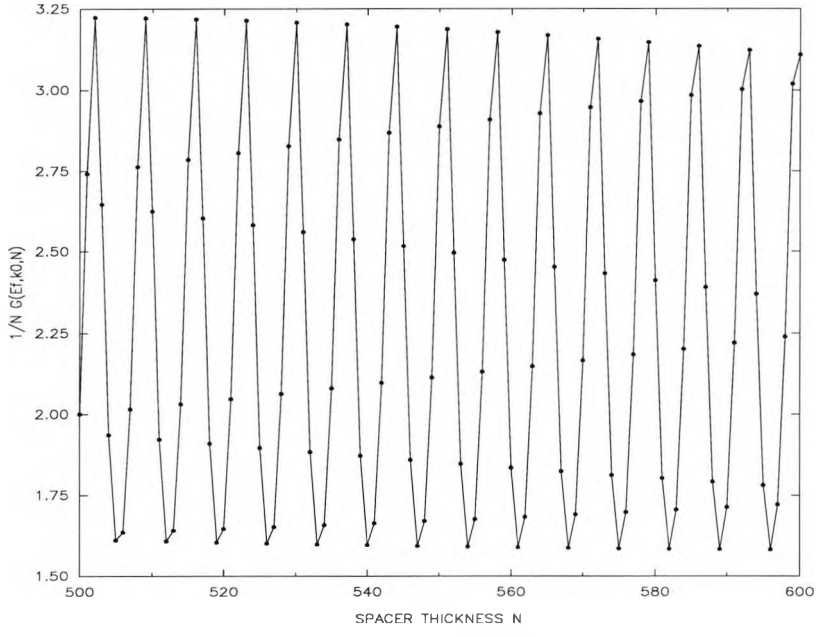

Figure 3.23: Dependence of the spectral density on N for the up spin band of the FM configuration of the trilayer. It is evaluated at $k_x = k_y = 0$ and $E = E_f$.

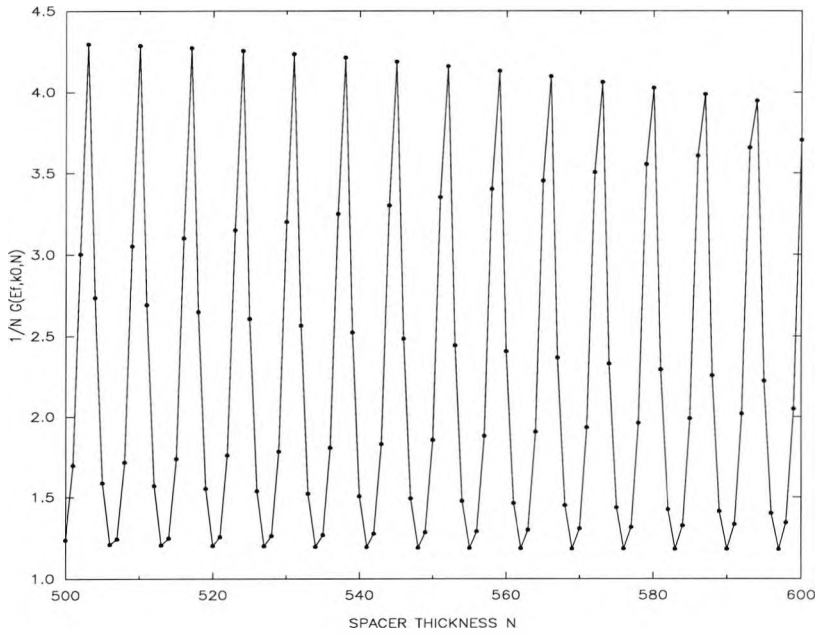

Figure 3.24: Dependence of the spectral density on N for the down spin band of the FM configuration of the trilayer. It is evaluated at $k_x = k_y = 0$ and E = E_f.

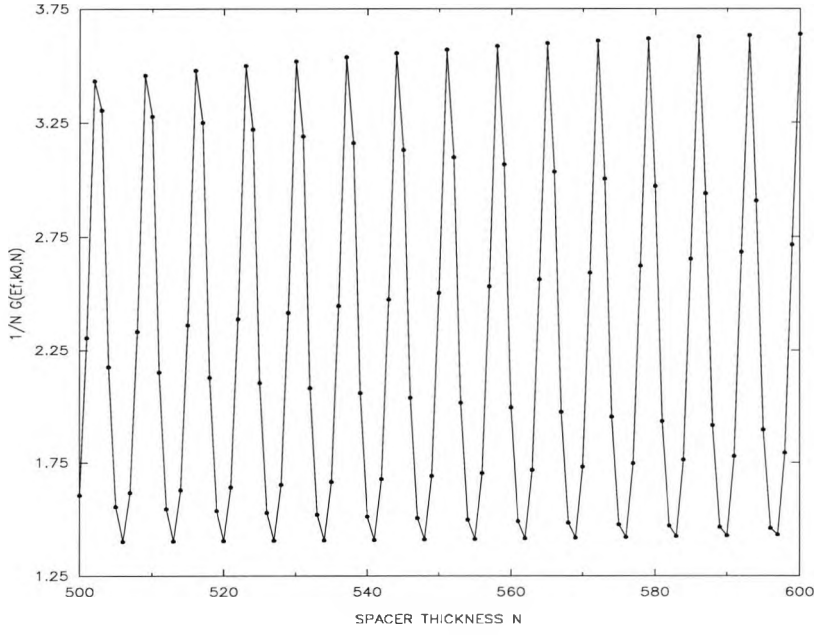

Figure 3.25: Dependence of the spectral density on N for the up and down spin bands of the AF configuration of the trilayer. It is evaluated at $k_x = k_y = 0$ and E = E_f.

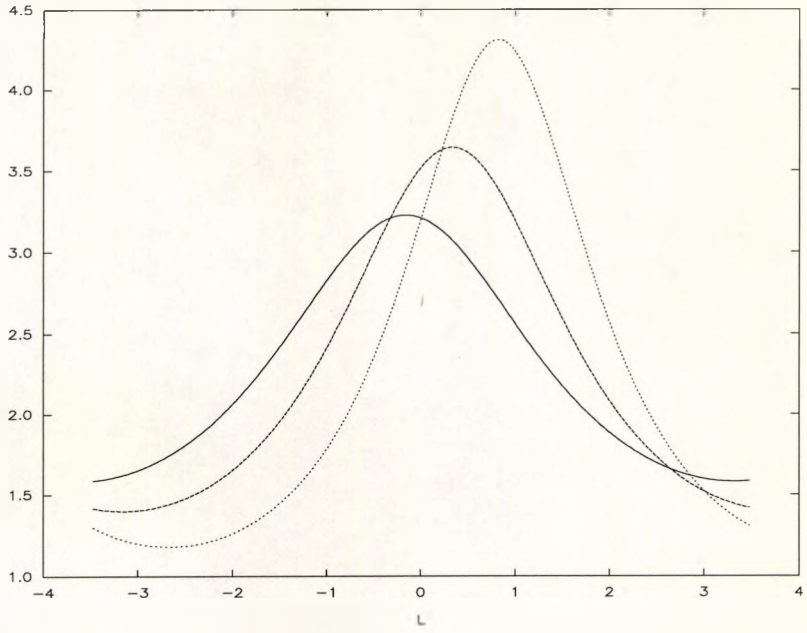

Figure 3.26: Plot of the shifted spectral density for the up spin band (solid line) and down spin band (dotted line) of the feromagnetic configuration of the trilayer. The dashed line is the shifted spectral density for the up and down spin bands of the antiferromagnetic configuration of the trilayer.

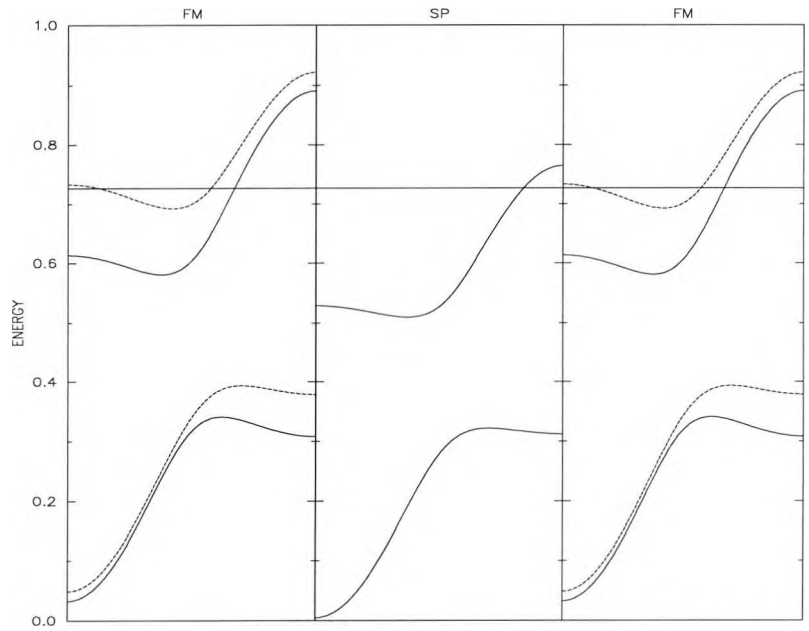

Figure 3.27: Bands in the ferromagnetic layers $FM^{\uparrow}$ (solid line) and $FM^{\downarrow}$ (dashed line) and the spacer layer SP. The straight solid line is the Fermi energy level.

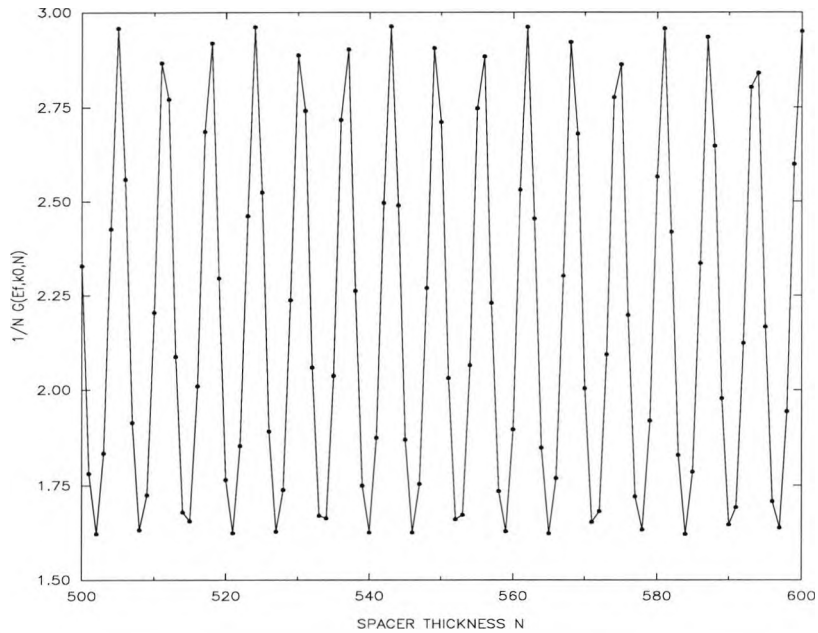

Figure 3.28: Dependence of the spectral density on N for the up spin band of the FM configuration of the trilayer. It is evaluated at $k_x = k_y = 0$ and $E = E_f$.

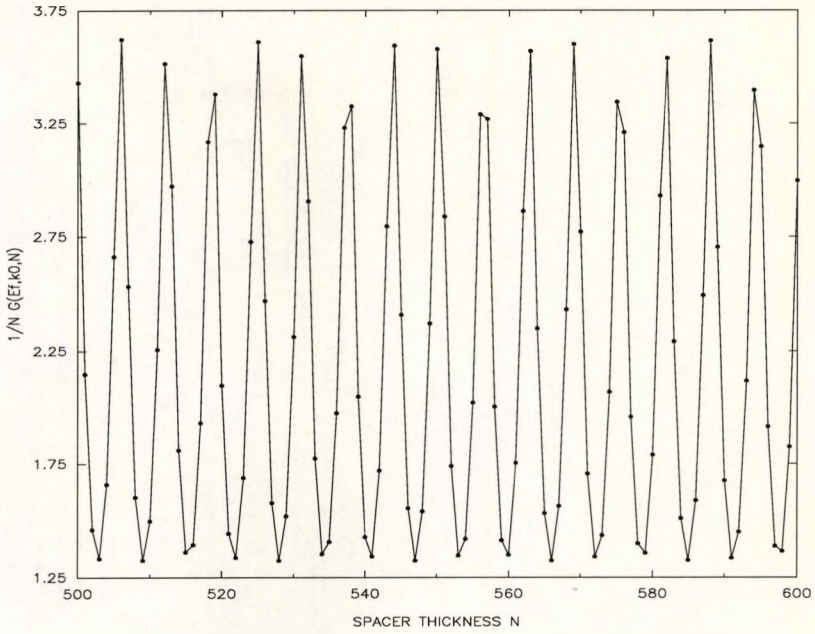

Figure 3.29: Dependence of the spectral density on N for the down spin band of the FM configuration of the trilayer. It is evaluated at $k_x = k_y = 0$ and E = E_f.

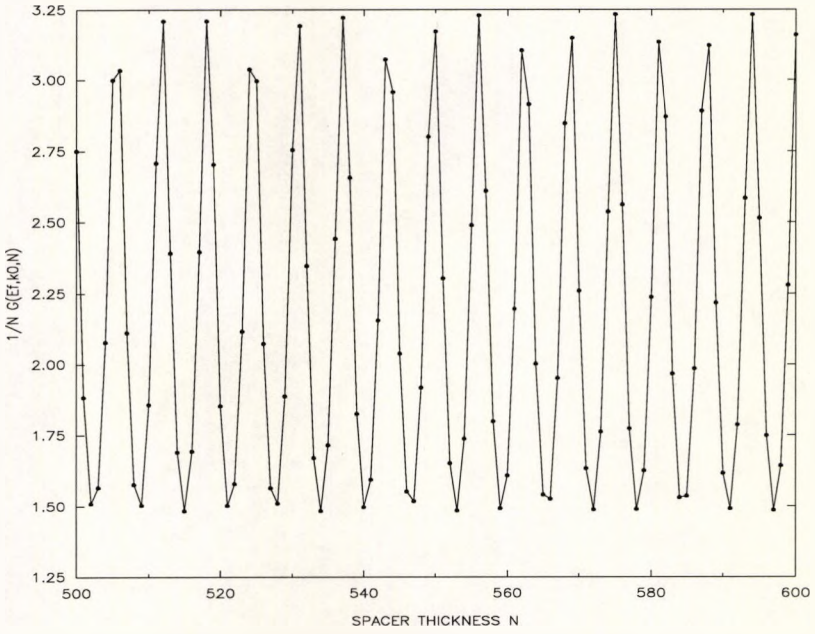

Figure 3.30: Dependence of the spectral density on N for the up and down spin bands of the AF configuration of the trilayer. It is evaluated at $k_x = k_y = 0$ and E = E_f.

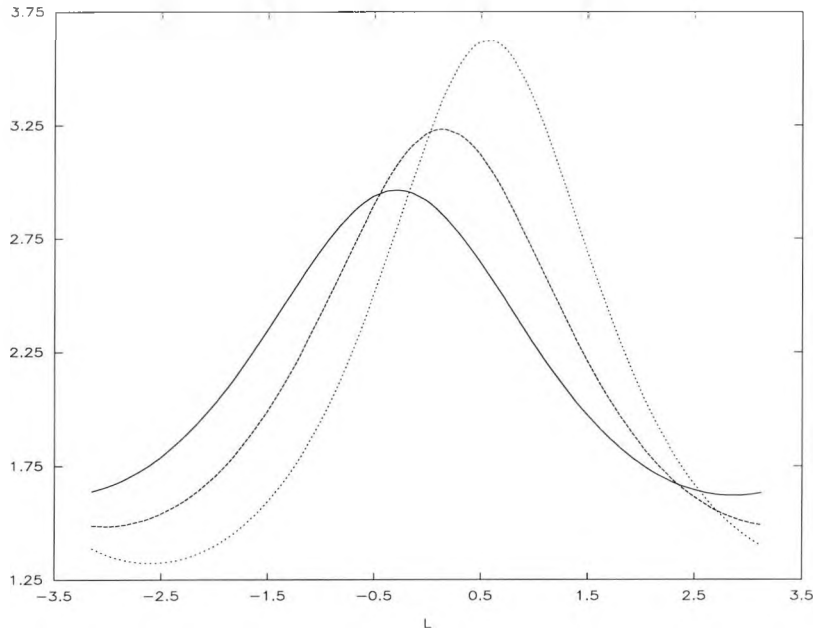

Figure 3.31: Plot of the shifted spectral density for the up spin band (solid line) and down spin band (dotted line) of the ferromagnetic configuration of the trilayer. The dashed line is the shifted spectral density for the up and down spin bands of the antiferromagnetic configuration of the trilayer.

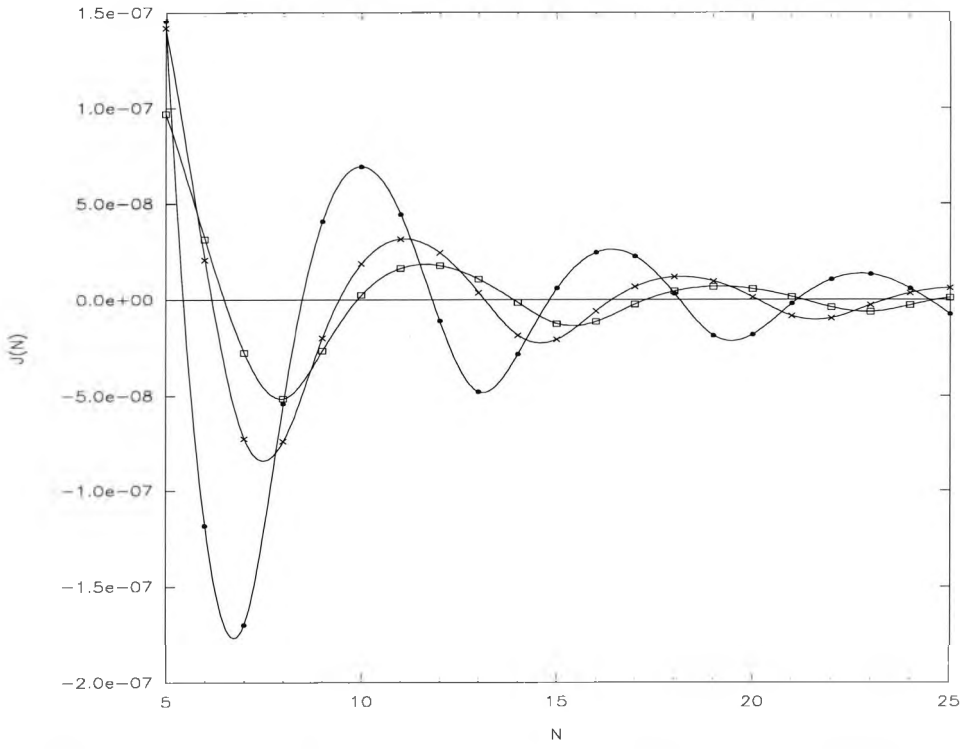

Figure 3.32: Comparison of the exchange coupling for this section. The squares are the first example. The X's are our second example and the solid cirlces are the third example.

3.4.4 Hybridization in the ferromagnetic layers

In this Section we turn our attention to investigating what effect the hybridization in the ferromagnetic layers has on the exchange coupling for a two orbital (001) trilayer. As when investigating hybridization in the spacer layer we do this using three examples and compare the corresponding results. For this section we use as our "basis" trilayer the third trilayer in Section 3.4.2 ie a Co/Cu trilayer see Ref [46]. We start by setting the hybridization in the ferromagnetic layers equal to zero for our first example. In the second we add a small amount of hybridization to the ferromagnetic layers. Finally for the third trilayer we increase the hybridization between the bands in the ferromagnetic layers even further. By only changing the hybridization in the ferromagnetic layers we can isolate what effect it has on the exchange coupling. In all three examples only one band in the spacer layer is intersected by the Fermi energy level so the exchange coupling oscillates with a single period and we use the single-period method to compute J(N).

The bands employed in our first trilayer are shown in Figure 3.33. The dependence of the spectral density on the spacer thickness for the up spin band of the ferromagnetic configuration of the trilayer is shown in Figure 3.34. The spectral density for the down spin band is shown in Figure 3.35. The dependence of the spectral density on the spacer thickness for the up and down spin bands of the antiferromagnetic configuration of the trilayer is shown in Figure 3.36. The spectral densities are shifted using the periodicity which for this example is $\simeq 6.32$ atomic planes and are shown in Figure 3.37.

The bands employed in our second trilayer are shown in Figure 3.38. The dependence of the spectral density on the spacer thickness for the up spin band of the ferromagnetic configuration of the trilayer is shown in Figure 3.39. The spectral density for the down spin band is shown in Figure 3.40. The dependence of the spectral density on the spacer thickness for the up and down spin bands of the antiferromagnetic configuration of the trilayer is shown in Figure 3.41. The shifted spectral densities for each respective spectral density are shown in Figure 3.42 from which we use to obtain all the Fourier coefficients.

The band employed in our third trilayer are shown in Figure 3.43. The dependence of the spectral density on the spacer thickness for the up spin band of the feromagnetic configuration of the trilayer is shown in Figure 3.44. The dependence of the spectral density on the spacer thickness for the down spin band is shown in Figure 3.45. The dependence of the spectral density for the up and down spin bands of the antiferromagnetic configuration of the trilayer is shown in Figure 3.46. Finally the shifted spectral densities for each respective spectral density is shown in Figure 3.47, which we use to obtain the Fourier coefficients.

Once all the Fourier coefficients have been obtained it is then possible to compute the exchange coupling for each of the three trilayers. A comparison of the exchange coupling for the three trilayers is shown in Figure 3.48 and as before the vertical axis should read $J(N) \times a^2$, where a is the inter-atomic distance and a cubic spline has been fitted to the data. As has already been seen with the derivation of the SPA the period of oscillations are directly related to the Fermi surface of the spacer

layer only. In this section the spacer layer is exactly the same for all three trilayers. Therefore we expect the period to be the same for all three trilayers and we find analytically the period p to be $\simeq 6.32$ atomic planes. Figure 3.48 demonstrates the period is indeed the same for all three trilayers. The point is further confirmed by looking at the shifted spectral densities. We use the period to shift the spectral density so that all the points lie within the region -p/2 to p/2. As we take our sample data set to be between 500 and 600 atomic planes in the spacer layer, to eliminate any interfacial effects, the shifting is sensitive to the period. By this we mean if the period used to shift the data differs even slightly from the true period then we would not obtain smooth curves for the shifted spectral density. We make our first conclusion that the hybridization in the ferromagnetic layers has no effect on the period of the exchange coupling.

The next feature we look at is the amplitude of the oscillations. Again by looking at Figure 3.48 it can be seen the amplitude of the oscillations increases as we increase the hybridization in the ferromagnetic layers. From a purely mathematical viewpoint an increase in the amplitude arises from an increase in the difference between the ferromagnetic and antiferromagnetic configuration of the trilayer. In physical terms this relates to an increase in the exchange splitting of the ferromagnetic layers. Therefore we conclude that increasing the hybridization in the ferromagnetic layers causes an increase in the exchange splitting and will result in a greater amplitude of oscillations in the exchange coupling.

One final affect the hybridization in the ferromagnetic layers has on the exchange

coupling is a phase shift. There is no phase shift between the data sets for the first and second trilayers, which is when there was no hybridization in the ferromagnetic layers and a little hybridization in the second trilayer. However for the third trilayer there a clear phase shift in the data where the hybridization was largest of all. We tentatively conclude the hybridization in the ferromagnetic layers does cause a phase shift.

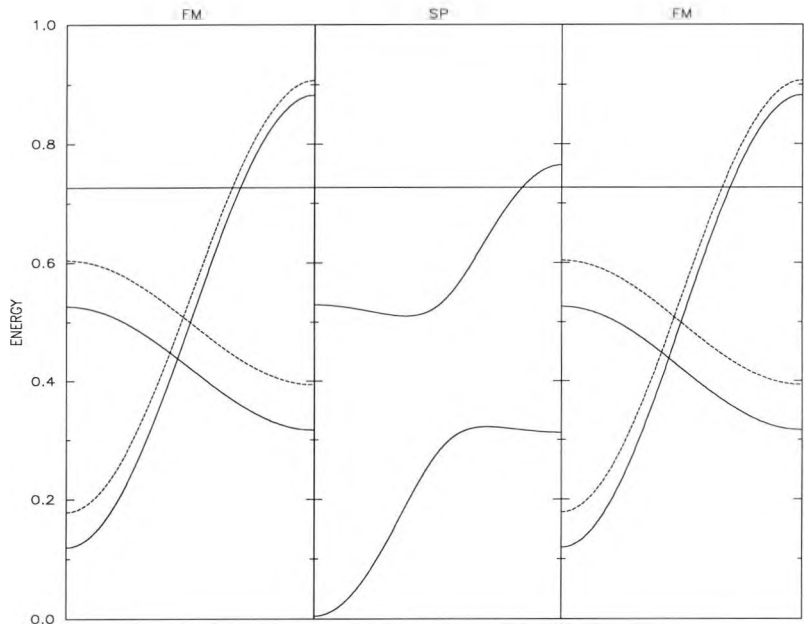

Figure 3.33: Bands in the ferromagnetic layers $FM^{\uparrow}$ (solid line) and $FM^{\downarrow}$ (dashed line) and the spacer layer SP. The straight solid line is the Fermi energy level.

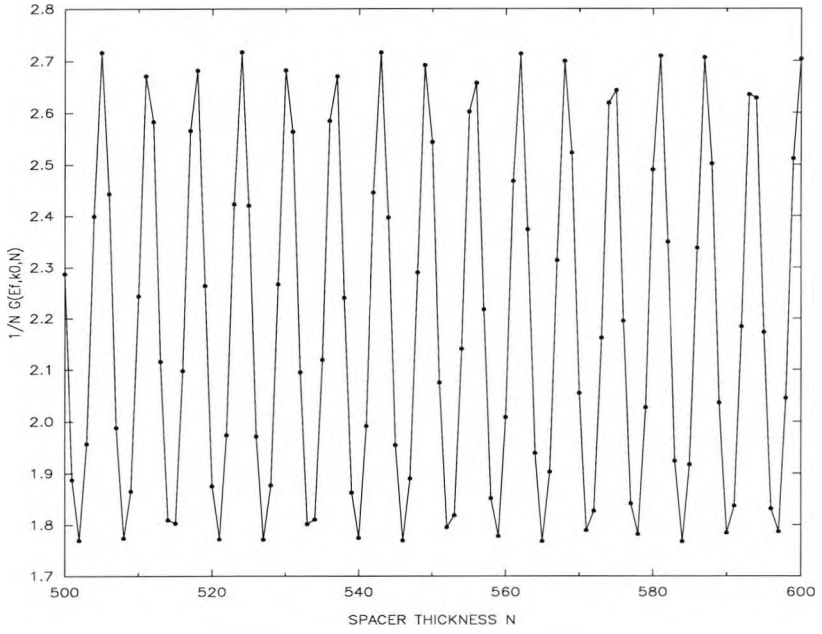

Figure 3.34: Dependence of the spectral density on N for the up spin band of the FM configuration of the trilayer. It is evaluated at $k_x = k_y = 0$ and $E = E_f$.

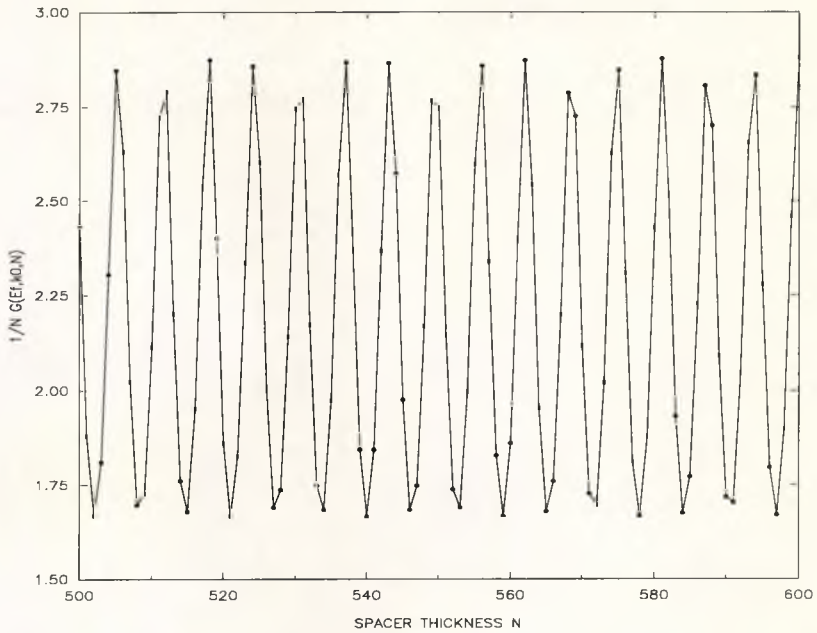

Figure 3.35: Dependence of the spectral density on N for the down spin band of the FM configuration of the trilayer. It is evaluated at $k_x = k_y = 0$ and E = E_f.

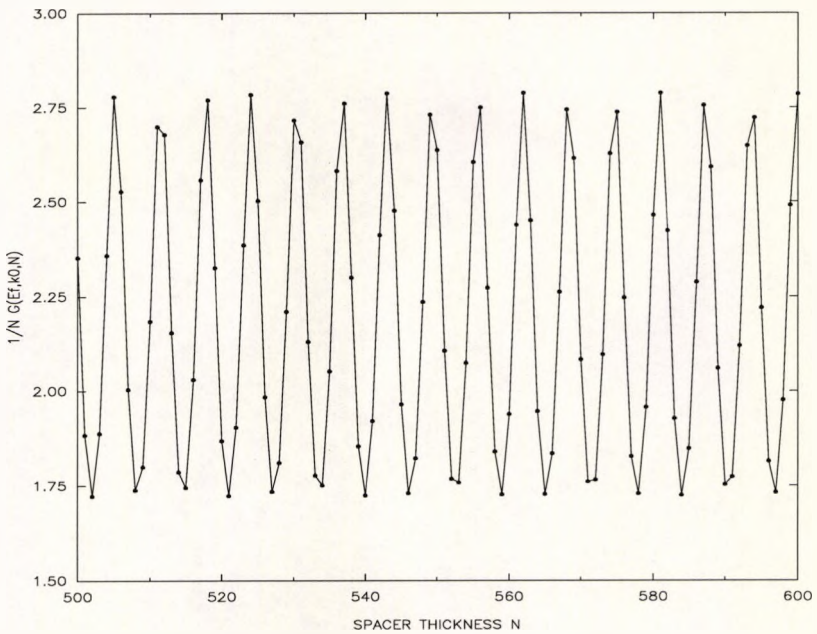

Figure 3.36: Dependence of the spectral density on N for the up and down spin bands of the AF configuration of the trilayer. It is evaluated at $k_x = k_y = 0$ and E = E_f.

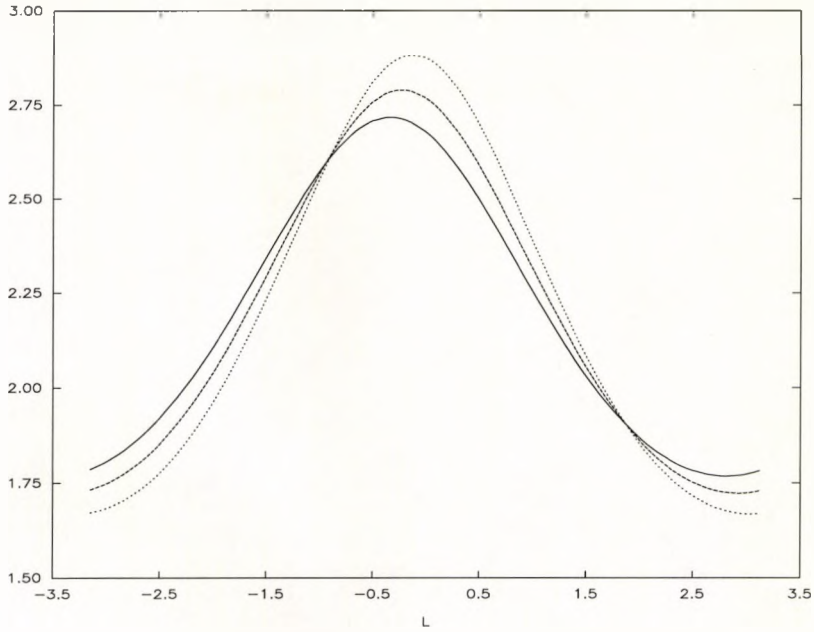

Figure 3.37: Plot of the shifted spectral density for the up spin band (solid line) and down spin band (dotted line) of the ferromagnetic configuration of the trilayer. The dashed line is the shifted spectral density for the up and down spin bands of the antiferromagnetic configuration of the trilayer.

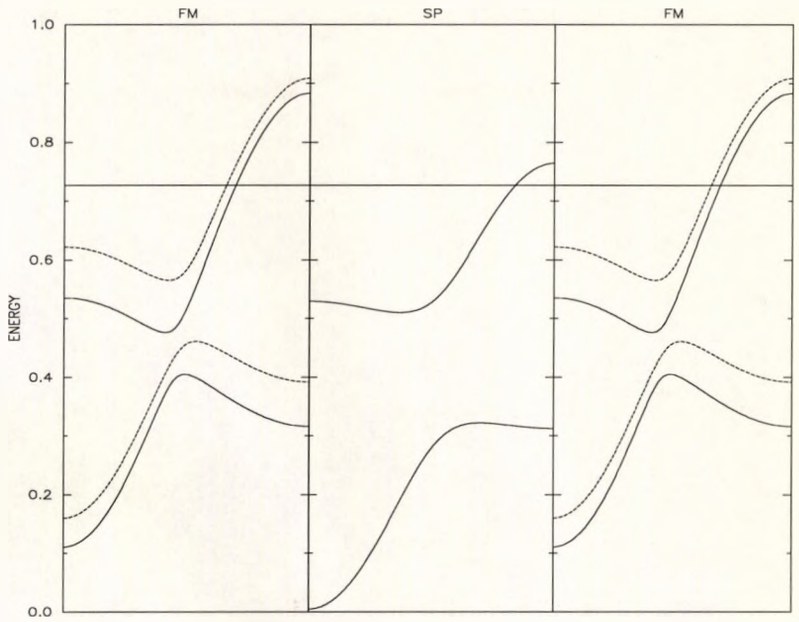

Figure 3.38: Bands in the ferromagnetic layers $FM^{\uparrow}$ (solid line) and $FM^{\downarrow}$ (dashed line) and the spacer layer SP. The straight solid line is the Fermi energy level.

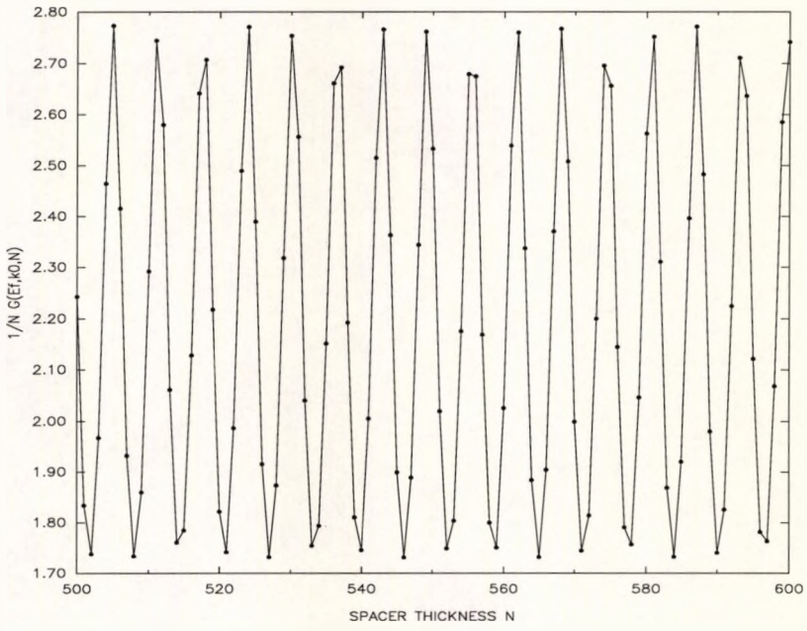

Figure 3.39: Dependence of the spectral density on N for the up spin band of the FM configuration of the trilayer. It is evaluated at $k_x = k_y = 0$ and $E = E_f$.

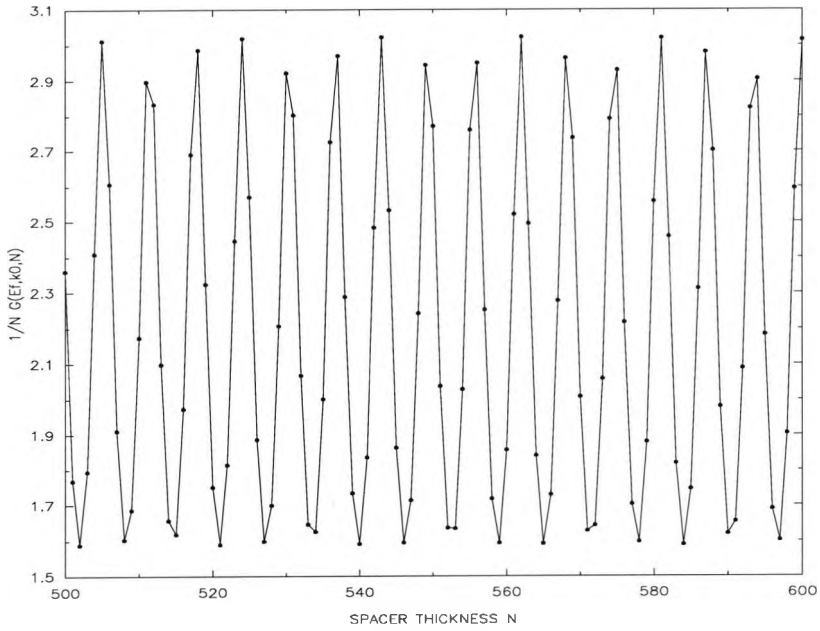

Figure 3.40: Dependence of the spectral density on N for the down spin band of the FM configuration of the trilayer. It is evaluated at $k_x = k_y = 0$ and E = E_f.

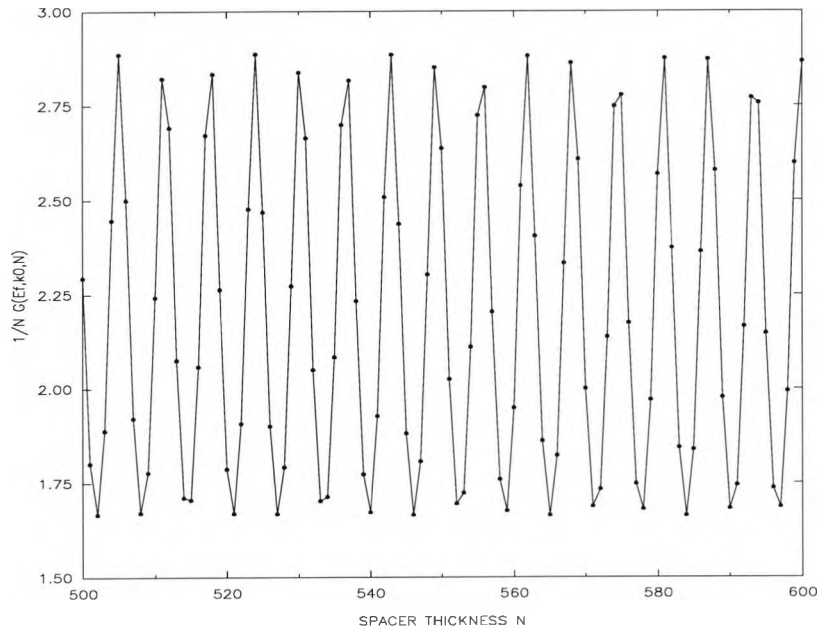

Figure 3.41: Dependence of the spectral density on N for the up and down spin bands of the AF configuration of the trilayer. It is evaluated at $k_x = k_y = 0$ and E = E_f.

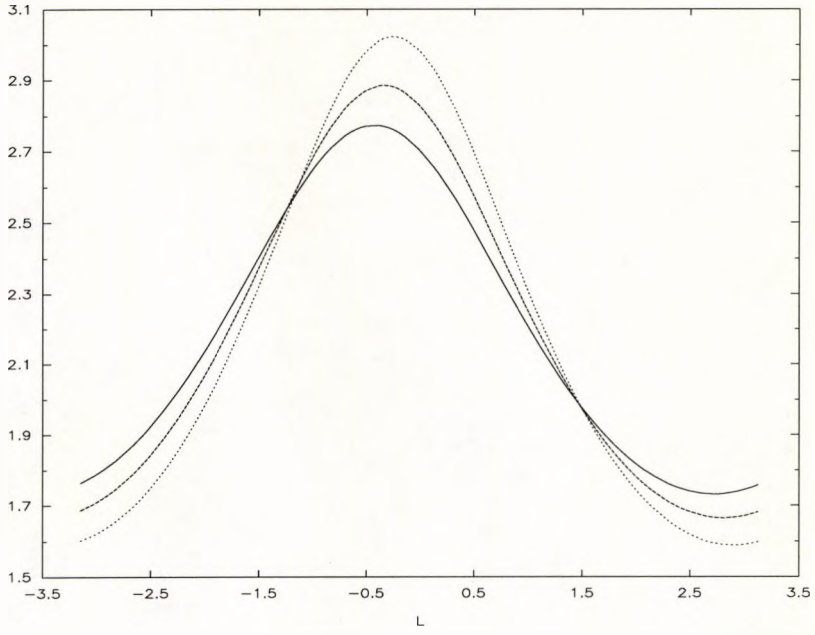

Figure 3.42: Plot of the shifted spectral density for the up spin band (solid line) and down spin band (dotted line) of the ferromagnetic configuration of the trilayer. The dashed line is the shifted spectral density for the up and down spin bands of the antiferromagnetic configuration of the trilayer.

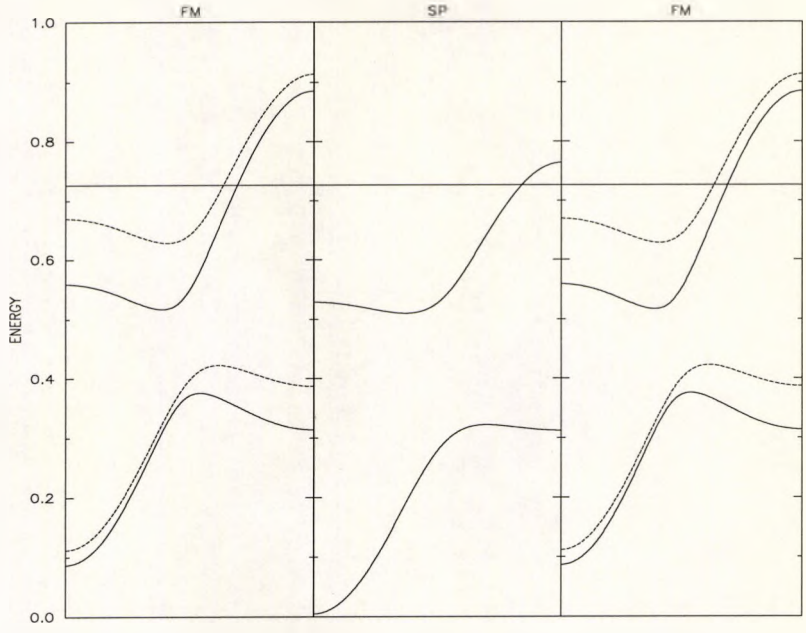

Figure 3.43: Bands in the ferromagnetic layers $FM^{\uparrow}$ (solid line) and $FM^{\downarrow}$ (dashed line) and the spacer layer SP. The straight solid line is the Fermi energy level.

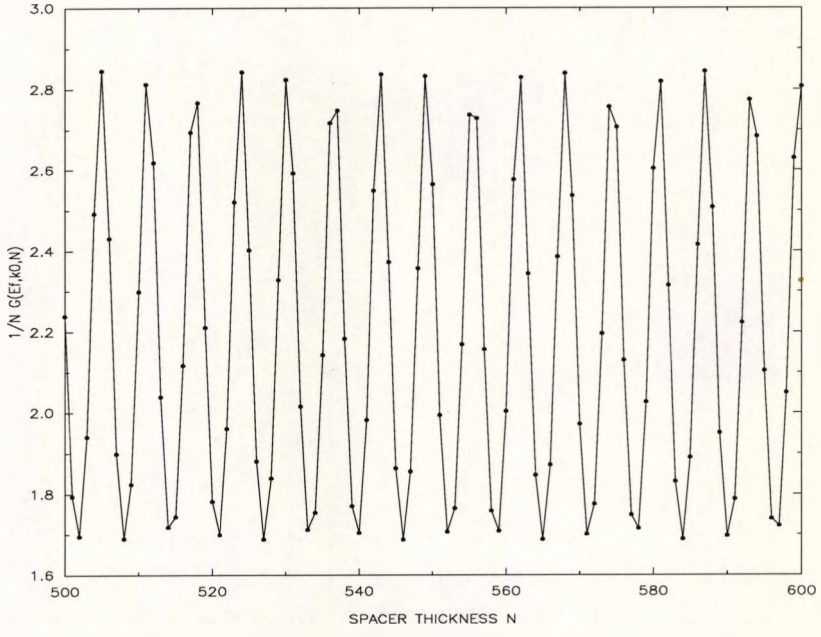

Figure 3.44: Dependence of the spectral density on N for the up spin band of the FM configuration of the trilayer. It is evaluated at $k_x = k_y = 0$ and $E = E_f$.

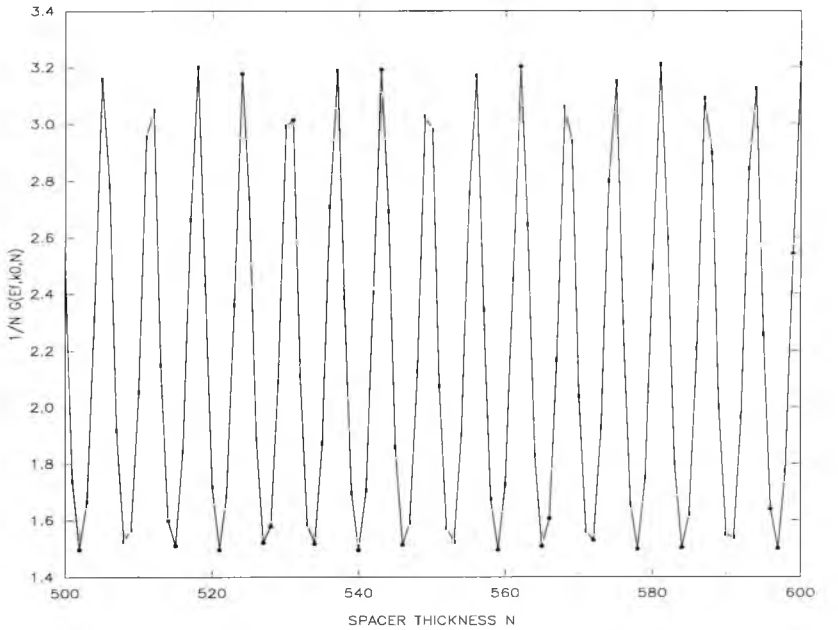

Figure 3.45: Dependence of the spectral density on N for the down spin band of the FM configuration of the trilayer. It is evaluated at $k_x = k_y = 0$ and E = E_f.

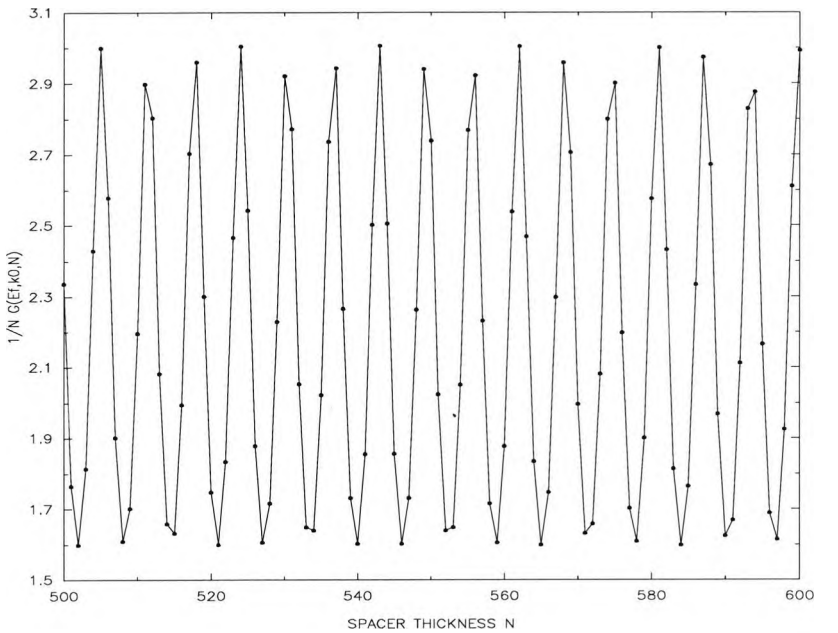

Figure 3.46: Dependence of the spectral density on N for the up and down spin bands of the AF configuration of the trilayer. It is evaluated at $k_x = k_y = 0$ and E = E_f.

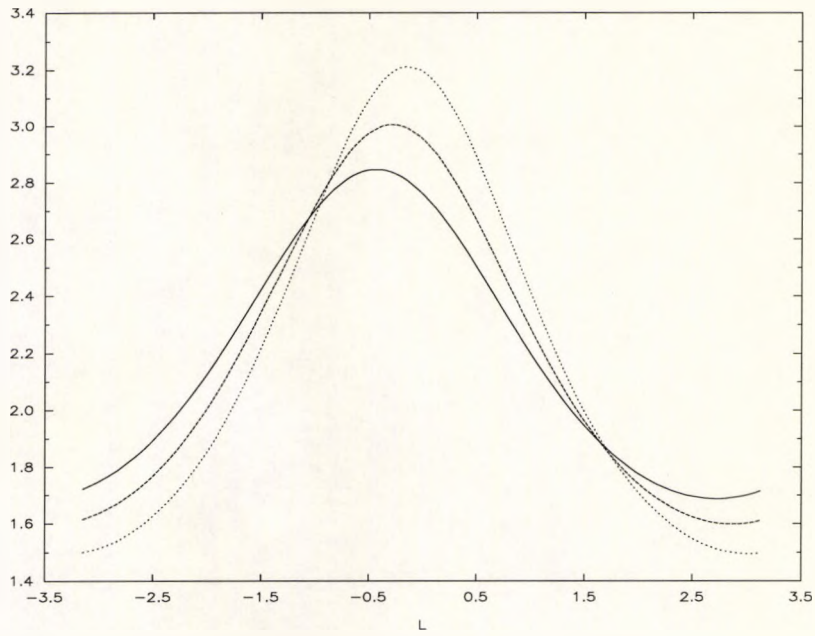

Figure 3.47: Plot of the shifted spectral density for the up spin band (solid line) and down spin band (dotted line) of the ferromagnetic configuration of the trilayer. The dashed line is the shifted spectral density for the up and down spin bands of the antiferromagnetic configuration of the trilayer.

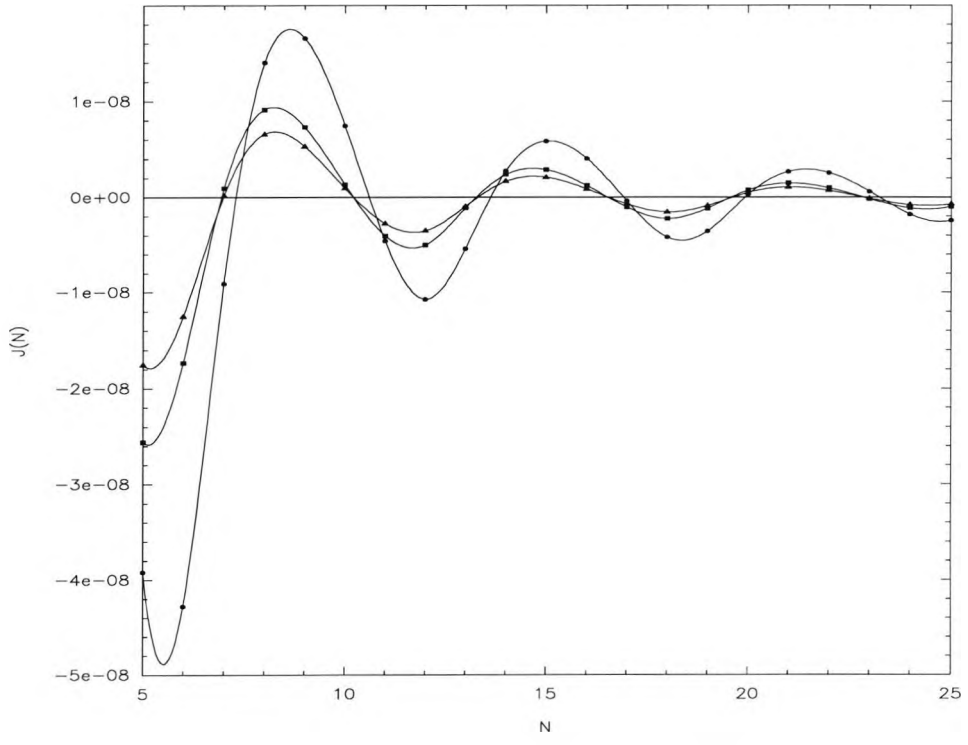

Figure 3.48: Comparison of the exchange coupling for this section. The triangles are the first example. The squares are our second example and the solid cirlces are the third example.

3.4.5 Double-period exchange coupling

We now consider an example of exchange coupling for a two orbital (001) trilayer where there is a double-period of oscillations. The bands employed in our calculation of J(N) are shown in Figure 3.49. For this example the parameters describing the trilayer have been chosen arbitrarily so there is a double period of oscillations and no bound states. In other words both bands in the spacer layer as well as the ferromagnetic layers are intersected by the Fermi energy level. Unlike the other examples for this Section we compute the exchange coupling using both the numerical and analytic approach. Then we compare the results to ensure they are in agreement with each other.

Analytic approach

We compute the exchange coupling using the double-period method of Section 3.4.1. The dependence of the spectral density on the spacer thickness for the up spin band of the ferromagnetic configuration of the trilayer is shown in Figure 3.50. The Fourier coefficients are obtained using the "fitting" procedure as outlined in Section 3.3.6. In Figure 3.51 we compare the spectral density with its corresponding Fourier series representation. The spectral density for the down spin band of the ferromagnetic configuration of the trilayer is shown in Figure 3.52. In Figure 3.53 we compare the spectral density with its corresponding Fourier series representation. The dependence of the spectral density on the spacer thickness for the up and down spin bands of the antiferromagnetic configuration of the trilayer is shown in

Figure 3.54. In Figure 3.55 we compare the spectral density with its Fourier series representation. Once the Fourier coefficients have have been obtained we can then compute the exchange coupling and this is shown in Figure 3.56. The vertical axis in this graph should read $J(N)\times a^2$, where a is the inter-atomic distance and a cubic spline has been fitted to the raw data.

The Fourier series representations of the spectral densities clearly shows the "fitting" procedure works well. In the three graphs Figure 3.51, 3.53 and 3.55 it is clear there is no difference between the spectral densities and their corresponding Fourier series representations. This also demonstrates the spectral densities are indeed quasi-periodic functions in N with two periods which is not clear from a visual inspection of the spectral densities themselves. They appear to be random oscillations rather than quasi-periodic functions. For this example the periods are $\simeq$ 2.55 atomic planes and $\simeq$ 2.13 atomic planes. The graph of the exchange coupling in Figure 3.56 is interesting because it is not immediately obvious the exchange coupling oscillates with two periods. This is due to the two periods being close to one another. However close examination demonstrates there is definitely more than one period of oscillations present. Perhaps a better choice of parameters where the two periods differ greatly would have been more desirable to make it more obvious the exchange coupling oscillates with two periods.

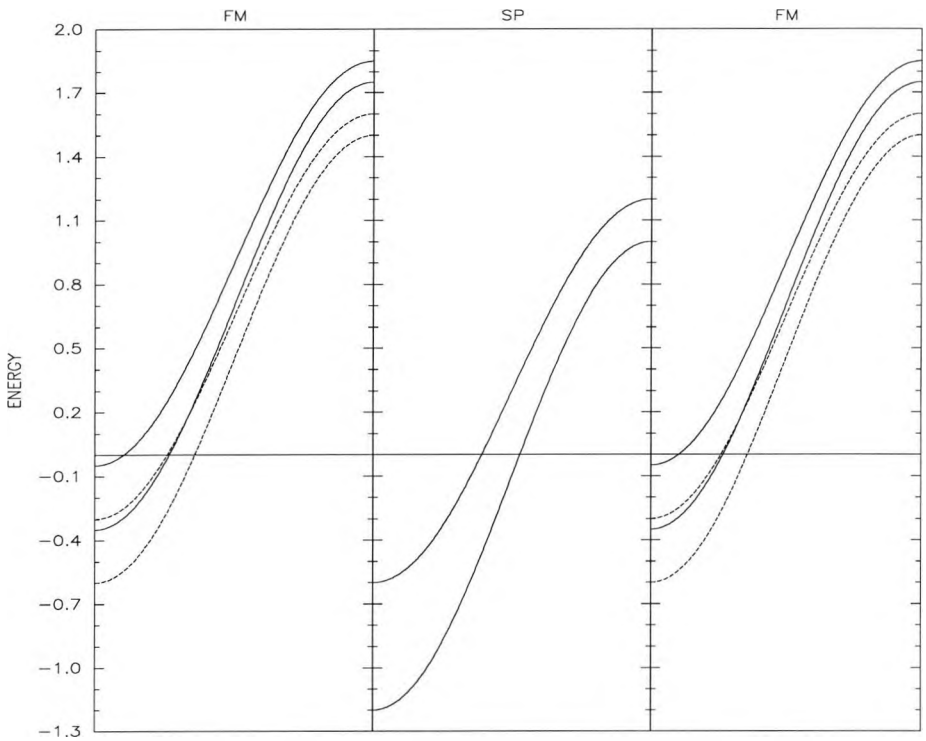

Figure 3.49: Bands in the ferromagnetic layers $FM^{\uparrow}$ (solid line) and $FM^{\downarrow}$ (dashed line) and the spacer layer SP. The straight solid line is the Fermi energy level.

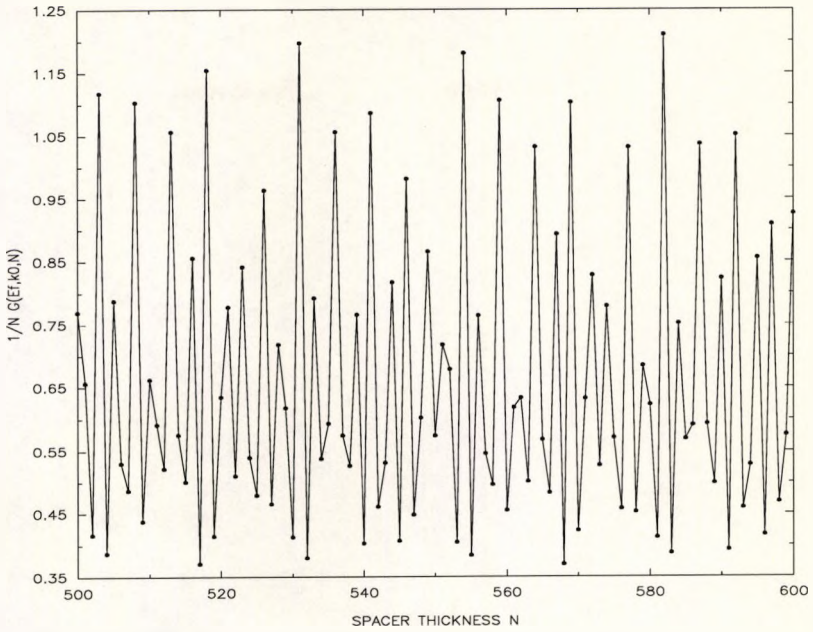

Figure 3.50: Dependence of the spectral density on N for the up spin band of the FM configuration of the trilayer. It is evaluated at $k_x = k_y = 0$ and $E = E_f$.

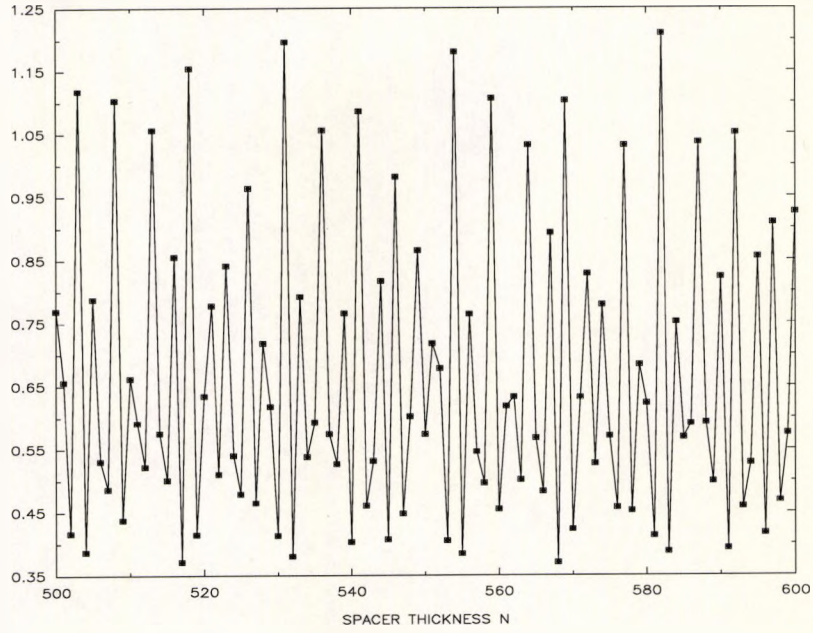

Figure 3.51: Comparison of the spectral density (solid circles) and its corresponding Fourier series representation (open squares).

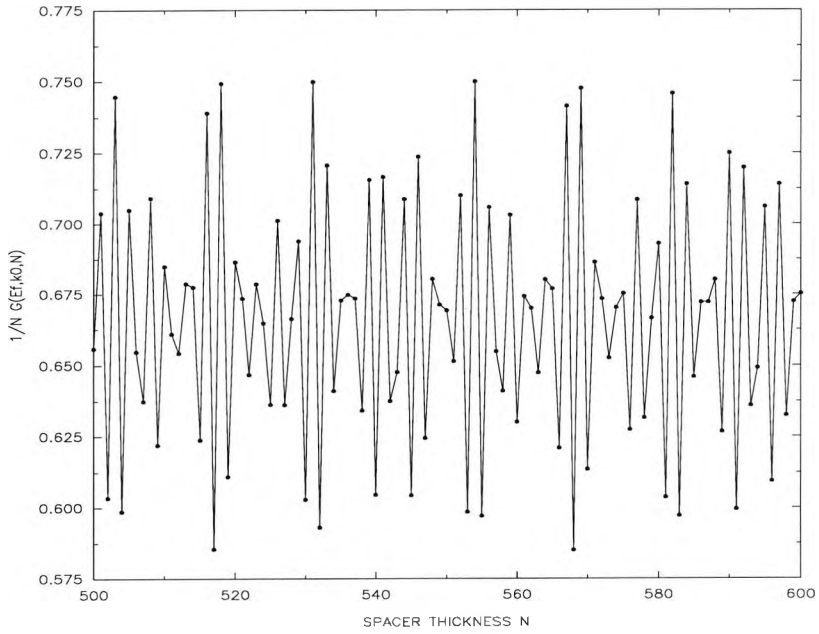

Figure 3.52: Dependence of the spectral density on N for the down spin band of the FM configuration of the trilayer. It is evaluated at $k_x = k_y = 0$ and $E = E_f$.

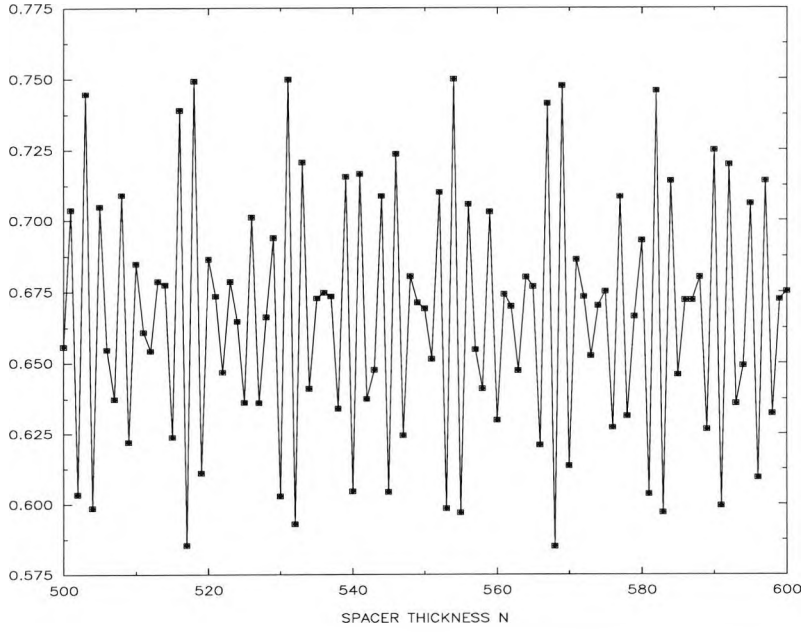

Figure 3.53: Comparison of the spectral density (solid circles) and its corresponding Fourier series representation (open squares).

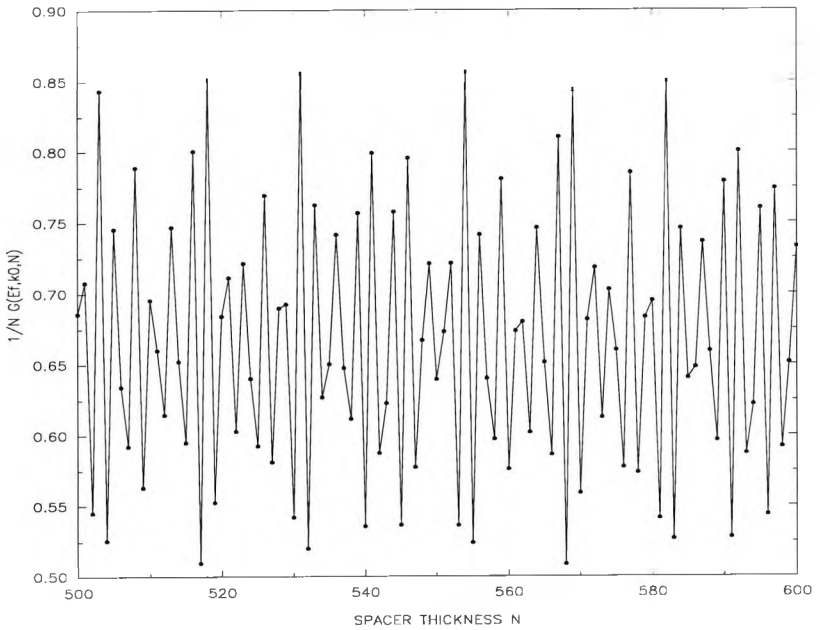

Figure 3.54: Dependence of the spectral density on N for the up and down spin bands of the AF configuration of the trilayer. It is evaluated at $k_x = k_y = 0$ and E = E_f.

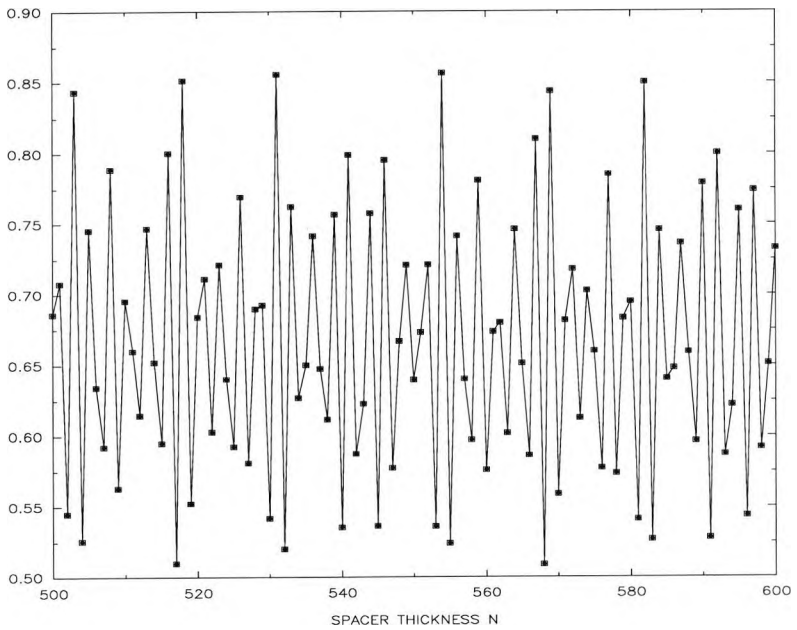

Figure 3.55: Comparison of the spectral density (solid circles) and its corresponding Fourier series representation (open squares).

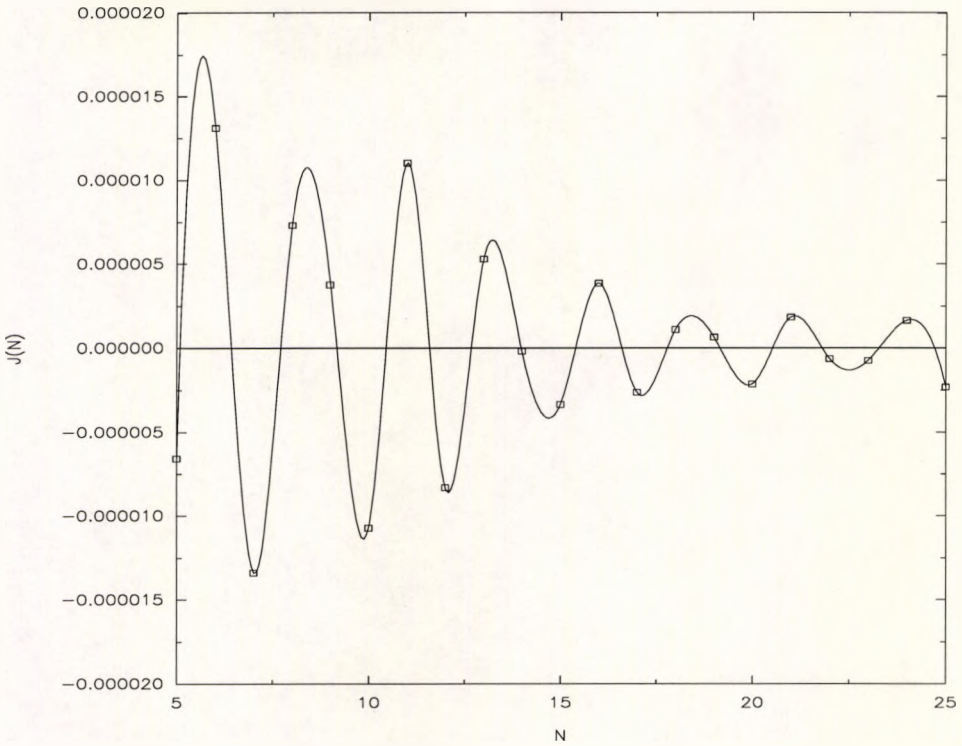

Figure 3.56: Exchange coupling for (001) trilayer associated with the point $k_x = k_y = 0$.

Numerical approach

Now we compute the exchange coupling using the numerical approach of Section 3.2. The last step in computing J(N) is obtained by using the same Equation as for the analtytic approach ie Equation 3.31. The thermodynamic potentials $\Omega^{\uparrow\downarrow}(N)_{FM}$ and $\Omega^{\uparrow\downarrow}(N)_{AF}$ in this formula are computed using Equation 3.30. The summation over $k_{||}$ in the formula for the thermodynamic potential is computed using the prescription as set out by Cunningham and is outlined in Section 3.2.2. In accordance with this summation procedure we increase the number of $k_{||}$ points used in the summation until the results converge to a required accuracy.

We start by comparing the exchange coupling using 528 and 2080 $k_{||}$ points in the $k_{||}$ summation in Figure 3.57. It is obvious from this graph that the results have not converged and conclude that more than 528 $k_{||}$ points are needed in the $k_{||}$ summation. Therefore we next compare the exchange coupling obtained using 2080 and 8256 $k_{||}$ points in the $k_{||}$ summation in Figure 3.58. As before we can see the results have not yet converged and conclude that more than 2080 $k_{||}$ points are needed in the $k_{||}$ summation. In Figure 3.59 we compare the exchange coupling obtained using 8256 and 32896 $k_{||}$ points in the $k_{||}$ summation. Again we see from this graph that the results have not yet converged but it is showing signs of convergence and it it likely not many more steps will be required. Finally in Figure 3.60 we compare the exchange coupling obtained using 32896 and 131328 $k_{||}$ points in the summation. It is clear from this graph that the results have converged to the required accuracy and conclude that for this example it is sufficient to use 32896 $k_{||}$ points

in the $k_{||}$ summation for the reduced BZ. One thing to note about all the graphs showing the exchange coupling is the vertical axis should read $J(N) \times a^2$, where a is the inter-atomic distance and a cubic spline has been fitted to the data.

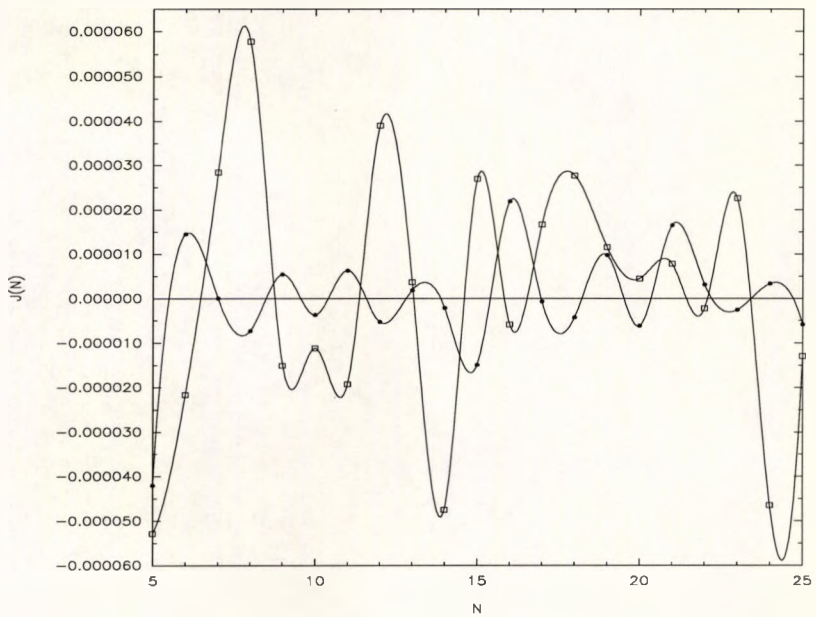

Figure 3.57: Comparison of the exchange coupling obtained using 528 (squares) and 2080 (circles) $k_{||}$ points in the $k_{||}$ summation for the reduced BZ.

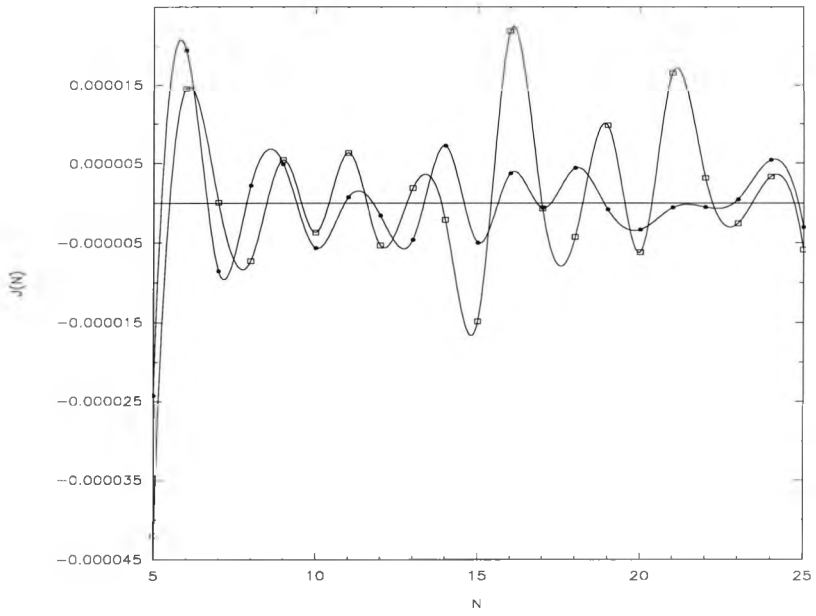

Figure 3.58: Comparison of the exchange coupling obtained using 2080 (squares) and 8256 (circles) $k_{||}$ points in the $k_{||}$ summation for the reduced BZ.

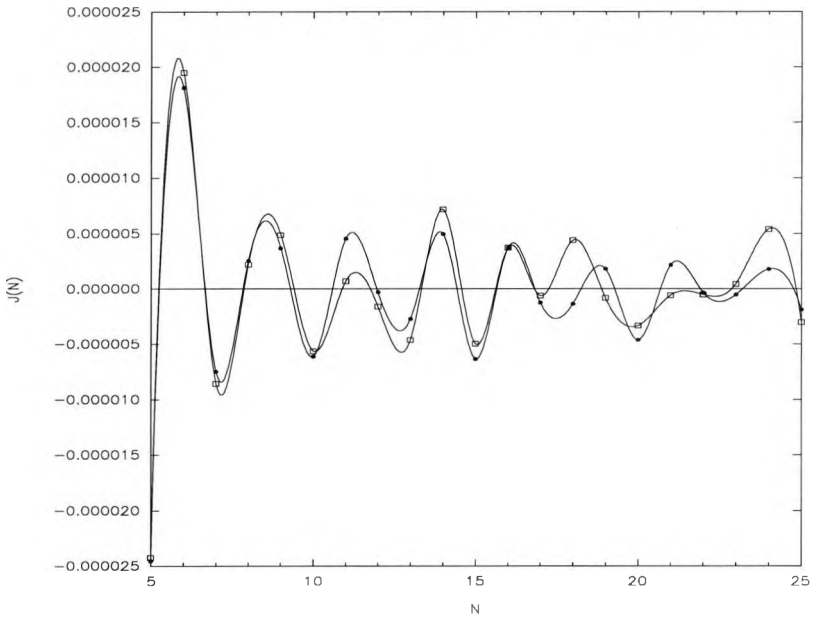

Figure 3.59: Comparison of the exchange coupling obtained using 8256 (squares) and 32896 (circles) $k_{||}$ points in the $k_{||}$ summation for the reduced BZ.

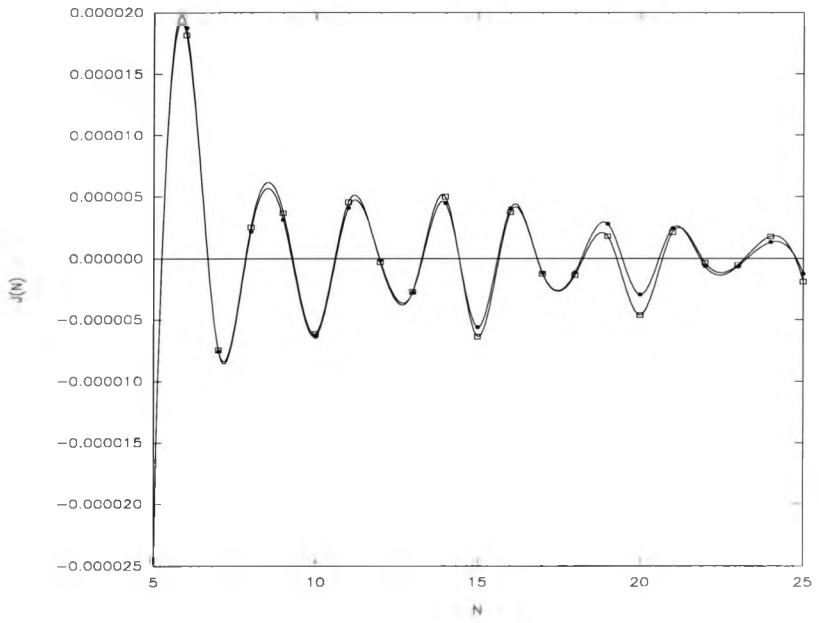

Figure 3.60: Comparison of the exchange coupling obtained using 32896 (squares) and 131328 (circles) $k_{||}$ points in the $k_{||}$ summation for the reduced BZ.

Comparison of the results

Now we have computed the exchange coupling using the analytic and numerical approaches we can compare the results to ensure they are in agreement with each other. This is shown in Figure 3.61. As we saw from the results of the single orbital trilayer in Section 2.5 we expect a phase shift between the SPA and the numerical results, which is a result of limiting this asymptotic formula to the leading term only, see Ref [43]. The graph shows there is indeed an apparent phase shift between the two sets of data. On close inspection the two sets of data are actually in good agreement with each other. However for between 7 and 12 atomic planes there does seem to be a relatively large difference between the data. Firstly the cubic spline has emphasized the difference at 8 atomic planes. Secondly as we saw with the single

orbital trilayer the apparent phase shift coupled with a short period resulted in an apparently large difference in the results. For this example both periods are short. We conclude that the combination of two short periods in the exchange coupling and the apparent phase shift has resulted in the relatively large difference between the two sets of data between 7 and 12 atomic planes. Otherwise the two sets of data are in close agreement. Even between 7 and 12 atomic planes all the main features of the exchange coupling are in close agreement except for the amplitude of the oscillations and this differs within an acceptable limit.

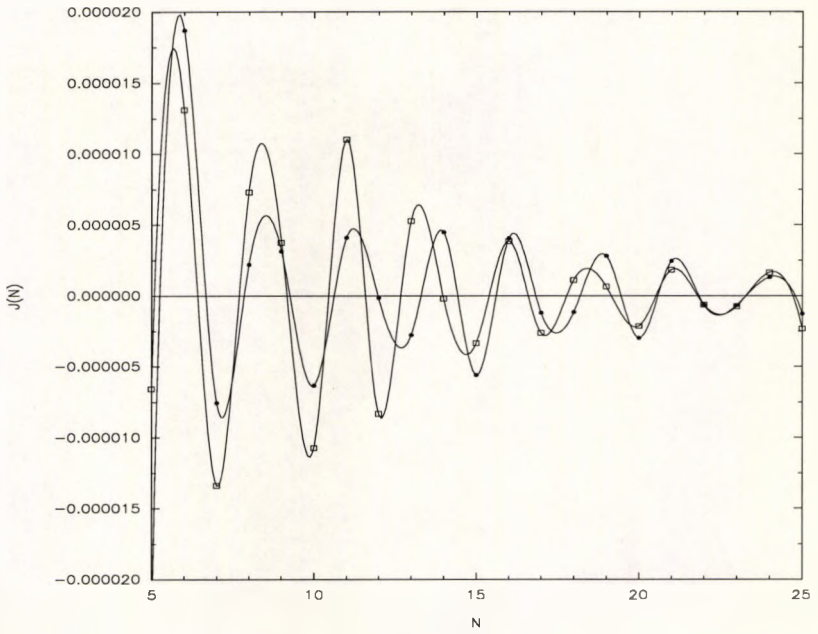

Figure 3.61: Comparison of the exchange coupling obtained using 131328 (circles) $k_{||}$ points in the $k_{||}$ summation for the reduced BZ and the results obtained using the stationary phase approximation (squares).

Conclusions

The generalization of the one band model of exchange coupling using the quantum well theory has for the first time enabled us to model what effect hybridization has on the exchange coupling. It is clear from the results that it can have a significant effect and therefore must be taken into account to achieve realistic results. This is true even if only one band of electrons is intersected by the spacer Fermi surface and it hybridizes with a second band of electrons.

- The analytic expression for the average spectral density for the single orbital trilayer proves explicitly for the first time that one can treat N as a continuous variable and the spectral density is therefore also a periodic function in N.

- When obtaining the surface Green's function for the two band semi-infinite crystal we demonstrated the exchange coupling is dependent on the thickness of the ferromagnetic layers.

- Hybridization in the ferromagnetic layers has no effect on the period of oscillations. The period of oscillations is directly related to the Fermi surface of the spacer layer, which is exploited by us in the SPA and by the RKKY model of exchange coupling. As the hybridization in the ferromagnetic layers has no effect on the Fermi surface of the spacer layer we expected this result prior to the analysis and the subsequent result agreed with this.

- Increasing hybridization in the ferromagnetic layers increases the amplitude of oscillations. The exchange coupling orginates from the exchange splitting

of the d-band in the ferromagnetic metals. When the d-band hybridizes with an s-band, the s-band electrons effectively "see" the exchange splitting, which is transmitted into the spacer layer. As the hybridization is increased the s-band "sees" a stronger exchange splitting which results in stronger exchange coupling.

- Increasing the hybridization in the spacer layer decreases the period of oscillations. We conclude that the hybridization in the spacer layer has an effect on the period as it alters the Fermi surface.

- Increasing the hybridization in the spacer layer increases the amplitude of the exchange coupling. This effect is similar to the hybridization in the ferromagnetic layers and results in the s-band electrons "seeing" a stronger exchange splitting and therefore also stronger exchange coupling.

The main objective of this thesis has been to generalize the one band model of exchange coupling to two bands and also incorporate hybridization into the model. It should be viewed as an important step in extending the possible aplications of the quantum well theory. One interesting feature we demonstrated , a while ago now, was that the exchange coupling is dependent on the thickness of the ferromagnetic layers. By taking semi-infinite ferromagnetic layers we neglect this parameter in our model. One future development of the model is to include the ferromagnetic layer thickness into the calculations and some work has been done in this field, see Ref [29]. Another development is to generalize the models so that more than

two bands can be considered as in the nine bands in Cu for example. We can now consider the case when the exchange coupling oscillates with 1 or 2 periods, using the analytic approach. Another development of the model is the generalization of the SPA so that we can model transition metals with more than two bands intersecting the Fermi surface in the spacer layer.

Bibliography

[1] Herman M.H. and Sitter H. : Molecular Beam Epitaxy-Fundamentals and Current Status (Berlin : Springer-Verlag) (1989)

[2] Parkin S.S, Bhadra R. and Roche K.P. : Physical Review Letters **66** 2152-2155 (1991)

[3] Parkin S.S., More N. and Roche K.P. : Physical Review Letters **64** 2304-2307 (1990)

[4] Qiu Z.Q., Pearson J. and Bader S.D. : Physical Review B **46** 8659-8662 (1992)

[5] Purcell S.T., Johnson M.T., McGee N.W, Coehoorn R. and Hoving W. : Physical Review B **45** 13064-13067 (1992)

[6] Purcell S.T., Folkerts W., Johnson M.T., McGee N.W, Jager K., aan de Stegge J., Zeper W.B. and Hoving W. : Physical Review Letters **67** 903-906 (1991)

[7] Coehoorn R., Johnson M.T, Folkerts W., Purcell S.T., McGee N.W., De Veirman A. and Bloemen P.J : Magnetism and Structure in Systems of Reduced Dimension (Plenum, New York) (1993)

[8] Wohlfarth E.P. : Physics Letters **36A** 131-132 (1971) : Ferromagnetic Materials Vol 1 (Amsterdam: North-Holland) 3-70 (1980)

[9] Hubbard J. : Proceeding of the Royal Society of London **A276** 238-257 (1963)

[10] Hubbard J. : Proceeding of the Royal Society of London **A281** 401-419 (1964)

[11] Thompson E.D. : Annals of Physics **22** 309-349 (1963)

[12] Thompson E.D., Wohlfarth E.P. and Bryan A.C. : Proceedings of the Physical Society **83** 59-70 (1964)

[13] Hohenberg P. and Kohn W. : Physical Review **136** B 864-871 (1964)

[14] Kohn W. and Sham L.J. : Physical Review **140** A 1133-1138 (1965)

[15] Lang P., Nordström L., Zeller R. and Dederichs P.H. : Physical Review Letters **71** 1927-1930 (1993)

[16] Zeller R., Lang P., Drittler B. and Dederichs P.H. : Mat. Res. Soc. Symp. Proc. **253** 357-368 (1992)

[17] Herman F. and Van Schilfgaarde M. : Physical Review Letters **71** 1923-1926 (1993)

[18] Anderson O.K., Jepsen O. and Glötzel D. : Highlights of Condensed Matter Theory (North Holland, Amsterdam) (1985)

[19] Wimmer E., Krakauer H., Weinert M. and Freeman A.J. : Physical Review B **24** 864-875 (1981)

[20] Anderson O.K. : Physical Review B **12** 3060-3083 (1975)

[21] Posternak M., Krakauer H., Freeman A.J. and Koelling D.D. : Physical Review B **21** 5601-5611 (1980)

[22] Foulkes W.M.C. and Haydock R. : Physical Review B **39** 12520-12536 (1989)

[23] Ruderman M.A. and Kittel C. : Physical Review **96** 99-102 (1954)

[24] Bruno P. and Chappert C. : Physical Review Letters **67** 1602-1605 (1991)

[25] Bruno P. and Chappert C. : Physical Review B **46** 261-270 (1992)

[26] Baltensperger W. and Helman J.S. : Applied Physics Letters **57** 2954-2955 (1990)

[27] Yafet Y. : Physical Review B **36** 3948-3949 (1987)

[28] Bloemen P.J.H., Johnson M.T., M.T.H. van de Vorst, Coehoorn R., J.J. de Vries, Jungblut R., J. aan de Stegge, Reinders A. and W.J.M. de Jonge : Physical Review Letters **72** 764-767 (1994)

[29] d'Albuquerque e Castro J., Mathon J., Villeret M. and Edwards D.M. : Physical Review B **51** 12876-12879 (1995)

[30] Roth L.M., Zeiger H.J. and Kaplan T.A. : Physical Review **149** 519-525 (1966)

[31] Coehoorn R. : Physical Review B **44** 9331-9337 (1991)

[32] Deaven D.M., Rokhsar D.S. and Johnson M. : Physical Review B **44** 5977-5980 (1991)

[33] Edwards D.M., Mathon J., Muniz R.B. and Phan M.S. : Journal of Physics Condensed Matter **3** 4941-4958 (1991)

[34] Edwards D.M., Mathon J., Muniz R.B. and Phan M.S. : Physical Review Letters **67** 493-496 (1991)

[35] Zubarev D.N. : Translation; Soviet Physics USP **3** 320-330 (1960)

[36] Mathon J. and Ahmad M.S. : Physical Review B **37** 660-663 (1988)

[37] Phan M.S. : Ph.D Thesis , City University (1989)

[38] Kalkstein D. and Soven P. : Surface Science **26** 85-99 (1971)

[39] Mathon J. : Journal of Physics Condensed Matter **1** 2505-2514 (1989)

[40] Zeller R., Deutz J. and Dederichs P.H. : Solid State Communications **44** 993-997 (1982)

[41] Cunningham S.L. : Physical Review B **10** 4988-4994 (1974)

[42] Abrikosov A.A. : Introduction to the Theory of Normal Metals (Academic, New York) (1972)

[43] Mathon J., Villeret M. and Edwards D.M. : Journal of Physics Condensed Matter **4** 9873-9892 (1992)

[44] Cassels J.M. : Basic Quantum Mechanics 2 nd Edition

[45] Quantum Mechanics lecture notes : City University (1991)

[46] Mathon J., Villeret M., Mander J., Edwards D.M. and Muniz R. : Mat. Res. Soc. Symp. Proc. **313** 171 (1993)

[47] Mathon J. : Contemporary Physics **32** 143-156 (1991)

[48] Mathon J. : Reports on Progress in Physics **51** 1-56 (1988)

[49] Ahmad S.B. : Ph.D Thesis , City University (1990)

[50] Mathon J. : Physica B **149** 31-36 (1988b)

[51] Bajpai A.C., Mustoe L.R. and Walker D. : Advanced Engineering Mathematics 2nd Edition Wiley